EXPERIMENTAL STUDY OF A MICROFLUIDIC FLOW USING A MICRO-PIV SYSTEM

A Thesis

Submitted to the College of Graduate and Postdoctoral Studies

In Partial Fulfilment of the Requirements for the Degree of

Master of Science

In the Department of Mechanical Engineering

University of Saskatchewan

Saskatoon, Saskatchewan, Canada

By

Amin Jahan Panah

PERMISSION TO USE

In presenting this thesis in partial fulfillment of the requirements for a Postgraduate degree from the University of Saskatchewan, I agree that the Libraries of this University may make it freely available for inspection. I further agree that permission for copying of this thesis in any manner, in whole or in part, for scholarly purposes may be granted by the professor or professors who supervised my thesis/dissertation work or, in their absence, by the Head of the Department or the Dean of the College in which my thesis work was done.

It is understood that any copying or publication or use of this thesis or parts thereof for financial gain shall not be allowed without my written permission. It is also understood that due recognition shall be given to me and to the University of Saskatchewan in any scholarly use which may be made of any material in my thesis.

Requests for permission to copy or to make other uses of materials in this thesis in whole or part should be addressed to:

Head of the Department of Mechanical Engineering
University of Saskatchewan
Engineering Building, 57 Campus Drive
Saskatoon, SK S7N 5A9
Canada
OR

Dean of the College of Graduate and Postdoctoral Studies
University of Saskatchewan
116 Thorvaldson Building, 110 Science Place
Saskatoon, SK S7N 5C9
Canada.

ABSTRACT

This thesis presents an experimental study of a creeping flow of water inside a micro-scale rectangular cross-sectional channel (110 μm × 40 μm) using Micro-Particle Image Velocimetry (Micro-PIV). Micro-PIV is designed to achieve the micro-scale resolution required for microfluidic flow investigation. One of the most important modifications is the implementation of volume illumination instead of the thin light sheet used in regular PIV systems.

Due to the widespread development of micro-scale devices, many experimental investigations of microfluidic flows using Micro-PIV are reported in the literature. However, relatively few of them have investigated the effects of volume illumination on the measured velocity profiles. In the present study, it became evident that the Depth of Correlation (DOC), which is a characteristic of volume illumination, has a significant effect on the measured velocity profiles. To illustrate this, two objective lenses with different magnifications (10x and 20x) were used for the measurements. The other parameters, i.e. the flow rate (Q = 100 μL/hr), channel geometry, size of the seeding particles (d_p = 3 μm) were kept constant during the experiment. An analytical solution for the 3D velocity profile was obtained from the governing equations. The effect of the DOC on the measured velocity profiles appeared as a reduction in the peak velocity compared to the centre-plane value based on the analytical solution. In order to show that this deficiency was due to the volume illumination, a special volume-averaging scheme was applied to the analytical solution. By comparing the experimental and volume-averaged analytical velocity profiles, one could determine the effective value of the DOC (37 μm and 27.5 μm for the 10x and the 20x magnification, respectively). These experimental values were consistent with previously reported DOC values for the 10x and the 20x objectives and for the 3 μm seeding particles.

The other objective was to assess the ability of the Micro-PIV to achieve near-wall velocity measurements. A significant improvement was observed in the near-wall resolution by using a higher magnification. This improvement was quantified by calculating the deviation of the measured velocity profiles from the volume-averaged analytical velocity profiles. The deviation exceeded 30% of the peak velocity in the near-wall region for the 10x magnification while it did not go beyond the 10% for the 20x magnification. The smaller interrogation regions in the 20x measurements was introduced as the most likely explanation for this enhancement.

ACKNOWLEDGEMENTS

I would like to take this opportunity to express my sincere thanks to people who had directly and indirectly helped me to finish my M.Sc. program successfully at the University of Saskatchewan.

I sincerely appreciate my supervisor professors, Prof. D J Bergstrom and Prof. J D Bugg for their thoughtful insights, guidance advice and their precious time which never withhold it to discuss my problems with them about the project. My special thanks goes to Prof. Bergstrom whose advices helped me beyond this project and never let me to lose my motivations during my program. I also appreciate him for providing financial support for my program.

I would like to acknowledge our lab technician, Shawn Reinink. The project progress was not possible without his deep technical knowledge. I also would like to thank CFD lab group members who help me by expressing their point of views about my project and provided fun atmosphere in the lab.

I also would like to thank the Department of Mechanical Engineering, College of Graduate and Postdoctoral Studies and the Natural Sciences and Engineering Research Council of Canada (NSERC) for providing financial support in the form of scholarships and teaching assistantships.

Finally, I would like to thank my parents who beside emotional support provided the major financial support for my program. I also would like to appreciate my real friends Majid Khak Pour, Mehraneh Ghavami & Kourosh Masoudnia who always stood beside me in hard times.

DEDICATION

To

My wonderful parents ***Dr. Jafar Jahan Panah*** and ***Mrs. Mahnaz Alishahi***

And my lovely sister ***Nilufar Jahan Panah***

TABLE OF CONTENTS

LIST OF FIGURES

LIST OF TABLES

LIST OF SYMBOLS

Acronyms

CCD	Charge Coupled Device
CMO	Common Main Objective
CMOS	Complementary Metal Oxide Semiconductor
DOC	Depth of Correlation
DOF	Depth of Field
DSMC	Direct Simulation Monte Carlo
FTV	Flow-Tagging Velocimetry
FOV	Field of View
ITV	Infrared Thermal Velocimetry
LDA	Laser Doppler Anemometry
LDV	Laser Doppler Velocimetry
LIF	Laser-Induced Fluorescence
LIMT	Laser-Induced Molecular Tagging
LIPA	Laser-Induced Photochemical Anemometry
LOC	Lab-on-Chip
Micro-PIV	Micro Particle Image Velocimetry
MTV	Molecular Tagging Velocimetry
NA	Numerical Aperture
PCR	Polymerase Chain Reaction
PF	Photo bleached Fluorescence
PHANTOMM	Photo-Activated Nonintrusive Tracking of Molecular Motion
PIV	Particle Image Velocimetry
PSV	Particle Streak Velocimetry
PTV	Particle Tracking Velocimetry
RAM	Random Access Memory
RMS	Root Mean Square
SIV	Scalar Image Velocimetry
SPE	Single Pixel Ensemble
TIR	Total Internal Reflection
2D2C	2 Dimensions and 2 Components
3D3C	3 Dimensions and 3 Components
2D	2 Dimensional
3D	3 Dimensional

Nomenclature

a	Arbitrary distance from the bottom-wall of the device
C	Concentration of particle solution
c	Convolution product

D	Diffusion coefficient
D_a	Diameter of the lens aperture
d_a	Diameter of the aberrated image of a point source
d_p	Diameter of the particles
d_s	Diffraction-limited spot diameter
d_t	Particle image diameter
e	Smallest distance that can be resolved by a detector
f	Focal length of the lens
$f^{\#}$	f number of the lens
I	Intensity of the focused particles
I_B	Average intensity of the background noise
k	Boltzmann's constant
L	Depth of the microfluidic device
M	Magnification of the objective lens
M_0	Magnification of the objective
n	Refractive index of the medium which lens is immersed
NA	Numerical Aperture of the lens
P	Size of the interrogation window in the *x* direction
Q	Size of the interrogation window in the *y* direction
S	Mean square distance passed by a particle
T	Time
T	Absolute temperature
u	Magnitude of velocity
u_x	Magnitude of velocity in the x-direction
u_y	Magnitude of velocity in the y-direction
u_z	Magnitude of velocity in the z-direction
v	Velocity in the y-direction
V	Particle visibility
V_{fr}	Volume fraction of particle solution
x	Direction along the x axis
y	Direction along the y axis
z	Direction along the z axis
z_0	Working distance of the objective

Greek Symbols

β	Cut-off level parameter
Δx	Shift in x direction
Δt	Time difference
δ	Dirac function
δ_z	Thickness of the measurement plane
δ_{z_f}	Depth of Field
$\delta_{z_{corr}}$	Value of depth of correlation
$\delta_{z_{corr_0}}$	Value of depth of correlation without the effect of Brownian motion
ε	Cut-off for the on-axis image intensity

ε_B	Error due to Brownian motion
Θ_{cc}	2D correlation function
λ	Wavelength of the light
λ_0	Wavelength of light in vacuum
μ	Dynamic viscosity

Dimensionless Groups

Re	Reynolds Number

CHAPTER 1: INTRODUCTION

Studying flow fields at the micron scale has become important in many areas of science and engineering in recent years. Micro-fabricated fluidic devices are becoming ubiquitous in aerospace, automotive, computer, pharmaceutical and biomedical applications. The study of fluid flows in these devices is called microfluidics (Markus *et al.,* 2018). The intense development of microfluidic devices lies in the advantages that result from miniaturization. Some of these advantages include faster analysis due to the smaller fluid volume needed for chemical reactions. This can also decrease the cost of these processes as the consumption of reagents, which are expensive chemicals used in these reactions, decreases. Another advantage is the lower energy used during fabrication and operation, which make these devices energy efficient compared to traditional methods (Tabeling, 2005).

The study of microfluidics consists of two approaches: continuum and sub-continuum microfluidics. In continuum microfluidics, which is the main focus of the thesis research, the fluid behaves as a continuum. Therefore, the same governing equations as for conventional flows at much larger length scales, i.e. the Navier-Stokes equations, are applicable. Non-intuitive behavior can still occur in continuum microfluidics, since the size of the system is reduced and the scale of the fluid forces changes. For example, the inertia force is proportional to the third power of the length scale and shear stress scales with the second power of the length scale. Therefore, most continuum microfluidic systems operate in a viscous-dominated regime where the Reynolds number is much lower than one. Also, surface tension is proportional to the inverse of the length scale making it more important in microfluidic systems than in larger sealed flows (Song *et al*., 2018).

For sub-continuum microfluidics, the Navier-Stokes equations are not applicable. An example of sub-continuum microfluidics is the flow of rarified gas around a hard drive read/write head. The Knudsen number, which is the ratio of the molecular mean free path to the length scale of the system, is larger than 0.1 in this case. Therefore, lattice Boltzmann or Direct Simulation Monte Carlo (DSMC) methods are usually implemented to describe the flow through these system (Nguyen *et al.*, 2006).

Some examples of continuum microfluidics in aerospace engineering are micron-scale supersonic nozzles that are used as micro-thrusters in micro- and nano-satellites, or used for the purpose of flow control devices in micro-air vehicles. Inkjet printers are good examples in the computer industry. These printers contain an array of nozzles with exit-orifice diameters on the order of tens of micrometers. Tiny nozzles are also used for fuel spray generation in automobile engines. The process engineering and pharmaceutical industries use continuum microfluidics for the homogenization of a media using membranes or tiny orifices (Gothsch *et al*., 2015); (Kelemen *et al*., 2015).

The most important application of continuum microfluidic technology is the micro-fabricated lab-on-chip (LOC) devices in the biomedical industry. These devices can be used for patient diagnosis and monitoring (Laurell *et al*., 2007), drug delivery and trapping (Bruus *et al*., 2011), and separation and sorting of cells (Muller *et al.*, 2013). Examples of these devices include microscale flow cytometers for cancer cell detection, micro-machined electrophoretic channels for DNA fractionation and polymerase chain reaction (PCR) chambers for DNA amplification (Li, 2008).

Such factors as nonlinear interactions between macromolecules, cells and the fluid medium in the microfluidic devices and the surface-dominated physics of the channel create complicated phenomena that make numerical simulation of the processes occurring in these devices challenging. Therefore, experimental methods are an ideal technique to study these flows (Markus *et al.*, 2018). There are many different experimental methods than can be implemented to measure the flow field either qualitatively or quantitatively in microfluidic systems.

Flow field measurement techniques used for microfluidic flows are usually the same methods developed for traditional macro-scale flows modified for the challenges of the small length scales associated with microfluidic systems. Non-optical methods such as a pitot tube and hot wire anemometry are not suitable for measuring flow in microfluidic devices. This is mainly due to the fact that these methods are intrusive and the smallest intrusion into a microfluidic system can affect the nature of the flow and change the geometry of the system. Therefore, optical methods are more suitable for studying the flow in these applications. Among optical methods Laser Doppler Anemometry (LDA) is not a suitable tool to study microfluidic flows due to the challenges of creating micro-scale measurement volumes. Also, it is a single point measurement method,

which does not provide enough information to calculate velocity gradients. PIV is known as the most reliable experimental method developed so far, with the lowest number of drawbacks compared to other methods. Besides being non-intrusive, it provides full field information, which is much more useful for studying velocity. Other parameters, such as the strain rate distribution, can be obtained using whole field data. These features make PIV an excellent tool for studying microfluidic flows.

1.1. Objectives

The main motivation behind this project is to perform a first set of measurements with a newly acquired Micro-PIV device from La Vision and assess the validity of these measurements. In order to do this, a flow was selected that has an analytical solution to allow validation of the measurements. For this purpose, a low Reynolds number flow of water inside a rectangular cross-section microchannel was selected. Therefore, flow through a rectangular cross-section microchannel is studied with two different magnifications (10x and 20x) and compared to the analytical solution.

During measurements it was discovered that the thickness of the measurement plane, known as the Depth of Correlation (DOC), is a critical parameter to consider when designing a Micro-PIV experiment. The two main objectives of the research project are:

1. To commission a Micro-PIV device based on velocity measurements in a low Reynolds number flow of water in a rectangular cross-section microchannel.
2. To assess the effect of the DOC on the Micro-PIV measurements of the velocity field.

1.2. Background

This section provides some background on the experimental method used to study the velocity field in this research project.

1.2.1. Particle Image Velocimetry

Particle Image Velocimetry (PIV) is a method used in experimental fluid mechanics to measure instantaneous velocity fields by measuring the displacement of numerous particles that follow the motion of the fluid. The movement of the particles is captured by recording images of the flow that is seeded with particles at two instants in time and then finding either the displacement of

individual particles, Particle Tracking Velocimetry (PTV), or the average displacement of small groups of particles (PIV) (Adrian *et al.*, 2011). PTV is not a common technique since it is difficult to distinguish specific particles in two consecutive images and the velocity can be measured only at places where particles are present. Standard planar PIV systems consist of a source of illumination, light-sheet optics, a camera and image digitization hardware, a synchronizer unit, seeding particles, and a computer for data storage and analysis (see Figure 1.1). These components are briefly discussed below.

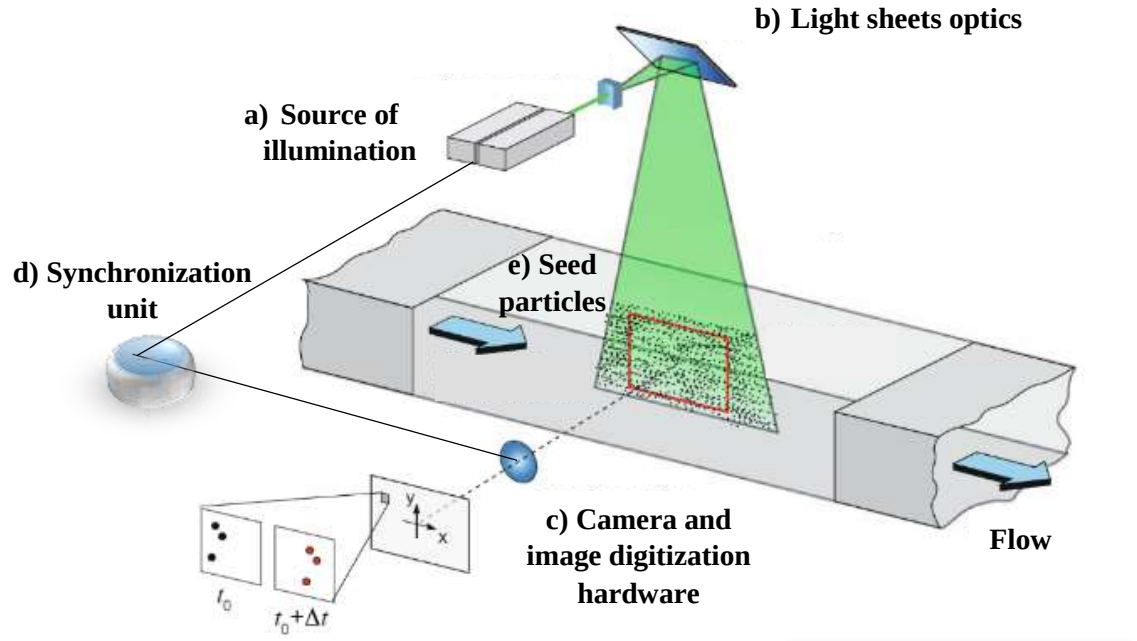

Figure 1. 1 Elements of 2D PIV (Markus *et al.*, 2018).

a) Source of illumination: Double-pulsed illumination is the current norm for PIV systems due to the issue of limited pulse frequency of the available lasers. To illuminate micro-scale particles, a laser with pulse energies between 5 and 500 mJ is required. For Micro-PIV less than 10 mJ per pulse is sufficient (Lindken *et al*., 2009). Pairs of separate lasers in a single housing are specially made for PIV applications, such as the Nd:YAG laser which uses frequency-doubling crystals to produce 532 nm pulses.

b) Light-sheet optics: Once 532 nm pulses are generated, they go through a cylindrical lens to form a thin sheet of laser light. The thickness of the light sheet is usually adjusted using a spherical lens.

c) Camera and image digitization hardware: The magnification of the objective lens is selected by either the desired resolution between adjacent velocity vectors or by the desired Field of View (FOV). The size of the particle images on the image plane cannot be calculated only from the magnification times the particle diameter. The effect of diffraction and geometric lens aberrations combine to create a particle image given by equation 1.1, (Adrian *et al.*, 2011)

$$d_\mathrm{t} = (M^2 {d_\mathrm{p}}^2 + {d_\mathrm{s}}^2 + {d_\mathrm{a}}^2)^{\frac{1}{2}} \tag{1.1}$$

where M is the magnification of the objective lens, d_t is the diameter of the particle image, d_a is the diameter of the aberrated image of a point source and, d_p is the diameter of the particles. The diffraction-limited spot diameter (d_s) is given by equation 1.2,

$$d_\mathrm{s} = 2.44(1 + M) f^{\#} \lambda \tag{1.2}$$

and

$$f^{\#} = f/D_\mathrm{a} \tag{1.3}$$

where f is the focal length of the lens, D_a is the diameter of the lens aperture and λ is the wavelength of the light. Due to diffraction, even points create finite-diameter images, and lens aberration makes images appear even broader. The diameter of the image of out-of-focus particles will be even larger than the value obtained by equation 1.1. Usually, d_t is dominated by d_s (for Micro-PIV systems, since M is large and the particle diameter is small, d_s is always dominant) (Olsen and Adrian, 2000). For locations outside the object plane, the diameter of the particle images is dominated by diffraction. The Depth of Field (DOF) is approximately given by equation 1.4 (Adrian *et al.*, 2011).

$$\delta_\mathrm{z} = 4(1 + \tfrac{1}{M})^2 {f^{\#}}^2 \lambda \tag{1.4}$$

All particles lying within $\pm(\delta_\mathrm{z})/2$ of the nominal object plane produce well-focused images. By proper selection of $f^{\#}$and M it is possible to make the DOF larger than the thickness of the light sheet. Therefore, all particles within the light sheet produce focused images.

The image on the image plane is recorded by briefly exposing a light-sensing array such as a Charged-Coupled Device (CCD) or Complementary Metal Oxide Semiconductors (CMOS) sensor. They consist of rectangular or square arrays of pixel sensors that convert the light energy into electrical signals. The process of converting a continuous image intensity field into a 2D array of analog pixel readings is called pixelization (Adrian *et al.*, 2011). The analog readings are subsequently digitized with typically 8 to 12 bit accuracy and stored first in the fast memory of a frame grabber and then in Random Access Memory (RAM).

The process of pixelization is very fast, but the time required to transfer millions of bytes of digitized data off the chip is quite slow, of order 10 ms. Therefore, standard video cameras cannot be used to record images in two separate frames. The best they can do is to record two images on one frame (single-frame double-pulsed recording). Special CCD cameras have been developed for PIV applications that have the capability to transfer the charge created by the first exposure from each pixel to an adjacent charge storage well very quickly, enabling the pixel sensor to record the second exposure almost immediately. With both images pixelized, the charges are moved off the chip at a rate about 30 MHz (2-frame, single pulse recording). The final issue in image digitization is that if the particle image is smaller than the pixel size, it is not possible to say exactly where in the image the particle image is located. This leads to a phenomenon called pixel locking. A design rule states that there should be at least 3-5 pixels per particle image diameter in order to reduce the effect of pixel locking (Wereley et al. 2010).

d) Synchronization unit: All of the events mentioned in the previous steps are coordinated by a master synchronizer. The synchronizer is responsible for arming and firing the light source at appropriate times, opening the camera shutter, activating image acquisition (in an electronic camera) and transferring data to the computer via a frame grabber.

e) Seed particles: The most important feature of seed particles in PIV is the ability to follow the flow accurately. Therefore, they should be small enough to follow the fluid and large enough to scatter sufficient light to form bright images. Particles offer important advantages over other markers such as dye or molecules. Particles produce stronger optical images and they do not diffuse or deform. The disadvantage of particles is the slip velocity, which can be kept acceptably small for almost all liquid flows (Jahanmiri, 2011).

f) Computer for data storage and analysis: Once the images are digitized and converted to an array of pixels with known intensities, they can be imported into a computer to be processed. Their quality is enhanced using various methods of image processing. The goal is to make the particle images less noisy. This step is called image pre-processing. Once an acceptable image quality is achieved, the velocity calculation operation can be performed. This is done using a cross-correlation function. The images are first divided into small segments known as interrogation regions and a correlation technique is applied to each pair of interrogation regions to calculate a velocity vector for that interrogation region. This correlation technique will be covered in more detail in Chapter 3.

Special PIV systems were developed for studying fluid flows in micro-scale passages which are known as Micro-PIV systems. A brief background on this technique is covered in the next section.

1.2.2. Micro-Particle Image Velocimetry

Micro-Particle Image Velocimetry (Micro-PIV) is a quantitative method that can be used to characterize the velocity fields of microfluidic systems (resolved length scales of 10^{-4} to 10^{-7} m). This technique is a modification of a conventional PIV system with some components changed to account for the challenges of small length scales (Markus *et al.*, 2018). The measurement method is similar to the conventional PIV system, i.e. the velocity field is calculated by capturing the movement of seed particles. Since the flow passages are very small (in the range of micrometers) in microfluidic systems, seed particles are even smaller (sometimes in the range of nm). This creates limitations in Micro-PIV measurements that require special consideration.

A microscope with a high magnification objective lens is required to provide the small FOV required. The second difference is that the seed particles are coated with fluorescent materials. In an optical elastic scattering scheme, which is the method used in normal vision, objects should be bigger than the wavelength of the illuminating light. Visible light has a wavelength of 400 nm to 700 nm. Therefore, particles smaller than 400 nm cannot be seen with visible light. In order to detect small particles clearly, they are coated with fluorescent materials that are sensitive to a specific wavelength independent of their size. Therefore, a Nd-YAG doubled-frequency laser which has a wavelength of 532 nm is used to excite the fluorescent materials coated on the surface of the particles. By this strategy any particle size will be detectable even if they are smaller than the wavelength of the exciting beam. Also, the fluorescent particles emit light at longer

wavelengths and this is an important feature which enables distinguishing between the reflection of the laser light from the test section and the scattered light from the particles. This helps to reduce noise in the Micro-PIV images.

Major difference between PIV and Micro-PIV, which makes Micro-PIV measurements much more complicated than normal PIV, is the fact that forming a light sheet that is thinner than the length scales of the microfluidic system is challenging. Therefore, another illumination technique known as volume illumination is implemented for Micro-PIV. In this method the entire flow passage is illuminated by the laser light and the measurement plane is defined by factors such as the DOF of the objective lens and the size of the particles. The thickness of this measurement plane compared to the dimensions of the flow passages in microfluidic systems is a critical factor that has a direct impact on the results of Micro-PIV measurements. This issue is investigated in this thesis. This illumination technique will be covered in more detail in Chapter 3. Different components of a Micro-PIV system are shown in Figure 1.2. The function of each component is briefly mentioned according to the numbering in Figure 1.2.

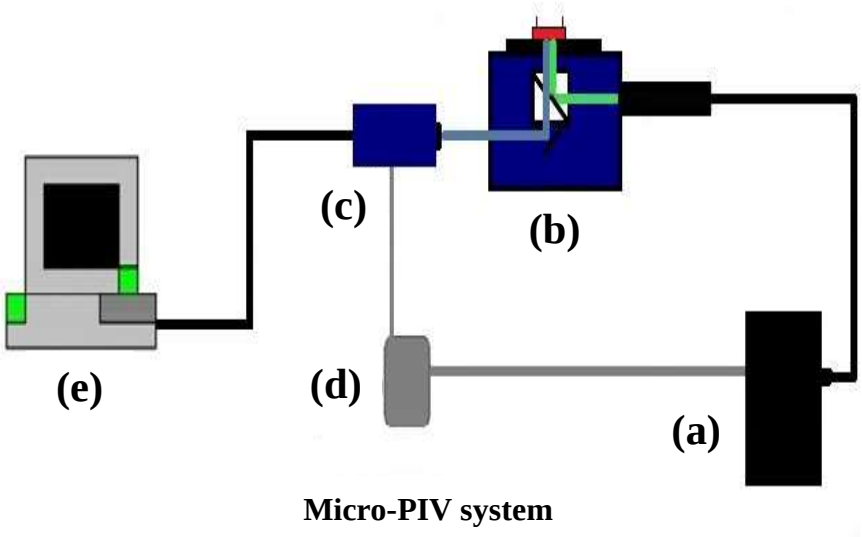

Figure 1. 2 Micro-PIV system schematic (Pitts and Fenech, 2013).

a) **Light source:** The illumination source typically ranges from Hg-arc lamps to pulsed Nd:YAG lasers. For applications where the flow contains living biological specimens that could be damaged by high intensity illumination, continuous Hg-arc lamps are a better choice. In other applications, a Nd:YAG pulsed laser is implemented (Prasad *et al*., 1992).

b) Microscope: In order to image small seed particles, microscopes with a high numerical aperture (NA) and magnification (M) are required. NA is a dimensionless number that characterizes the ability of the objective lens to collect or emit light. Common lenses range from oil-immersion (M = 100, NA = 1.4) to air immersion lenses (M = 10, NA = 0.1).

c) Camera: CCD sensors are less susceptible to noise compared to CMOS sensors. Therefore, they are a better option for Micro-PIV applications.

d) Synchronizer: The functions of all components are coordinated by a synchronizer responsible for sensing flow events that occur in real time, firing the light source at appropriate times, activating image acquisition, initiating digitization and transferring data via a frame grabber.

e) Computer: All the data go to a computer for further processing.

1.3. Thesis structure

Experimental methods of flow velocity measurement were reviewed in this chapter and Micro-PIV was introduced as the most powerful technique. A literature review of Micro-PIV is presented in Chapter 2. This literature review focuses on the first efforts to enhance micro-scale flow visualization. Modifications of Micro-PIV in order to achieve higher resolution as well as near-wall and 3D measurements are covered in Chapter 2.

Chapter 3 contains two parts. In the first part, the background theory that is required to understand the experiment design process such as volume illumination, particle visibility, correlation theory and Brownian motion are discussed. The second part is devoted to explaining components of the set-up and reasons for the chosen values of the experiment parameters. After that, data processing including interrogation region selection and processing scheme are explained.

In Chapter 4, the analytical solution of the investigated flow is presented. Next, preliminary instantaneous velocity field results are analyzed. After that, different averaging schemes such as spatial and time averaging are performed, and their results are compared with the analytical solution. Finally, the role of DOC in obtaining a match between these velocity profiles is explained. Some specific conclusions from this experimental study and recommended future work are presented in Chapter 5.

CHAPTER 2: LITERATURE REVIEW

This chapter tracks the historical development of Micro-PIV systems. In the first section of this chapter, different methods that were developed by different researchers to study microfluidic flows are covered. Flow visualization was the first tool used to study microfluidic systems. Micro-scale flow visualization methods have been categorized in different ways in the literature. A common conclusion is that Micro-PIV has many advantages over other techniques. Section 2 of this chapter describes in chronological order the Micro-PIV experiments that were designed to achieve higher resolution. Also, the evolution of 3D Micro-PIV systems is briefly discussed in this section.

2.1. Micro-Scale Flow Visualization

A variety of micro-scale flow visualization methods have evolved since the late 1990s coinciding with the widespread development of microfluidic systems. These methods can be categorized based on such factors as the tracers used to detect the fluid motion or the extent to which data are collected at a single point or over large domains.

The first effort in this field goes back to the 2000s, when Meinhart *et al*. (2000) published a review paper on different micron-resolution velocimetry techniques. They divided micron-resolution velocimetry into three techniques: Scalar Image Velocimetry, Laser Doppler Velocimetry, and Particle Image Velocimetry. Sinton (2004) divided micro-scale flow visualization methods into scalar-based, particle-based, and point-detection techniques. Other categorization methods, developed by other scientists, will be discussed later.

2.1.1. Scalar-Based Velocimetry

Scalar-based velocimetry or scalar image velocimetry (SIV) refers to the determination of a velocity vector field by recording images of a passive scalar quantity as defined by Meinhart *et al*. (2000). In this method the spatial and temporal distribution of the concentration of a transported scalar (dye) can be estimated using a pair of images. With the assumption that the scalar follows the fluid motion (non-dynamic scalars), velocity components of the fluid can be inferred from the concentration variation of the scalar in the pair of images. Reynolds dye-streak experiment in 1883 is the first known effort in SIV. The first quantitative SIV method was developed by Dahm *et al*. (1992) for measurements in turbulent jets.

Sinton (2004) discussed in detail the basic mechanisms (fluorescence, photo-bleached fluorescence, photochromic reactions, phosphorescence, caged fluorescence, and infrared heating) used in different SIV techniques for micro-flow velocimetry. Some of these techniques are laser-induced fluorescence (LIF), flow-tagging velocimetry (FTV), molecular tagging velocimetry (MTV), laser-induced molecular tagging (LIMT), laser-induced photochemical anemometry (LIPA), photo bleached fluorescence (PF), infrared thermal velocimetry (ITV) and photo-activated nonintrusive tracking of molecular motion (PHANTOMM).

Successful velocity measurements using SIV depend on factors such as having sufficient spatial variation in the passive scalar field. SIV uses molecular tracers that have much higher diffusion coefficients than particle tracers and this can significantly decrease the spatial resolution of SIV measurements. Figure 2.1 shows an example of a scalar-based image velocimetry technique (photo-bleached fluorescence imaging) that is implemented in a microchannel with an electro-osmotic flow (toward the right) in the presence of an adverse pressure gradient. These images were acquired with a 20x objective and NA = 0.5.

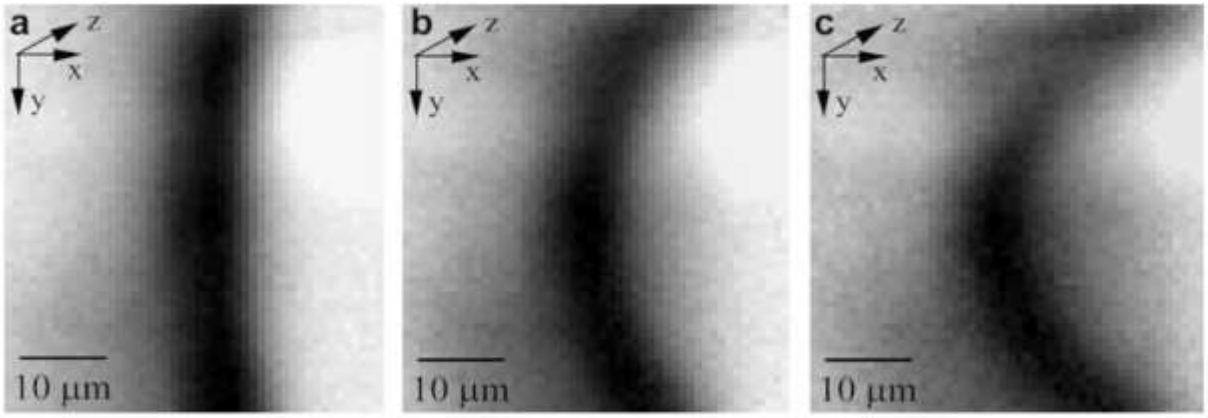

Figure 2. 1 Photo-bleached fluorescence imaging applied to combined electro-kinetically and pressure-driven flow in a square cross-section 50×50 μm^2 microchannel at **a)** t = 0 s, **b)** t = 0.06 s, and **c)** t = 0.12 s. The electric potential and pressure decreases and increases (Sinton, 2004).

2.1.2. Particle-Based Velocimetry

The most general definition of particle-based velocimetry is to measure the local fluid velocity by observing the velocity of marker particles. Laser Doppler velocimetry (LDV), particle streak velocimetry (PSV) and PIV are subcategories of particle-based velocimetry (Sinton, 2004).

LDV, also called LDA, measures the instantaneous velocity in a small spatial volume. Applying LDV to visualize micro-scale flows is challenging as it requires increased optical infrastructure to form a micro-scale fringe pattern (Sinton, 2004). Meinhart *et al*. (2000) considered LDV as a separate category of micro-flow visualization.

PSV uses particle displacement in a single image over a period of time. The signal is integrated by a CCD camera as the particle travels with the flow. However, the velocity measurements obtained by PSV are about 10 times less reliable than PIV measurements (Adrian, 1991). Figure 2.2 shows a particle streak velocimetry measurement performed on a flow through a contraction-expansion microchannel.

PIV is the most popular method to obtain a 2D or 3D velocity field. It records images of a flow that is seeded with tracer particles at two different instants of time, and determines the velocity field by analyzing the change of the particle distribution over time. PIV (Micro-PIV) provides more flow information than LDV and PSV for micro-flow measurements (Sinton, 2004).

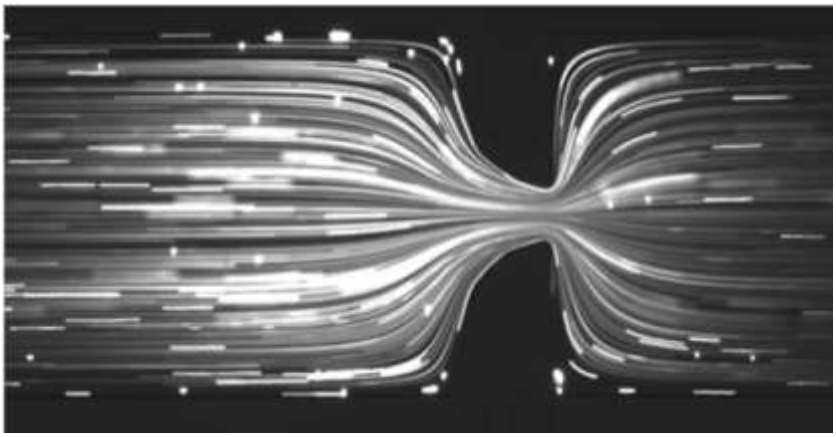

Figure 2. 2 Flow visualization using streak line photography technique of a viscoelastic fluid flowing through a contraction-expansion geometry (Galindo-Rosales, 2017).

2.1.3. Point-Detection Scanning Based Velocimetry

The final category in the review paper of Sinton (2004) is the point detection scanning technique for micro-flow visualization, which is based on single-point, high-resolution measurements using confocal fluorescent microscopy. As shown by Park *et al*. (2004), this has several advantages over typical Micro-PIV systems such as high sensitivity, high spatial accuracy, and 3D measurements. These advantages are obtained at the cost of scanning all points in a 2D plane which takes time.

This fact limits its application to low-speed microfluidics. Wereley and Meinhart (2010) considered this method as 3D Micro-PIV. Figure 2.3 shows a typical confocal laser scanning Micro-PIV system. Its working principles will be explained in more detail in the section on 3D Micro-PIV.

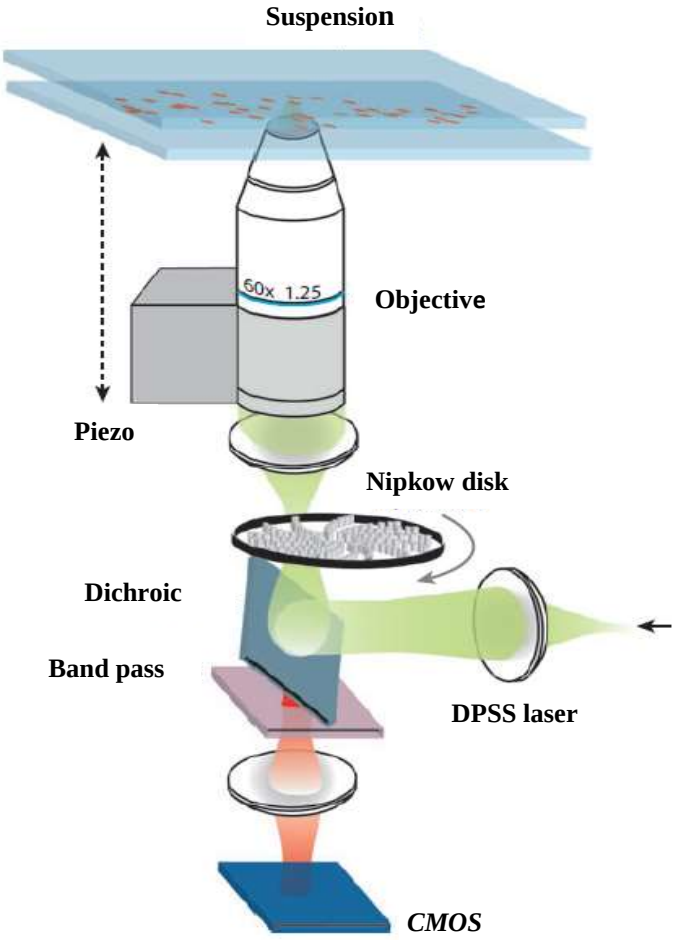

Figure 2. 3 Schematic of a confocal laser scanning Micro-PIV system (Wereley and Meinhart, 2010).

2.1.4. Final Remarks on Micro-Flow Visualization Techniques

As mentioned, there are other categorizations of micro-flow velocimetry techniques reflecting different scientists points of view. For example, Lindken *et al*. (2009) divided micro-flow visualization into qualitative and quantitative groups. Based on their categorization, phosphorescence imaging, photo-bleaching, molecular tagging of a caged fluorescein, and Raman-

scattering are qualitative visualization methods. They placed SIV and PIV in the quantitative flow visualization category.

After all of these indicated visualization methods and their different categorization, Meinhart *et al*. (2000) mentioned Micro-PIV results as the best match to the analytical solution for Stokes flow. Sinton (2004) introduced Micro-PIV as the most prominent technique for microscale flow visualization. Lindken *et al*. (2009) introduced Micro-PIV as the most established method of this kind, because it is in a well-developed state and commercial units can be purchased from various suppliers. All of these facts, indicate that Micro-PIV is a reliable method for studying fluid flow at the micro-scale. In the next section the historical development of Micro-PIV systems is covered.

2.2. Historical Development of Micro-Particle Image Velocimetry

In this section, the development of Micro-PIV systems in terms of both the achieved resolution and the data collection method, such as 2D and 3D measurement, is covered chronologically.

2.2.1. 2D Micro-Particle Image Velocimetry

In the natural development of PIV systems for obtaining higher spatial resolution, Micro-PIV was invented. Table 2.1 shows how the first Micro-PIV system was developed by Santiago *et al*. (1998). They studied Stokes flow around surface irregularities on a piece of frosted glass and achieved a spatial resolution of $6.9 \times 6.9 \times 1.5\ \mu m^3$. Their system implemented an epi-fluorescent microscope and an intensified CCD camera to image the flow of 300 nm diameter polystyrene tracing particles in water. The progression of subsequent studies towards higher spatial resolution is illustrated in Table 2.1.

Meinhart *et al*. (1999) applied Micro-PIV to measure the flow field inside a $30 \times 300\ \mu m^2$ rectangular channel with a flow rate of 50 μL/hr which corresponds to a centerline velocity of 10 mm/s. They achieved a resolution of $5 \times 1.3 \times 2.8\ \mu m^3$. Koutsiaris *et al*. (1999) developed a Micro-PIV system suitable for relatively slow flows that implemented 10 μm glass spheres as tracer particles. They achieved a coarse ($26.2 \times 26.2 \times 26.2\ \mu m^3$) spatial resolution. The flow of water inside a 236 μm diameter glass capillary tube was studied, and they found agreement between the measurements and the analytical solution.

Table 2. 1 Historical progression of Micro-PIV toward higher spatial resolutions (Markus *et al.*, 2018).

Technique	Author	Flow Tracer	Spatial Resolution (μm^3)	Observation
PIV	Urushihara *et al.*, (1993)	1 μm oil droplets	280 × 280 × 200	Turbulent flow
Super-resolution PIV	Keane *et al.* (1995)	1 μm oil droplets	50 × 50 × 200	Particle tracking velocimetry
Micro-PIV	Santiago *et al.* (1998)	300 nm polystyrene particles	6.9 × 6.9 × 1.5	Hele-Shaw flow
Micro-PIV	Meinhart *et al.* (1999)	200 nm polystyrene particles	5.0 × 1.3 × 2.8	Microchannel flow
Micro-PIV	Koutsiaris *et al.* (1999)	10 μm glass spheres	26.2 × 26.2 × 26.2	Glass capillaries
Evanescent Wave PIV	Sadr *et al.* (2012)	50 nm polystyrene particles	78 × 28 × 0.3	Fused silica microchannel flows
Micro-PIV (SPE)	Chuang *et al.* (2012)	100 nm polystyrene particles	0.13 × 0.13 × 1.2	PDMS microchannel flow

Using an evanescent field as an illumination source in Micro-PIV applications was first reported by Zettner and Yoda (2003). This technique illuminates particles that are close to the wall, therefore, it is suitable for near-wall measurements. An evanescent field is created by Total Internal Reflection (TIR) of light between a high refractive index medium and low refractive index medium. According to the Goos-Hanchen effect, instead of total reflection of light at the refractive index interface, an evanescent wave penetrates into the less dense medium and decays exponentially proportional to the normal distance from the interface which is typically on the order of a hundred nanometers thick. Therefore, only particles close to the wall are illuminated as shown in Figure 2.4 and the DOC is no longer an issue in this method. Spatial resolutions of 40 × 40 × 0.3 μm^3 and 78 × 28 × 0.3 μm^3 were reported by Zettner and Yoda (2003) and Sadr *et al*. (2012) using evanescence Micro-PIV, respectively. The key advantage of evanescence Micro-PIV is the reduced out-of-plane resolution and the ability to make near-wall measurements.

Later applications of the Micro-PIV technique progressed toward faster flows and higher spatial resolutions by using pulsed lasers such as 2-headed Nd:YAG lasers instead of Hg-arc lamps. Subsequently, Meinhart and Zhang (2000) investigated the flow inside a micro-fabricated

inkjet printer head which yielded a very high speed microfluidic measurement performed with Micro-PIV. They measured a velocity of 8 m/s which is a high value for micro-scale flows.

Single-pixel ensemble correlation methods were developed by Chuang *et al*. (2012) to increase the in-plane spatial resolution. They showed by a Monte Carlo simulation that for a camera with pixel sizes of around 6 μm, the ultimate in-plane spatial resolution is approximately 65 nm using 60 nm or smaller particles. In experiments, the best possible in-plane resolution they achieved was approximately 130 nm.

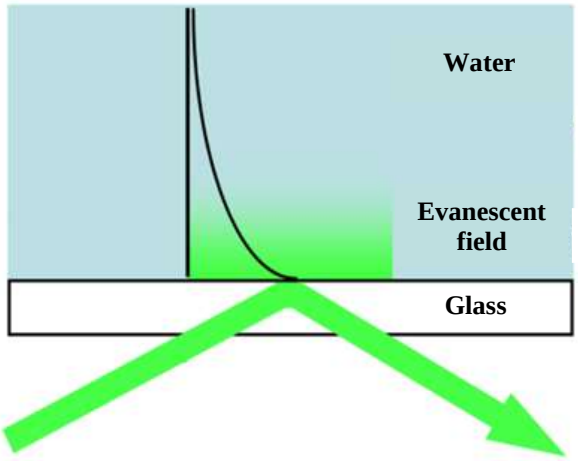

Figure 2. 4 Evanescence field generation at the interface of a high refractive index medium (glass) and low refractive index medium (water) (Torok *et al*., 1996).

Although 2D planar velocity data are sufficient in many cases for Micro-PIV experiments, defining the 3-Dimensional 3-Component (3D3C) velocity field is sometimes required since the velocity field can be complex in microfluidic devices despite the fact that the flow is laminar. In recent years, different particle-based imaging methods, such as confocal scanning microscopy (Park *et al*., 2004), stereoscopic Micro-PIV (Lindken *et al*., 2005), tomographic imaging (Elsinga *et al*., 2006), and approaches based on defocused particle images (Yoon and Kim, 2006) or optical aberrations (Kao and Verkman, 1994) have been developed to measure complex 3D velocity fields in microfluidic systems. Most of these methods require additional cameras and equipment compared to the conventional Micro-PIV. A short review of 3D Micro-PIV systems is presented in the next section.

2.2.2. 3D Micro-Particle Image Velocimetry

The flow in microfluidic systems can be complicated due to factors such as surface phenomena (electro-kinetic and electrophoresis forces), magnetic fields and complex fluid properties. This creates the need to study 3D velocity fields, motivating the development of 3D Micro-PIV systems.

3D Micro-PIV systems are divided to two groups of single camera and multi-camera approaches. Epi-Fluorescence microscopy, confocal scanning microscopy, out-of-focus imaging without aperture, and defocused imaging with aperture (3-pinhole technique) are among the single camera approaches. Stereoscopic imaging and tomographic imaging are multi-camera approaches.

2.2.2.1. Single Camera Approaches

Four different kinds of single camera 3D Micro-PIV systems are available. A review of each system is covered in this section:

a. Epi-Fluorescence Microscopy

In steady flows, it is possible to obtain 3D3C velocity data from the 2-Dimensional 2-Cmponent (2D2C) information using consecutive slices in the flow field. The third component of the velocity can be calculated by solving the continuity equation with the no-slip boundary condition at the wall for each scanned plane (Brücker, 1996). 3D3C velocity data reconstruction from multi-plane scanning in micro-flows was implemented by several scientists. Angele *et al*. (2006) designed a rotating disk upon which glass plates with different thicknesses were mounted. This changes the optical path, and therefore the position of the focal plane, fairly quickly for a scanning speed of 100 fps in the vertical direction. Shinohara *et al*. (2005) combined the dual-plane PIV concept and a scanning technique by implementing a piezo-actuator to move the objective plane while recording. Rossi *et al*. (2009) performed measurements on eight planes (each 2 μm apart) in a microchannel with living cells planted on the wall. Using these data they could obtain the mean shear stress and the average surface topology of the cells for different shear rates.

b. Confocal Scanning Microscopy

The main difference between confocal scanning microscopy and epi-fluorescence microscopy is the point-wise detection in the confocal scanning microscopy. This can greatly increase the out-

of-plane and in-plane resolution. For pointwise illumination, a laser beam is focused on the sample using micro lenses (Minsky, 1988). Micro-lenses are arranged on a spiral track on a spinning disk to increase the speed of scanning. This disk is also mechanically connected to another disk with apertures that block the light from out-of-focus points. This mechanical set-up is called a Nipkow disk. Each rotation of the Nipkow disk is equivalent to one scan of the whole FOV. 3D velocity profiles can be obtained by scanning several planes in the depth direction. However, confocal scanning microscopy is limited to low speed flows due to the limited scanning rates. The main advantages of this technique are significantly enhanced signal-to-noise ratio resulting from filtering out the effect of out-of-focus particles and the small thickness of the measurement plane (on the order of 1 to 2 μm) due to the point illumination. A schematic of the components of a confocal scanning microscope system is shown in Figure 2.5. As can be seen in Figure 2.5 (b), particles that are displaced from the focal-plane are not present in the particle images.

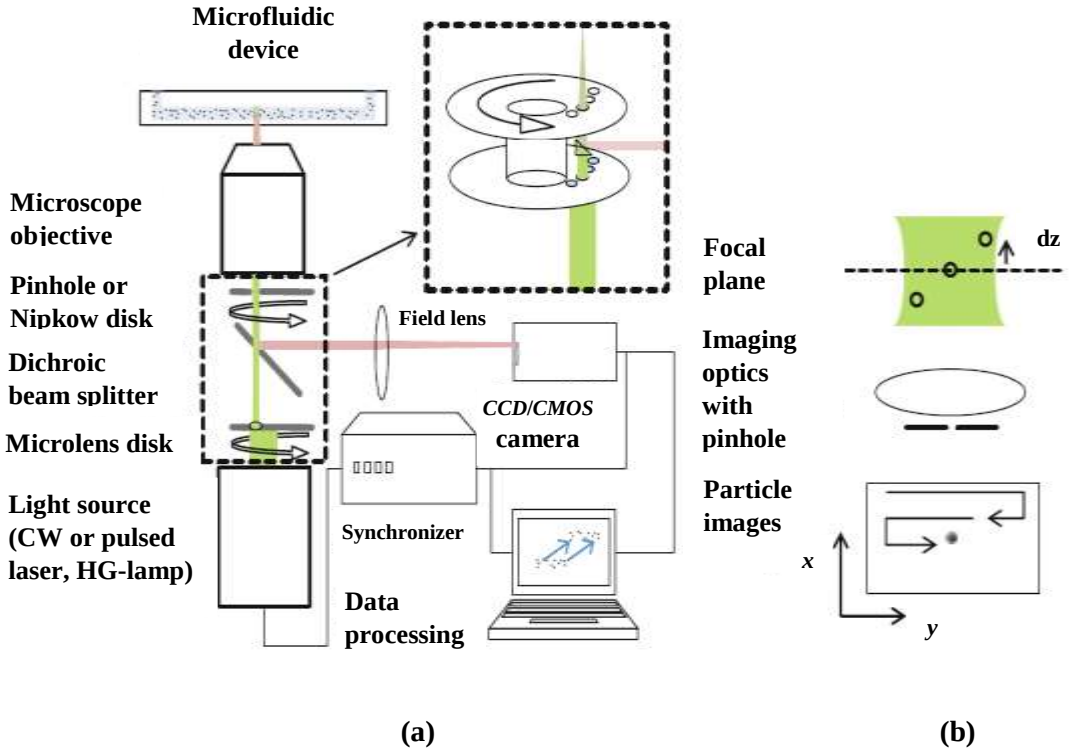

Figure 2. 5 a) Pointwise illumination using a Nipkow disk configuration in a confocal scanning microscopy Micro-PIV, **b)** The procedure of filtering out-of-focus particles from captured images (Markus *et al*., 2018).

c. Techniques Based on Out-of-Focus Imaging Without an Aperture

Methods based on out-of-focus imaging of particles are more common in 3D microfluidic measurements since confocal scanning microscopes are very expensive. These methods work based on the fact that particles that are away from the focal plane appear larger in particle images, as shown in Figure 2.6. A model was developed by Olsen and Adrian (2000) to estimate the correlation between the diameter of the particle image and its distance from the focal plane (z). This will be discussed in more detail in Chapter 3. The only assumption for this model is that the working distance of the microscope objective should be larger than the distance of the particle from the focal plane, which is true for almost all microscopes. Barnkob *et al.* (2015) also showed that by proper calibration, the diameter of a particle image can be correlated to its position from the focal plane.

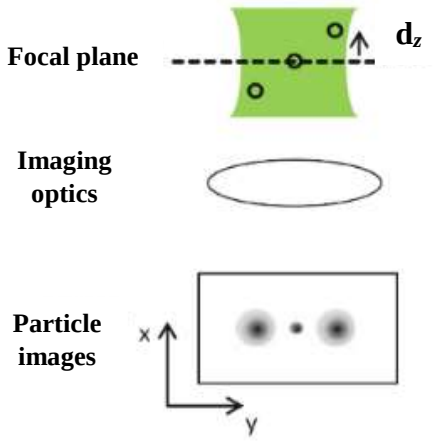

Figure 2. 6 The effect of out of focus particle on the diameter of particle images (Cierpka and Kähler, 2012).

The first implementation of out-of-focus imaging in defining the out-of-plane velocity component was by Stolz and Kohler (1994). They estimated the third velocity component of a particle by tracking its diameter change when moving in a 1.5 mm light sheet. They compared their measurement with LDA results and found only a 5% deviation between these two methods. Different strategies for out-of-focus imaging for 3D velocity measurements in micro-scale flows were developed by Ovryn and Hovenac (1993), Guerrero-vilamontes *et al*. (2006), Moreno-Hernandz *et al.* (2011), and Snoeyink and Wereley (2013).

d. Defocused Imaging with Aperture (3-Pinhole Technique)

Defocused imaging using a 3-pinhole aperture enables depth coding of out-of-focus particles. This technique was successfully used in microfluidic flows for the first time by Yoon and Kim (2006). The main difference from the original Micro-PIV is the aperture mask with three pinholes that is placed right after the objective lens (see Figure 2.7). Since the 3-pinhole aperture blocks the laser light, illumination is done from the other side of the channel. Using this optical configuration, out of focus particles appear as triplets depending on their position in the volume illumination. The distance between the edges of the triplets is directly proportional to the distance of the particle from the focal plane. The position of the particle relative to the focal plane (front or back) is defined by the mirrored arrangement of the triplet as shown in Figure 2.7 (b). Therefore, it is possible to distinguish the position of the particle in all three directions. This can be used to measure the 3D velocity in microfluidic devices. The low allowable seeding density and the low image intensity due to the small pinholes are the major limitations of this technique.

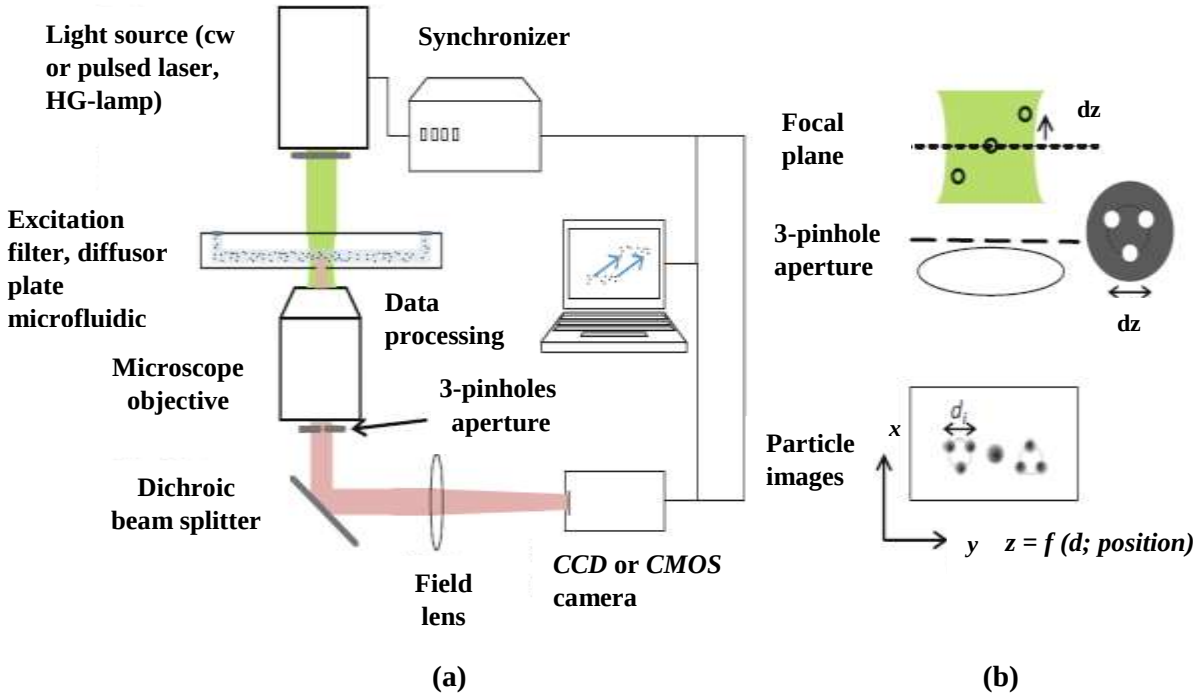

Figure 2. 7 a) The components of the 3-pinhole defocusing technique, **b)** the image of different particles based on their position relative to the focal plane using a 3-pinhole aperture (Markus *et al.*, 2018).

The main advantage of this technique over out-of-focus imaging methods without an aperture is easier processing of the particle images. As an application, Lu *et al*. (2008) used this method for in-vivo measurements of the beating heart of an embryonic zebrafish, and they were able to reconstruct the movement of the ventricle in their research.

2.2.2.2. Multi camera approaches

This section describes multi-camera 3D Micro-PIV systems.

a. Stereoscopic Imaging Micro-PIV

As in normal stereo PIV systems, the 3D velocity profile is obtained by observing the flow from two different viewing angles. Due to the small length scales of microfluidic systems, the optical set-up for different viewing angles is challenging and only two types of stereoscopic microscopes exist that are capable of this kind of measurement (Greenough and Common Main Objective (CMO) types). The CMO type is more common in microfluidic measurements as it provides large over-lapping in-focus regions due to the implementation of one large objective for both angles. The Greenough type uses a different objective for each viewing direction. Both techniques are shown in Figure 2.8.

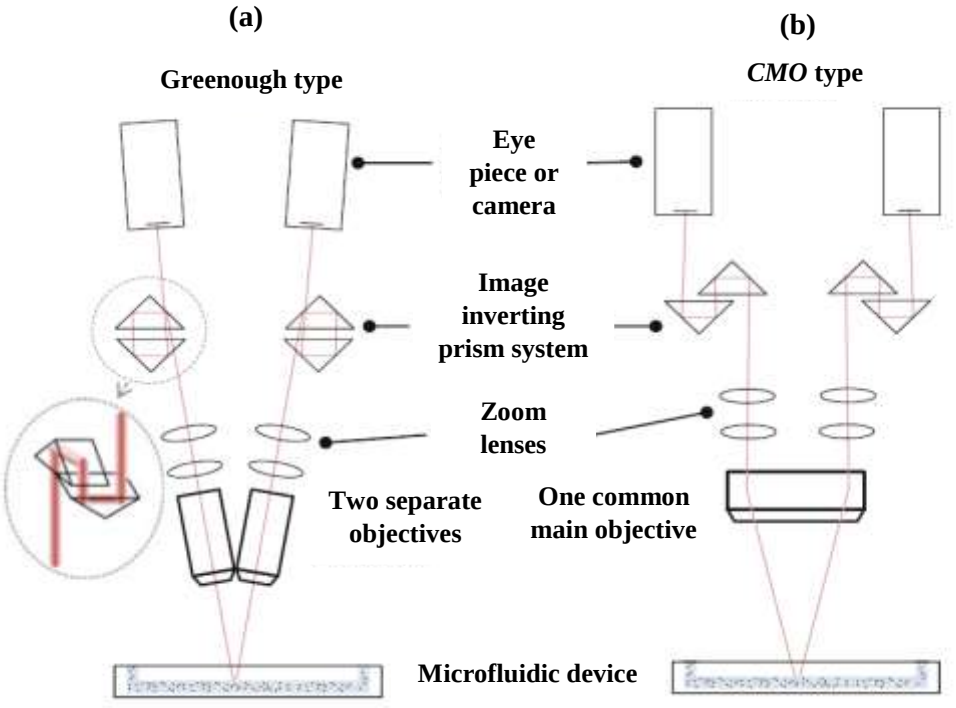

Figure 2. 8 Schematic of different types of stereoscopic microscopes. **a)** Greenough type with two separate objectives and **b)** CMO type with one common objective (Cierpka and Kähler, 2012).

The main disadvantage of the CMO type is the asymmetric distortion of the incident beams due to passing through the side of the large objective lens instead of its center. Once the particle images from two different viewing angles are obtained, the processing of images to calculate 3D velocity field is similar to conventional stereoscopic PIV. The first attempt at stereoscopic Micro-PIV was performed by Lindken *et al*. (2005). Due to the complicated calibration of stereo-Micro-PIV systems, it is usually preferable to use other 3D techniques.

b. Tomographic Micro-PIV

Tomographic Micro-PIV, uses a volume distribution of the particles to reconstruct recording images of the flow from different viewing angles (usually four different angles). The 3D velocity field is calculated by volumetric cross-correlation or volumetric tracking methods. The appearance of ghost particles in the reconstruction is the main limitation of this method which does not allow seed particle concentrations of more than 0.05 particles per pixel. Kim *et al*. (2011) used four different cameras to perform the first tomographic Micro-PIV measurement of the flow inside a droplet on a moving surface. Their experimental set-up is shown in Figure 2.9.

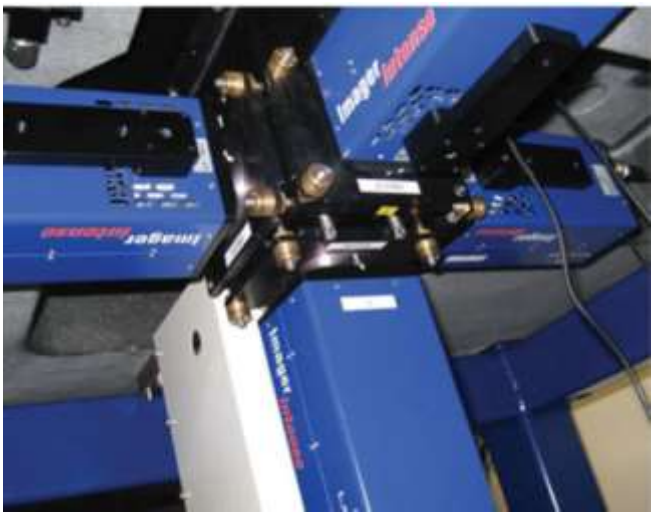

Figure 2. 9 The four-camera tomographic Micro-PIV set-up of Kim *et al.* (2011).

2.3. Summary

This chapter started by describing the early efforts by different research groups to visualize and measure microfluidic flows. All of them concluded that Micro-PIV is the most suitable technique for this purpose. Therefore, a literature review was specifically developed on Micro-PIV. This literature review comprised of two parts: first, the chronological development of Micro-PIV systems in terms of the achieved resolution of measurements (Table 2.1). Second, the enhancement of the Micro-PIV systems in terms of the components and design to achieve more complex measurements such as 3D and near-wall measurement.

This chapter serves as an introductory document about Micro-PIV to help readers grasp the complex theories associated to these systems easier. Some of these theories will be covered in Chapter 3.

CHAPTER 3: METHODOLOGY AND EXPERIMENTAL DESIGN

3.1. Introduction

This chapter presents the additional background on Micro-PIV that is required to understand the motivation behind this experimental work. It also justifies the selected values for the parameters of this experiment such as the size of the particles, the concentration of the particles, and the flow rate. These parameters were selected so that factors that typically create errors in Micro-PIV measurement, such as Brownian motion and particle visibility, have negligible effect on the measurements. This chapter begins with a brief overview of the cross-correlation function in Section 3.2. An understanding of the cross-correlation function is required to explain phenomena such as the DOC, which will be covered later in this chapter.

In Section 3.3, details of a typical Micro-PIV optical set-up and the procedure for creating volume illumination are described. The DOF and the DOC are two important phenomena related to volume illumination that are explained. A secondary effect of volume illumination is the visibility issue, which is discussed in the same section. It imposes an upper limit on the seed particle concentration due to the contribution of illuminated particles within the DOC.

In Section 3.4, Brownian motion is discussed and it will be shown that this effect imposes a lower limit on the size of the particles and the flow rate. Section 3.5 shows that the parameters of this experiment (flow rate, particle size, and particle concentration) are selected such that the effects due to visibility and Brownian motion are negligible. Therefore, if any unexpected deviations of results from the analytical solution are observed, DOC is the best candidate to explain that deviation.

In Section 3.6, the components of the Micro-PIV system (LA Vision GmbH) and the designed flow loop are briefly discussed. The rest of this chapter documents the preliminary image processing steps such as the calibration process, and selecting the most appropriate interrogation region, and the most suitable correlation scheme.

3.2. Cross-correlation

Both PIV and Micro-PIV use cross-correlation functions to calculate the particle displacements. This section explains the correlation function using 1D functions to illustrate the velocity

calculation procedure. The correlation of two functions is defined as the convolution product of those functions as shown below (Bastiaans, 1993).

$$f * g = c_{\mathrm{fg}}(\Delta x) = \int_{-\infty}^{+\infty} f(x)g(x + \Delta x)dx \tag{3.1}$$

For each shift (Δx) the correlation between these two functions can be calculated. The maximum of the correlation function occurs at a value of Δx that corresponds to a translation leading to the best overlap of the two functions. In order to show this more clearly, assume $f(x)$ and $g(x)$ are delta functions given by (Figure 3.1).

$$f(x) = \delta(x - x_{\mathrm{f}}) \quad , \quad g(x) = \delta(x - x_{\mathrm{g}}) \tag{3.2}$$

where x_f and x_g are the locations of the pluses on the x-axis as shown in Figure 3.1. Their correlation is calculated as follows:

$$C_{\mathrm{fg}}(\Delta x) = \delta\big(\Delta x - \Delta x_{\mathrm{fg}}\big), \tag{3.3}$$

where

$$\Delta x_{\mathrm{fg}} = x_{\mathrm{g}} - x_{\mathrm{f}} \tag{3.4}$$

Therefore, the correlation function has a peak at Δx_{fg} and is zero everywhere else (see Figure 3.1).

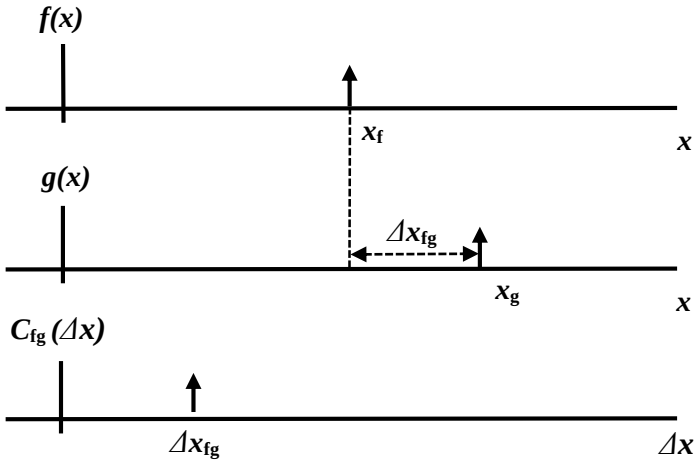

Figure 3.1 Cross-correlation of two Dirac delta functions.

The parameter Δx_{fg} in Figure 3.1 is the distance between the two delta functions as defined in equation (3.4). Therefore, the maximum value of the correlation defines the distance required to overlap one of the delta functions with the other. This same idea can be implemented for two 2D functions. Each interrogation region in an image of the flow that contains images of several particles is a 2D distribution of intensities.

By applying a 2D cross-correlation to the intensity distribution functions of the interrogation regions and finding the position of the maximum value ($\Delta x_{\mathrm{R_D}}$ and $\Delta y_{\mathrm{R_D}}$), the mean displacement of the particles in an interrogation region between the two exposures can be calculated. Since the time difference between the exposures is known, the average velocity for the particles inside the interrogation region can be obtained. This procedure is shown schematically in Figure 3.2. The mathematical expression for the 2D correlation can be written as (Wereley and Meinhart, 2010):

$$\Theta_{\mathrm{cc}}\left(\Delta x_{\mathrm{R_D}}, \Delta y_{\mathrm{R_D}}\right) = \int_{x=0}^{P}\int_{y=0}^{Q} f(x,y)g(x+\Delta x, y+\Delta y), \tag{3.5}$$

where P and Q denote the size of the interrogation window in the x and y direction, respectively. The image intensity functions in the first and second windows are denoted by f and g, respectively, and Δx and Δy are the displacement components in the correlation domain. The correlation graphs of this experiment are shown in Apendix C.

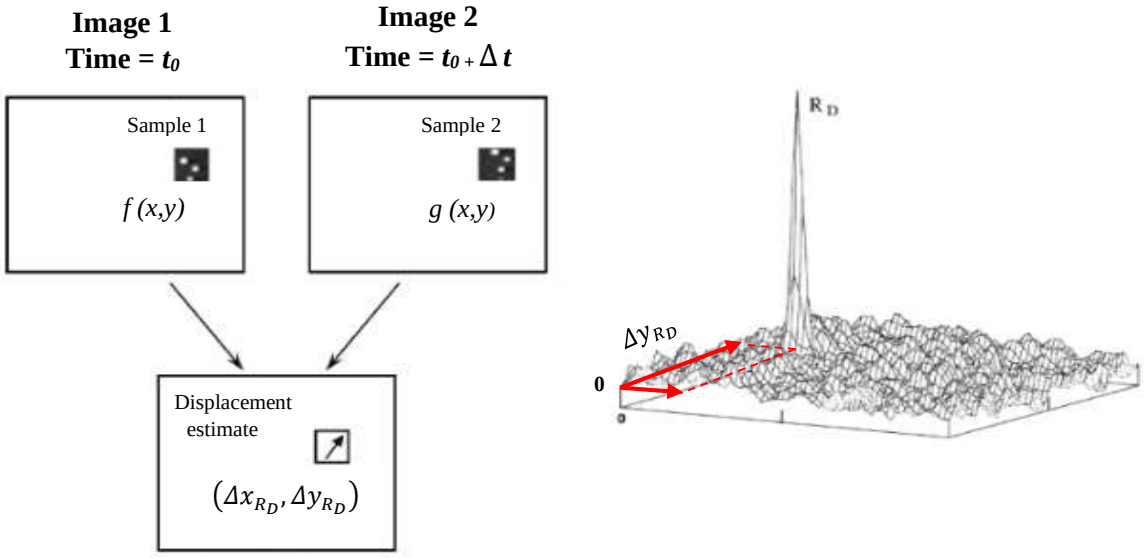

Figure 3.2 2D cross-correlation applied to the intensity distribution functions ($f(x,y)$ and $g(x,y)$) of interrogation regions in the first and second exposures (Markus *et al.*, 2018).

3.3. Volume illumination

In this section, volume illumination and the optics required to produce it are explained. One of the most complicated issues of Micro-PIV measurements results from the use of volume illumination. In volume illumination, instead of taking data from a thin, pre-defined 2D light-sheet as in regular PIV, data are taken from a 3D region in the flow field. Due to the limited optical access of microfluidic chips, illumination typically enters the flow through the same planar window through which the scattered light from the particles is collected. This optical set-up is called a back-scatter configuration (Markus *et al.*, 2018). A problem with this kind of illumination is that the light scattered from the window interface and other boundaries also enters the microscope objective and can overwhelm the scattered light from the seed particles. Since the wavelength of light emitted from the excited fluorescent particles is longer than the wavelength of the laser light, the noise from the back-scattered light can be filtered. This is achieved by a special optical configuration known as an epi-fluorescent prism cube which is shown inside the dashed-line region in Figure 3.3.

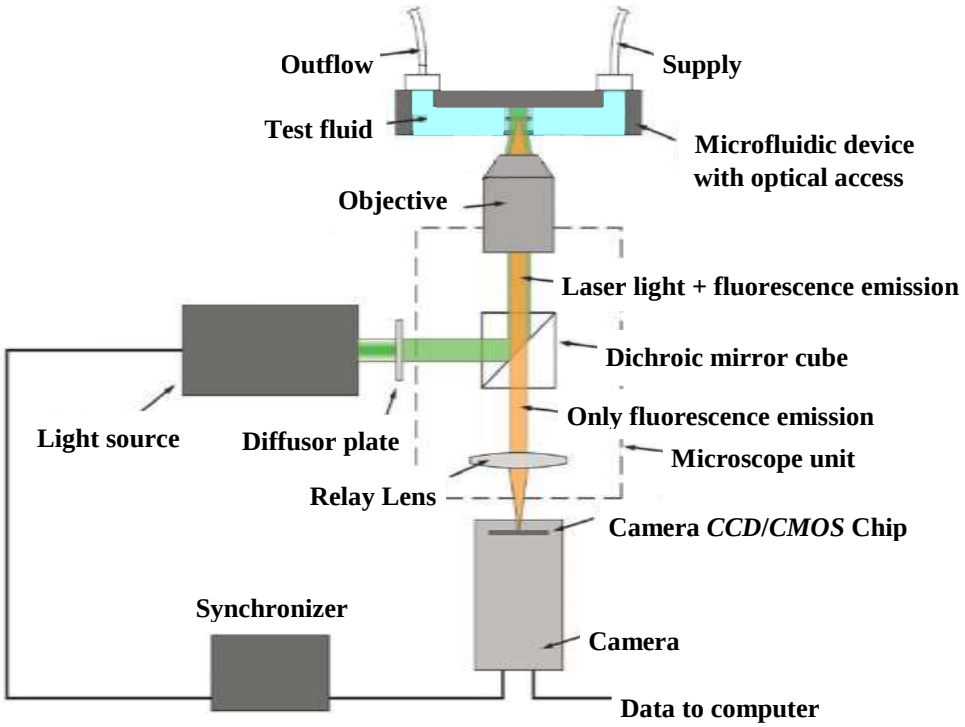

Figure 3.3 Optical configuration known as epi-fluorescent prism cube (the equipment inside the dashed line) that filters laser. Light reflecting back to the microscope from the scattered light of the excited fluorescent particles (Lindken *et al*., 2009).

As can be observed in Figure 3.3, the laser light first goes through a diffusor plate, which makes the laser light uniform. Next, the laser light is reflected by the dichroic mirror. The laser light is transmitted to the flow through the objective lens such that a hyperbolic volume of the test section is illuminated. This is shown in more detail in Figure 3.4. Seed particles in the hyperbolic volume of the laser light are excited and emit light at a longer wavelength than the laser light. The light scattered from the particles toward the microscope objective lens is collected by the same objective lens and reaches the epi-fluorescent filter cube. The dichroic mirror in the filter cube passes the high wavelength scattered light from the particles but filters the laser light. Therefore, only the scattered light from the particles reaches the camera through a relay lens and particle images are obtained.

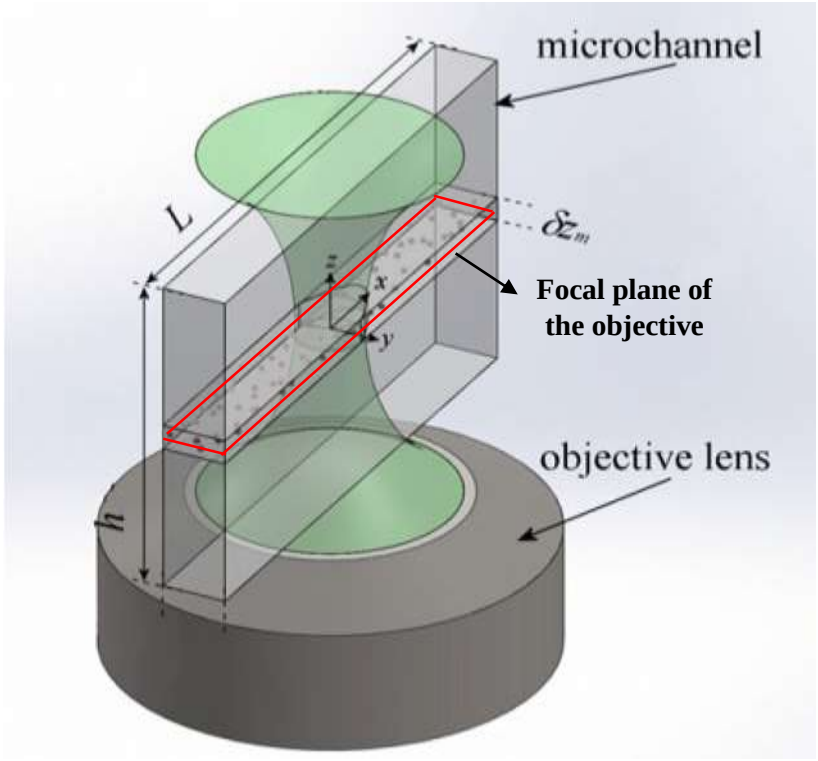

Figure 3.4 Volume illumination of microchannel through a microscope objective (Galindo-Rosales, 2017).

Depending on the distance of the particles from the focal plane of the lens, their images contribute differently to the correlation function. Particle images located outside the focal plane, appears broader and dimmer. At a certain distance from the focal plane, particle images will appear as background noise. Defining this distance has been a topic of considerable research in the last few decades. The parameter δ_z in Figure 3.4 illustrates the region of the flow domain in the *z* direction that will influence the image collected. Its value is closely related to the Depth of Correlation

(DOC) and Depth of Field (DOF) which will be described in the next section. Parameters *h* and *L* shows the depth of the microchannel and the length of the part of the microchannel which is in the objective domain, respectively. The following sections will clarify the difference between the DOF and the DOC.

3.3.1. DOF

The DOF is twice the distance from the object plane to the point at which the object is considered unfocused. The DOF, denoted by $\delta_{\mathrm{z_f}}$, is calculated as (Inoue, 1998):

$$\delta_{\mathrm{z_f}} = \frac{n\lambda_0}{NA^2} + \frac{ne}{NA.M}, \tag{3.6}$$

where n is the refractive index of the medium the objective lens is immersed in, λ_0 is the wavelength of light in a vacuum that is used for imaging, e is the smallest distance that can be resolved by the detector located at the microscope image plane, NA is the numerical aperture of the objective lens, and M is the objective magnification. For a CCD sensor, e is the spacing between pixels. Equation 3.6 includes both diffraction (first term) and geometric (second term) effects. Note that the DOF is independent of particle diameter and only depends on the objective lens.

3.3.2. DOC

The DOC is twice the distance that a particle can be positioned away from the focal plane of the objective such that its intensity on the image plane is a specified fraction, ε, of the intensity of the same particle positioned on the focal plane. Beyond this distance the particle's image will not affect the correlation function.

While the DOC is related to the DOF of the optical system, it is important to distinguish between them. Some particles may exist in the image that do not have acceptable quality and would be considered out of focus, yet they can contribute to the PIV correlation calculations. These particles are outside the DOF, but are considered to be within the DOC. Therefore, the DOF is not a complete description of the thickness of the measurement plane. The theoretical contribution of an unfocused particle to the correlation function is estimated by considering the effect due to diffraction, geometric optics and the finite size of the particle. The cutoff value for the image intensity, ε, is often assumed to be 0.1. This is because the correlation function depends on the square of the intensity, so a particle image with $\varepsilon = 0.1$ can be expected to contribute 1% to the

correlation function (Markus *et al*., 2018). Considering all three contributions to the correlation function and without going into details of the background optics theory, the DOC, denoted by $\delta_{z_{corr}}$, was defined mathematically by Olsen and Adrian (2000) as follows:

$$\delta_{z_{corr}} = 2\left\{\left(\frac{1-\sqrt{\varepsilon}}{\sqrt{\varepsilon}}\right)\left[\frac{{d_p}^2\left[\left(\frac{n}{NA}\right)^2-1\right]}{4} + \frac{1.49(M+1)^2\lambda^2\left[\left(\frac{n}{NA}\right)^2-1\right]^2}{4M^2}\right]\right\}^{1/2}, \quad (3.7)$$

where d_p is the particle diameter, *n* is the refractive index, *NA* is the numerical aperture of the objective, *M* is the magnification, and λ is the wavelength of the light used. In equation 3.7, it is obvious that $\delta_{z_{corr}}$ is strongly dependent on the *NA* and d_p and is only weakly dependent upon *M*. Also equation 3.7 shows that, unlike the DOF, the DOC is dependent on the particle size. The value of the DOC according to this analytical equation is calculated for both the 10x and the 20x objective lenses as 36.1 µm and 16.8 µm for 3 µm particles.

The value of DOC was also measured experimentally by Wereley and Meinhart (2005) for various optical configurations (*M* and *NA*) and particle size (d_p), and results are shown in Table 3.1.

Table 3. 1 Value of the DOC (µm) for various optical configurations (*M*, *NA*, *n*) and particle sizes (*d*p) (Wereley & Meinhart, 2005).

Optical configuration (M, NA, n) / ***d_p (µm)***	**(60, 1.4, 1.51)**	**(40, 0.75, 1)**	**(40, 0.6, 1)**	**(20, 0.5, 1)**	**(10, 0.25, 1)**
0.01	0.36	1.6	3.7	6.5	34
0.1	0.38	1.6	3.8	6.5	34
0.2	0.43	1.7	3.8	6.5	34
0.3	0.52	1.8	3.9	6.6	34
0.5	0.72	2.1	4.2	7.0	34
0.7	0.94	2.5	4.7	7.4	35
1	1.3	3.1	5.5	8.3	36
3	3.7	8.1	13	17	49

The estimated values of the DOC according to Table 3.1 for the measurements reported in this thesis (which uses 3 μm seed particles) are 17 μm to 49 μm for the 10x magnification and 17 μm for the 20x magnification. The reason for estimating a range instead of a single value for 10x magnification is because the optical configuration for the 10x magnification in this experiment is different from the ones provided in Table 3.1. The 10x objective lens used in these measurements has *NA* of 0.3 instead of 0.25 which lies between the *NA* of 0.25 and 0.5 that are available in Table 3.1. Bourdon *et al.* (2003) used a paraxial approximation and derived another expression for the DOC:

$$\delta_{Z_{corr}} = 2\left\{\frac{(1-\sqrt{\varepsilon})}{\sqrt{\varepsilon}}\left[\frac{{n_0}^2{d_p}^2}{4NA^2} + \frac{5.95\,(M+1)^2\lambda^2{n_0}^4}{16M^2NA^4}\right]\right\}^{1/2} \tag{3.8}$$

The parameters in equation 3.8 are the same parameters used in equation 3.7. The value of the DOC according to this analytical expression is calculated for both the 10x and the 20x measurements of this experiment as 38.4 μm and 19.8 μm, respectively.

Table 3.2 shows the DOC values obtained by Bourdon *et al*. (2004) experimentally for the same optical configurations and particle sizes used in Table 3.1.

Table 3. 2 Value of the DOC (μm) for various optical configurations (*M, NA, n*) and particle sizes (*d*p) (Bourdon *et al.*, 2004).

Optical configuration (M, NA, n) / d_p **(μm)**	**(60, 1.4, 1.51)**	**(40, 0.75, 1)**	**(40, 0.6, 1)**	**(20, 0.5, 1)**	**(10, 0.25, 1)**
0.01	2.1	2.1	2.1	2.2	2.3
0.1	2.1	2.2	2.2	2.3	2.9
0.2	2.2	2.4	2.6	2.8	4.3
0.3	2.3	2.8	3.1	3.5	5.9
0.5	2.6	3.7	4.3	5.0	9.4
0.7	3.1	4.7	5.7	6.7	13
1	3.9	6.4	7.9	9.3	18
3	10	18	23	27	55

The estimated values of the DOC according to Table 3.2 for this experiment which uses 3 μm seed particles are, 27 μm to 55 μm for 10x and 27 μm for 20x magnification. Table 3.1 and Table 3.2 show two different experimental studies by different research groups. It can be noticed that the trend for the measured DOC is similar for both Table 3.1 and Table 3.2 but, the DOC values for the same experimental condition in these two tables varies significantly. For the same optical configuration (each column), the value of the DOC increases with larger particles. Also for the same particle size (each row), the value of the DOC decreases with higher magnification.

The DOC value for the present experiment estimated from different analytical expressions (equations 3.7 and 3.8) and experimental data (Table 3.1 and Table 3.2) are shown simultaneously in Table 3.3.

As can be observed in Table 3.3, significant differences are observed between the DOC values obtained for 10x and 20x measurements of this experiment. This illustrates the challenge and ambiguity of DOC measurement and calculation.

Table 3. 3 Value of the DOC for this experiment based on various theoretical and experimental methods.

Researchers	**Calculated DOC**
Olsen & Adrian, 2000 Analytical (Equation 3.2)	**10x (*NA* = 0.3) :** 36.1 μm **20x (*NA* = 0.5):** 16.8 μm
Bourdon *et al*., 2003 Analytical (Equation3.3)	**10x (*NA* = 0.3):** 38.4 μm **20x (*NA* = 0.5):** 19.8 μm
Wereley & Meinhart, 2005 Experimental (Table 3.1)	**10x (*NA* = 0.3):** 17 μm to 49 μm **20x (*NA* = 0.5):** 17 μm
Bourdon *et al*., 2004 Experimental (Table 3.2)	**10x (*NA* = 0.3):** 27 μm to 55 μm **20x (*NA* = 0.5):** 27 μm

3.3.3. Particle visibility

Another issue related to volume illumination is the particle visibility. The scattered light from out-of-focus particles can degrade the images of the in-focus particles. Filtering the noise from the out-of-focus particles is not as simple as filtering the noise resulting from the laser light reflections, as they have same wavelength as the excitation light (Santiago *et al*., 1998). The literature suggests

that seed particle concentration and the channel depth should be adjusted to minimize the effect of this issue. Olsen and Adrian (2000) defined particle visibility (v) as the ratio of the intensity of a focused particle image to the average intensity of the background light produced by the unfocused particles. v is calculated as follows:

$$v = \frac{I(0,0)}{I_B} = \frac{4M^2\beta^2(z_0-a)(z_0-a+L)}{\pi CLZ_0{}^2\left\{M^2 d_p{}^2+1.49(M+1)^2\lambda^2\left[(\frac{n}{NA})^2-1\right]\right\}}, \tag{3.9}$$

where $I(0,0)$ is the intensity of the focused particles, I_B is the average intensity of the background noise, β is the cutoff level parameter which defines the edges of the particle image (β =1.91), L is depth of the microfluidic device, M is the magnification of the objective lens, d_p is the seed particles diameter, λ is the wavelength of the light used for imaging, n is the reflective index of the medium, a is used to represent offsets from the centre-plane, z_0 is the working distance of the objective, and C is the seed particle concentration (number of particles per unit volume of the fluid). For the centre-plane measurement the value of a is equal to $L/2$. Note the inverse relation of v with C and L in equation 3.9. Also, for a fixed C, v increases for smaller particles (d_p) or larger NA. The dependence of v on M is weak. Equation 3.9 can be rearranged to give the particle volume fraction (v_{fr}) as a function of v as shown below.

$$v_{fr} = \frac{2d_p{}^3M^2\beta^2(Z_0-a)(Z_0-a+L)}{3vLz_0{}^2\left\{M^2 d_p{}^2+1.49(M+1)^2\lambda^2\left[\left(\frac{n}{NA}\right)^2-1\right]\right\}} \tag{3.10}$$

It worth noting that v_{fr} is equal to the volume of a particle multiplied by C. Practically, it was shown that for high quality Micro-PIV measurements a value of $v > 1.5$ is required (Werele and Meinhart, 2010). Therefore, by substituting 1.5 for v in equation 3.10, the maximum allowable concentration of seed particles in order to have an acceptable Micro-PIV images in terms of visibility can be obtained. As an example, Table 3.4 shows the maximum allowable concentration of particles for a 100 µm deep channel.

In general, for a constant particle size, a thinner channel depth allows for a higher concentration of seeding particles. This enhances the quality of the Micro-PIV measurements. Decreasing the thickness of the device decreases the number of unfocused particles, while the number of focused particles remains constant. In order to reduce errors due to the visibility, the microchannel in this thesis was designed to be thin (depth of 40 µm) which enables the maximum

seeding particle concentration available without any dilution ($v_{\mathrm{fr}} = 1\%$ for both 10x and 20x magnifications).

Table 3. 4 Maximum v_{fr} in a 100 μm deep microchannel in order to keep v = 1.5 (Wereley & Meinhart, 2010).

Optical configuration (M, NA, n) / ***d_{P} (μm)***	**(60, 1.4, 1.51)**	**(40, 0.75, 1)**	**(40, 0.6, 1)**	**(20, 0.5, 1)**	**(10, 0.25, 1)**
0.01	2.0E-5	4.3E-6	1.9E-6	1.1E-6	1.9E-7
0.1	1.7E-2	4.2E-3	1.9E-3	1.1E-3	1.9E-4
0.2	1.1E-1	3.1E-2	1.4E-2	8.2E-3	1.5E-3
0.3	2.5E-1	9.3E-2	4.6E-2	2.7E-2	5.1E-3
0.5	6.0E-1	3.2E-1	1.8E-1	1.1E-1	2.3E-2
0.7	9.6E-1	6.4E-1	4.1E-1	2.8E-1	2.3E-2
1	1.5E+0	1.2E+0	8.7E-1	6.4E-1	1.7E-1
3	4.8E+0	4.7E+0	4.5E+0	4.2E+0	2.5E+0

3.4. Brownian motion

Brownian motion is the random thermal noise of particles that are suspended in a fluid. This random motion is more substantial if the particles are small or the flow is slow (e.g. flow velocities of the order of μm/s) (Lindken *et al*., 2009) . The effect of Brownian motion on the correlation function would appear as a spread of the correlation peak, which makes its detection among noise peaks more difficult (Olsen and Adrian, 2000). The extent of the spread of the correlation peak is proportional to the temperature of the flow. Therefore, this spreading of the correlation signal peak can be used to measure temperature, allowing for simultaneous measurement of velocity and temperature in Micro-PIV. Oslen *et al*. (2000) showed that the effect of Brownian motion on the correlation peak also affects the DOC, as shown below:

$$\delta_{\mathrm{z_{corr}}} = \delta_{\mathrm{z_{corr_0}}} \times \left(1 + \frac{8M^2\beta^2 D\Delta t}{M^2 {d_{\mathrm{p}}}^2 + 5.95(M+1)^2\lambda^2 {f^{\#}}^2}\right)^{1/2} \tag{3.11}$$

where $\delta_{z_{corr_0}}$ is the DOC without the effect of Brownian motion, M is the magnification of the objective, β is the same cut-off level parameter used in equation 3.9 ($\beta^2 = 3.67$), D is the diffusion coefficient, Δt is the time difference between two frames, d_p is the diameter of the particles, λ is the wavelength of the light and $f^\#$ is the f number of the lens which is defined as the ratio between the focal length f and the aperture diameter D_a. The second part of equation 3.11 represents the contribution of the Brownian motion to the DOC. When $\frac{8M^2\beta^2 D\Delta t}{M^2 {d_\mathrm{p}}^2 + 5.95(M+1)^2\lambda^2 {f^\#}^2}$ is close to zero, the effect of Brownian motion on DOC can be ignored. This parameter is calculated to be 7.87×10^{-5} and 6.51×10^{-5} for 10x and 20x magnifications datasets in this experiment, respectively. These value are close to zero, therefore the effect of Brownian motion on the DOC value is estimated to be negligible in this experiment.

The controlling parameters of the Brownian motion are the size of the seed particles and the time interval between the two exposures (Wereley *et al*., 2010). Increasing the size of the seed particles and increasing the time interval between two frames decreases the errors due to Brownian motion. Santiago *et al*. (1998) was the first to quantify the error due to Brownian motion. The mean square distance traveled by a particle due to diffusion can be calculated as

$$S^2 = 2D\Delta t\,, \tag{3.12}$$

where Δt is the time difference between the two exposures and D is the diffusion coefficient given by

$$D = \frac{kT}{3\pi\mu d_\mathrm{p}}\,, \tag{3.13}$$

where k is Boltzmann's constant, T is the absolute temperature, μ is the dynamic viscosity and d_p is the particle diameter. The velocity of a particle that travels a distance Δx in the time interval Δt can be approximated by

$$u = \frac{\Delta x}{\Delta t}\,, \tag{3.14}$$

Therefore, the error due to Brownian motion is equivalent to

$$\varepsilon_B = \frac{\langle S^2\rangle^{1/2}}{\Delta x} = \frac{1}{u}\sqrt{\frac{2D}{\Delta t}}\,, \tag{3.15}$$

As can be seen from equations 3.13 and 3.15, increasing the particle size decreases the diffusion coefficient and therefore the error due to Brownian motion. Also, by increasing Δt, the flow displacement increases proportional to Δt, so the root mean square of the particle displacement grows as $\Delta t^{1/2}$.

In practice, Brownian motion is an important consideration for 50 nm to 500 nm particles with characteristic flow rates of less than approximately 20 µL/hr (Wereley *et al*., 2010). Therefore, for the selected value of the parameters in the thesis research (particle size of 3 µm and average flow velocity 100 µL/hr), the errors due to the Brownian motion are not present in the measurements.

3.5. Experimental parameters

In the previous sections, phenomena that contribute to the errors in Micro-PIV measurements, i.e. the DOC, particle visibility and Brownian motion, were introduced. Also, the critical values of different parameters required to minimize these source of errors were discussed. The experimental parameters were chosen such that errors minimally affected the measurements. Table 3.5 shows the source of errors, their active range and the value used in this experiment for those parameters.

Table 3. 5 Assessment of the errors and experimental parameters in the present measurements.

Source of error	**Critical value**	**Value of Parameters used in the experiment**	**Comment**
Brownian motion	$\boldsymbol{d_p}$**:** 500 nm $\boldsymbol{Q}$**:** 20 µL/hr	$\boldsymbol{d_p}$**:** 3 µm $\boldsymbol{Q}$**:** 100 µL/hr	**No effect**
Particle visibility	Maximum v_{fr} for depth of 40 µm (equation 3.5): **10x:** 2.13% **20x:** 3.85%	$\boldsymbol{v_{fr}}$**:** 1%	**No effect**
DOC	According to Table 3.3 DOC changes from 16.8µm to 55µm	$\boldsymbol{M}$**:** 10x and 20x $\boldsymbol{d_p}$ **:** 3 µm	**Possible effect**

As can be observed in Table 3.5, errors due to Brownian motion and particle visibility are negligible for the experiment performed in this thesis but, the error due to the DOC is not negligible. The minimum value of the DOC estimated (16.8 μm) is too large compared to the microchannel's depth (40 μm).

3.6. Components of the experimental set-up

A detailed description of experimental set-up including the Micro-PIV system and the flow loop is presented in this section.

3.6.1. Micro-PIV system

The major components of the Micro-PIV system are indicated by the letters (a-h) in Figure 3.5.

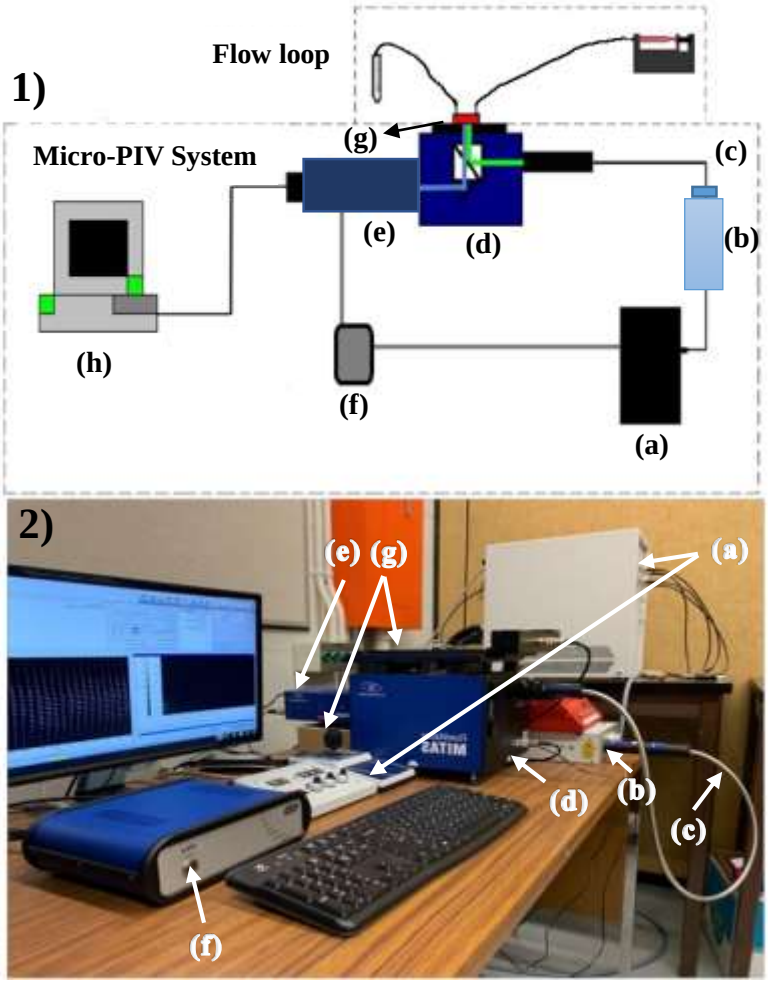

Figure 3.5 Components of LA Vision Micro-PIV system: **1)** schematic, and **2)** photograph.

LA Vision's MITAS Micro-PIV was used to measure the velocity field. The system consists of:

a) Laser control, power and cooling reservoir unit

b) Litron Nano-PIV series Nd:YAG laser (New Wave Research, USA); (Maximum energy of 30 mj/pulse at a wavelength of 532 nm with a maximum pulse rate of 15 Hz).

c) Fiber optics which allows convenient configuration of the system due to its flexibility

d) MITAS fluorescent microscope (La Vision GmbH, Germany)

e) Image intensifying CCD camera (La Vision GmbH, Germany); 1376 × 1040 pixel progressive scan CCD sensor (12 bit digital, dual frame technique), double shutter with minimum 500 ns inter-framing time, pixel size of 6.45 × 6.45 μm^2 and recording rate of 10 frames/s at 16 MHz read-out rate with digital frame grabber.

f) Programmable triggering unit (PTU)

g) Moving stage coupled with microscope; (Computer-controlled translation stage with resolution of 0.05 μm in 3 directions (*x*, *y*, *z*). An external joy-stick is also provided for the axis control of the stage.)

h) Computer

3.6.2. Flow Loop

The major components of the flow loop are shown in Figure 3.6.

a) Syringe pump (NE-300 Just Infusion^{TM} Syringe Pump)

Flow is supplied by a high precision syringe pump. Flow rates ranging from 0.73 μL/hr to 1.5×10^6 μL/hr are possible depending on the size of the syringe used. A solution of deionized water and fluorescent seed particles (1% volume fraction) was injected at a flow rate of 100 μL/hr. Polysterene fluorescent coated seed particles were used in this experiment which have density of 1.05 g/cm^2 and temperature stability of up to 100 ˚C.

b) Syringe (Hamilton Gastight with removable needles)

A 50μL barrel capacity syringe was selected for this experiment, which is the smallest syringe available that can inject the desired flow rate of 100 μL/hr. A 26-gauge small hub removable needle was chosen to fit the Tygon tubing.

c) Tubing (23 gauge Tygon tubing)

The tubing is flexible in order to integrate the microchannel into the Micro-PIV system. In order to reduce the pressure drop in the system, the shortest amount of tubing is used. The tubing had a 1.58 mm outer diameter and 0.51 mm inner diameter.

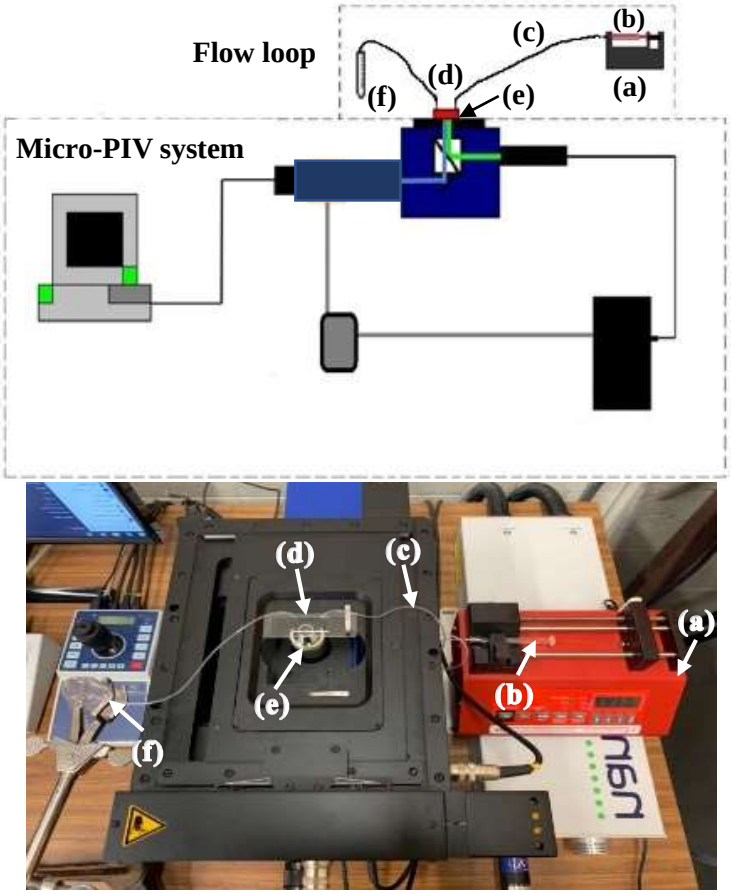

Figure 3.6 Components of the flow-loop shown in both **1)** photograph, **2)** schematic of the whole set-up which shows how the flow loop is placed relative to the Micro-PIV system.

d) Test section (Microchannel)

Microchannels were fabricated from PDMS (Polydimethylsiloxane), specifically Slygard-184. The channels have a rectangular cross-section with nominal dimensions of 40 × 110 μm^2 (1:2.5). The entrance length was calculated to be on the order of the hydrodynamic radii of the channel (58.67 μm). The data were taken at least 100 entrance lengths away from the inlet to ensure the flow is fully developed.

e) Microscope objectives

The specifications of the available objectives (10x and 20x magnifications) are given in Table 3.6.

Table 3. 6 Specifications of the objective lenses (10x and 20x magnifications) used in the present experiment.

M	***NA***	**FOV**	**DOF**	**Working distance**
10x	0.3	600 × 450 μm^2	7 µm	5.5 mm
20x	05	300 × 225 μm^2	4 µm	7.9 mm

f) Container

The outlet of the tubing is placed in a container so, the solution of deionized water and tracer particles can be collected and reused.

All parts of the set-up must be perfectly sealed. Therefore, a leak test was performed before data collection. Also, bubbles should not be present in the system. Once all these steps are checked, the flow is generated by turning on the syringe pump. The data are taken a few minutes after that the syringe pump is working to ensure that there are no instabilities in the generated flow due to starting the pump.

3.7. Calibration

A calibration procedure is required to convert the image pixel data to distances. For this purpose, a single plane calibration target plate with known dot spacing (0.02 to 0.3 mm) was used (see Figure 3.7). Since the distances between dots are known, once the image of the plate is captured by the camera, the calibration is readily done in the DAVIS software. After the calibration is performed, a bar is added to a side and bottom edge of each image in the software showing the distance in micrometers from an arbitrary reference point. Figure 3.7 shows the custom LA vision Micro-PIV calibration plates.

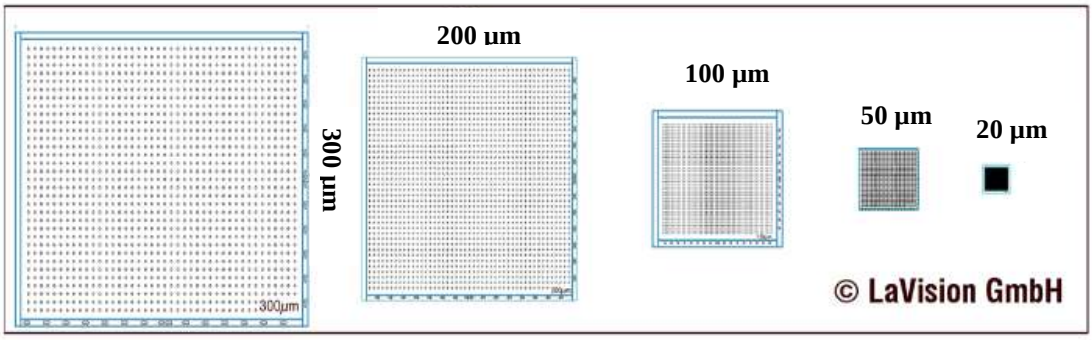

Figure 3. 7 Calibration plate of the LA Vision Micro-PIV system.

3.8. Interrogation region

As mentioned in Chapter 1, PIV images are divided into small interrogation regions. Instead of tracking the movement of each particle individually, the movement of a group of particles in the same interrogation region is tracked. The selection of the interrogation region size and shape is of critical importance. The size of the interrogation region should be chosen such that each interrogation region contains between 5 to 15 particles (Jahanmiri, 2011). Different interrogation region shapes can be selected in the DAVIS software. There are three popular choices: square, ellipse with an aspect ratio of 2 and ellipse with an aspect ratio of 4, as shown in Figure 3.8. According to Behboudi (2015), the shape of the interrogation region does not have a significant effect on the Micro-PIV results. However, selecting the right size for the interrogation region is critical (Behboodi 2015) as will be explained in the next section.

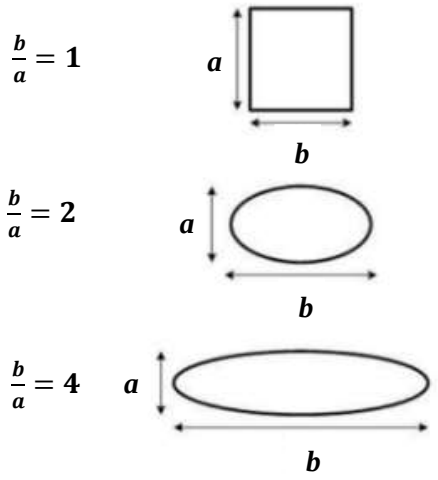

Figure 3. 8 Popular shapes for the interrogation region.

For the present measurements, square interrogation regions were selected due to its simplicity. The optimal size of the interrogation regions are obtained by a trial and error process. For both 10x and 20x magnifications, 32 × 32 pixel interrogation regions proved to be the optimal size. This follows the rule of 5 to 15 particles per interrogation region almost everywhere in the channel domain (Jahanmiri, 2011). Figure 3.9 shows the channel divided into square interrogation regions for 10x magnification.

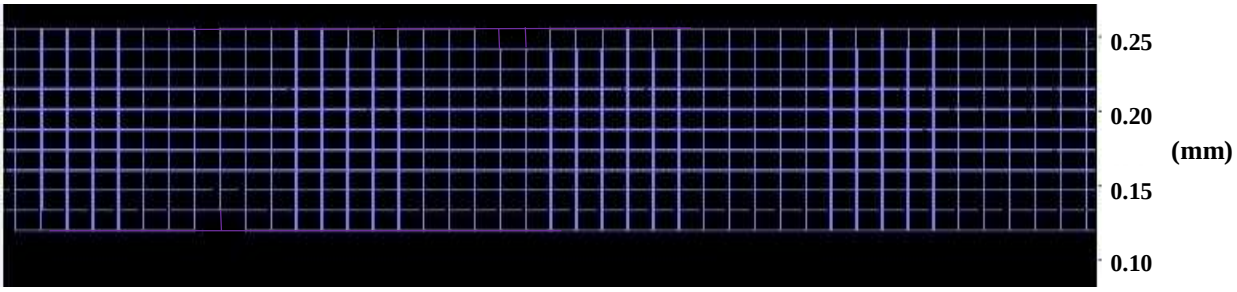

Figure 3.9 The channel domain divided into 32 × 32 pixels square interrogation regions in 10x magnification.

The process of locating the channel walls is described in the next section. A velocity vector will be calculated for each of the interrogation regions in Figure 3.9. Therefore, the size of the interrogation region also defines the resolution of the measurements.

3.9. Processing of Micro-PIV images

Image processing is an important stage in Micro-PIV experiments. Processing has multiple steps starting with a detailed assessment by the user to determine whether the images quality is sufficient to be processed by the Micro-PIV software. Defining the proper size of the interrogation region and choosing the right cross-correlation scheme (single pass or multi-pass) are some of the other considerations. The first Micro-PIV images of this experiment, for both 10x and 20x magnifications, are shown in Figure 3.10.

Image pre-processing using sliding minimum subtraction algorithm (Behboudi, 2015) was tested on both the 10x and 20x images to decrease the background noise. The processed results did not show noticeable enhancement for the present experiments. As will be discussed in Chapter 4, this is due to the large DOC compared to the height of the microchannel. Therefore, almost all the particles in the images affect the cross-correlation operation.

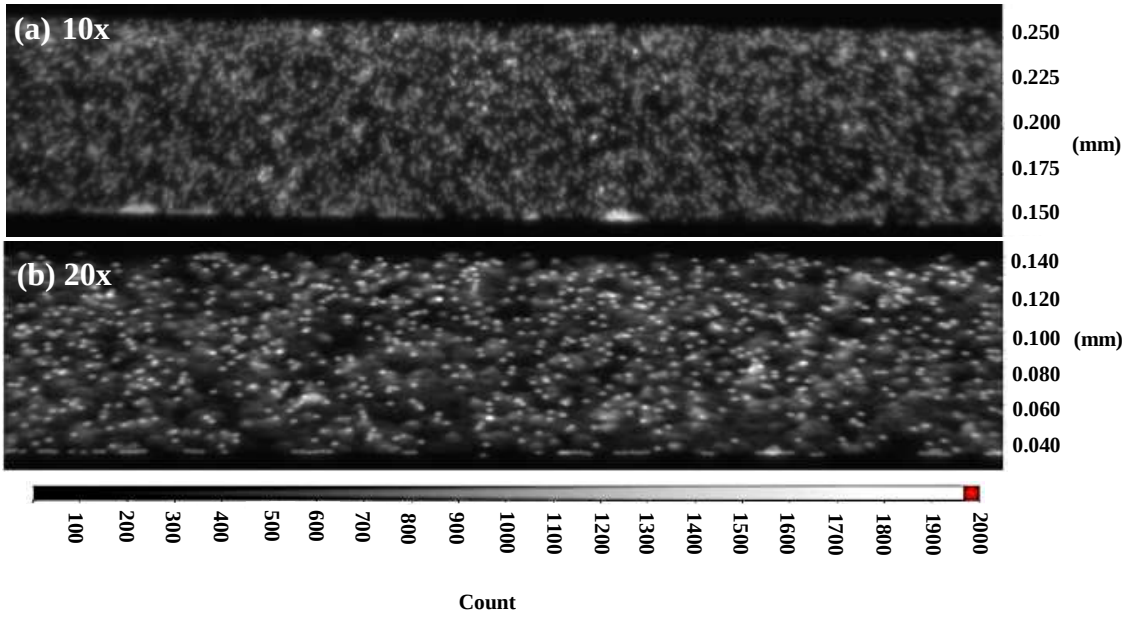

Figure 3.10 Particle images for **a)** 10x, and **b)** 20x lenses. "count" refers to the pixel intensity.

The channel width measured as 110 µm and 109 µm in the 20x and 10x calibrated images of Figure 3.10, respectively. The position of the wall is assumed to be at the furthest distance from the channel center-line with stationary particles, i.e. particle attached to the wall. The measured width of the microchannel shows that the microchannel was fabricated close to its design width of 110 µm, with relatively small tolerances.

For accurate results the particle size in the Micro-PIV images should be 3 to 5 pixels in diameter. In the current Micro-PIV images, in-focus particles are between 3 and 5 pixels in both 10x and 20x images, respectively. Out of focus particles may appear much larger. Another important issue in Micro-PIV images is that particles should not stick to each other. An agglomeration of particles may not follow the flow faithfully due to its larger size. The fluorescent particles used in this experiment are packaged in deionized water with trace amounts of surfactants that inhibit aggregation of particles. Except for a few regions near the walls, the particles are well separated, which allows for acceptable processing. The images in Figure 3.10 were obtained after a long trial and error process to satisfy all the mentioned criteria. The particle images were then processed using the DAVIS 8.2 software. The domain of the processing was limited to the microchannel's inner area by performing geometric masking operation.

The optimal size for the interrogation regions was chosen to be 32×32 pixels for both the 10x and 20x images as explained in the previous section. A multi-pass cross-correlation was used

for processing. In the multi-pass cross-correlation, the size of the interrogation regions are first selected to be bigger (usually twice the size) and a velocity vector is calculated for each large interrogation region using a standard cross-correlation. For the second pass, the interrogation regions are reduced in size and shifted an amount equivalent to the displacement calculated in the first pass. A standard cross-correlation is then applied to the translated interrogation regions. Smaller velocity vectors will be calculated in the second pass. The total velocity vector for the original interrogation regions will be the sum of the calculated velocities for all passes. Other processing schemes include multi grid correlation, central difference interrogation correlation and image deformation correlation (Pan, 2006). Use of a multi-pass cross-correlation enhances the accuracy of the velocity calculations. A two pass cross-correlation using 64×64 pixel and 32×32 pixel interrogation regions was selected for both the 10x and 20x images. A 50% overlap of interrogation regions was used for both passes. The reason for this overlapping is to increasing the spatial resolution of the measurements.

Finally, some vector post-processing operations were performed. The calculated vector is typically corrected if that specific vector is detected by the software to be out of the expected range. In this experiment a simple vector post-processing scheme was chosen such that if the software was unable to calculate the velocity vector for an interrogation region due to reasons such as low correlation, lack of particles, etc., a velocity vector will be assigned to that interrogation region by interpolating neighboring vectors. Peak-locking was also checked for the measured instantaneous velocity fields.The details of the peak-locking analysis for both the 10x and the 20x magnification data are covered in Apendix D.

3.10. Summary

In this chapter the parametric design of the experiment is discussed. It was shown that for the selected value of the experimental parameters such as the seed particle size (d_p= 3 μm), the flow rate (Q =100 μL/hr) and the concentration of seed particles for the channel depth of 40 μm (v_{fr}= 1%), the errors due to visibility and Brownian motion are negligible. Also, it was realized that the value of the DOC obtained for the designed experiment varies significantly based on different research group's analytical and experimental studies for both 10x and 20x magnifications (Table 3.3). This made the analysis of the effects due to the DOC in the final results more complicated, which will be covered in Chapter 4.

Once the parametric design of the experiment was completed, the measurement tool (LA Vision Micro-PIV system) and the equipment used (Flow loop) were described. The final step to obtain preliminary Micro-PIV instantaneous velocity fields (which are shown in Chapter 4) was to select appropriate parameters within the DAVIS software to process the images. The selection procedure of these parameters for both 10x and 20x measurements such as the interrogation region (32×32 pixel square interrogation region), pre-processing scheme (not used for this experiment as explained), processing scheme (two-pass cross correlation with 50 % overlap of interrogation region) and post-processing scheme (linear interpolation of neighboring vectors) were explained in the final part of this chapter.

CHAPTER 4: RESULTS AND DISCUSSION

In this chapter, the results of processing the Micro-PIV images are presented and the importance of considering the DOC in Micro-PIV data processing will be highlighted. In section 4.1, the theoretical velocity profile for low Reynolds number flow of a Newtonian fluid in a rectangular cross-section microchannel is presented. This will later be compared to the experimental data. In Section 4.2, a preliminary instantaneous velocity field calculated from one pair of images is discussed. Section 4.3 presents some background on the spatial and time averaging techniques to be used. Section 4.4 explains why averaging is required. The DOC was discussed in Chapter 3, where it was shown that defining an exact value for the DOC is challenging. Different values of the DOC were reported for the same objective lens and particle size according to Table 3.3. In Section 4.5, a special averaging scheme will be applied to the analytical solution to account for the DOC. The sensitivity of the measurements to flow fluctuations is assessed in Section 4.6. Finally, near-wall measurements and the sources of error affecting measured velocity profiles in near-wall regions are discussed in Sections 4.7 and 4.8, respectively.

4.1. Analytical solution

In this section, an analytical solution for the investigated flow is discussed. Low Reynolds number fully developed flow of a Newtonian fluid in a rectangular cross-section microchannel (or duct) is studied in this experiment. Since the non-linear convection terms are negligible in this flow regime, the Navier-Stokes equations reduce to a Poisson equation,

$$\frac{\partial^2 u}{\partial y^2} + \frac{\partial^2 v}{\partial z^2} = -\frac{1}{\mu}\frac{\partial p}{\partial x} \tag{4.1}$$

where μ is the dynamic viscosity and $\frac{\partial p}{\partial x}$ is the pressure gradient along the channel. The coordinates *y* and *z* are aligned with the height and span of the channel cross-section, respectively. The boundary conditions are shown in Figure 4.1.

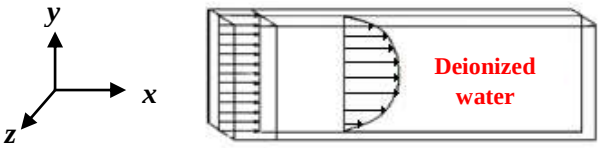

At $y = \pm\frac{w}{2}$, $u=0$ and At $z = \pm\frac{b}{2}$, u = 0

Figure 4. 1 schematic of the microchannel and the boundary conditions for this flow.

Using a Fourier series expansion, the expression for the velocity profile u (y,z) is (Tabeling, 2005)

$$u(y,z)_{\mathrm{x}} = \frac{4}{\mu w}\left(-\frac{\partial p}{\partial x}\right)\left[\sum_{n=1}^{\infty}\frac{(-1)^{n+1}}{{B_{\mathrm{n}}}^{3}}\left(1-\frac{\cosh B_{\mathrm{n}} y}{\cosh\frac{B_{\mathrm{n}} h}{2}}\right)\cos(B_{\mathrm{n}} z)\right], \tag{4.2}$$

where w is the width of the channel, h is the height of the channel, and B_{n} is given by

$$B_{\mathrm{n}} = (2n-1)\frac{\pi}{w}, \tag{4.3}$$

This 3D velocity profile is shown in Figure 4.2 (for more information refer to Appendix A).

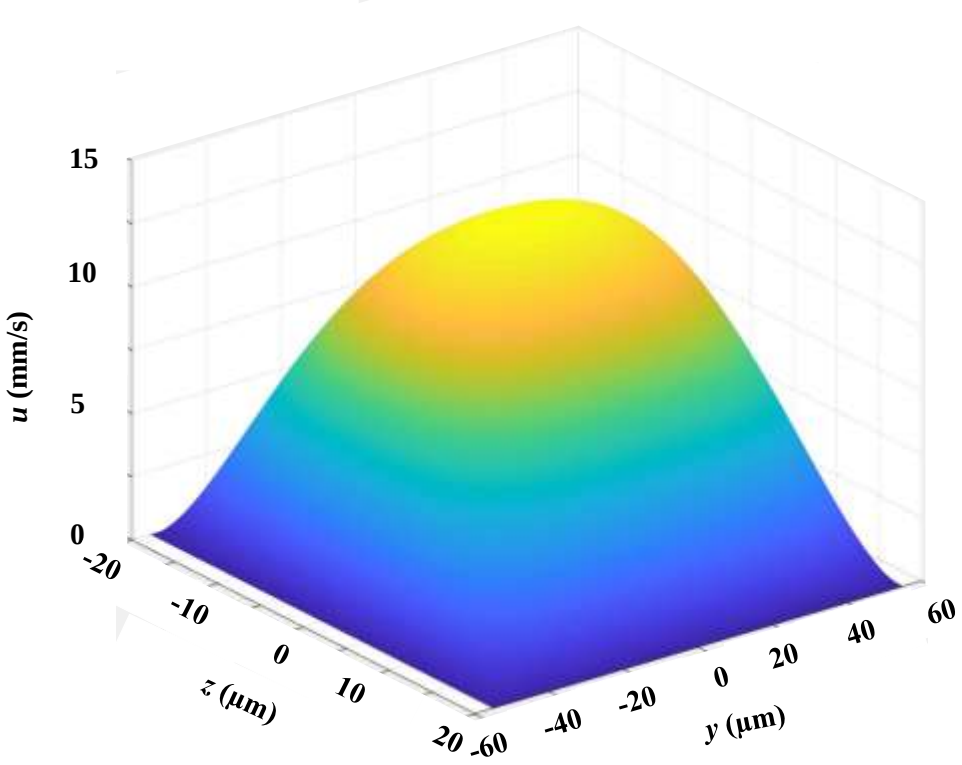

Figure 4.2 3D analytical velocity profile in a rectangular cross-section microchannel.

The velocity profile shown in Figure 4.2 is calculated over a plane section. For each plane perpendicular to the cross-section of the channel a specific 2D velocity profile *u(y)* can be extracted. This analytical solution will be used to verify the experimental data.

4.2. Instantaneous results

Images obtained for both 10x and 20x magnifications (Figure 3.11) were processed using different interrogation region (sizes and shapes), processing schemes and seed particle concentration and size. The most appropriate options selected in this trial and error process were described in Section 3.9 (two-pass regular cross-correlation starting from 64×64 pixel to 32×32 pixel square interrogation regions and seed particle concentration of 1% volume fraction). An example of the results for both the 10x and 20x images are shown in Figure 4.3. In this figure, velocity vectors are shown for every 4 interrogation regions in the *x* direction for the 10x image and every 8 interrogation regions in the 20x image. The distance between the original vectors in the *y* direction is filled with interpolated vectors (10 vectors) in order to see the shape of the calculated velocity profiles more clearly.

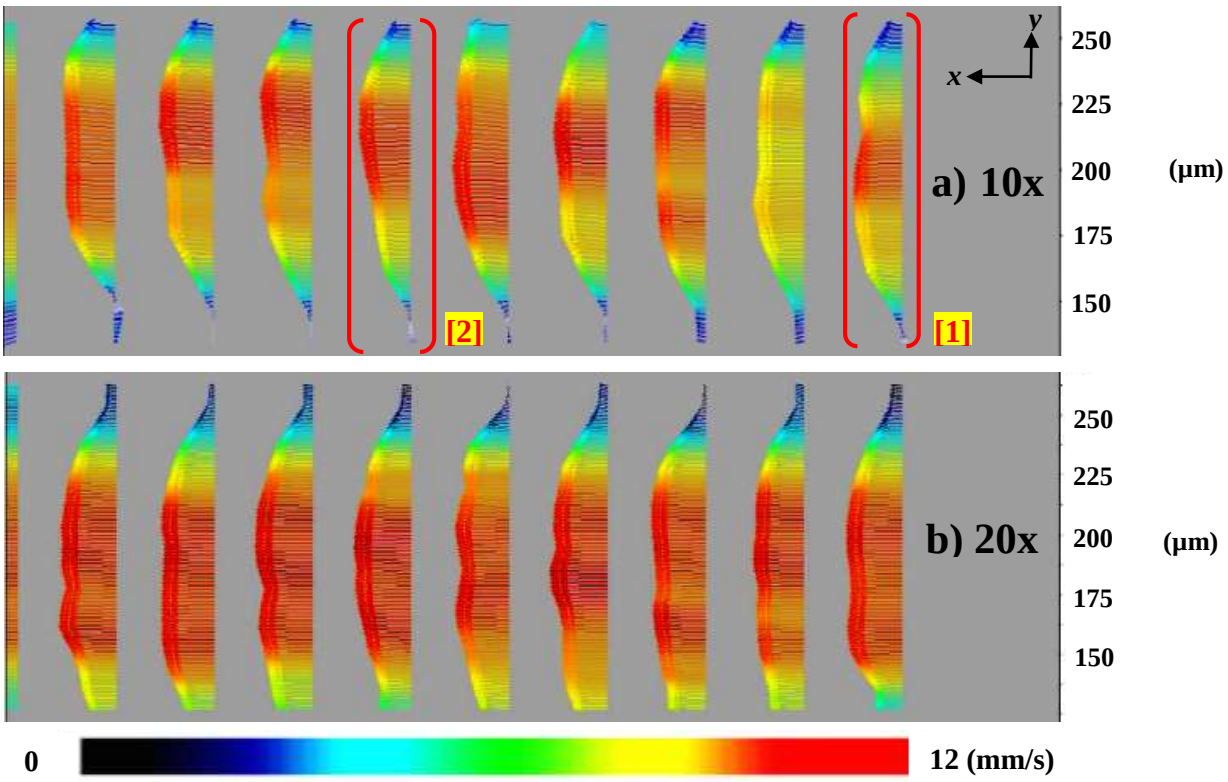

Figure 4.3 Instantaneous velocity profiles for both **a)** 10x and **b)** 20x images.

As can be seen in Figure 4.3, the velocity profiles have a generally parabolic shape as expected. However, the velocity profiles are not smooth along the channel and their shape and peak velocities change erratically. This issue is shown more clearly in Figure 4.4 where two of the velocity profiles in the 10x velocity field in Figure 4.3 are compared to the centre-plane analytical solution.

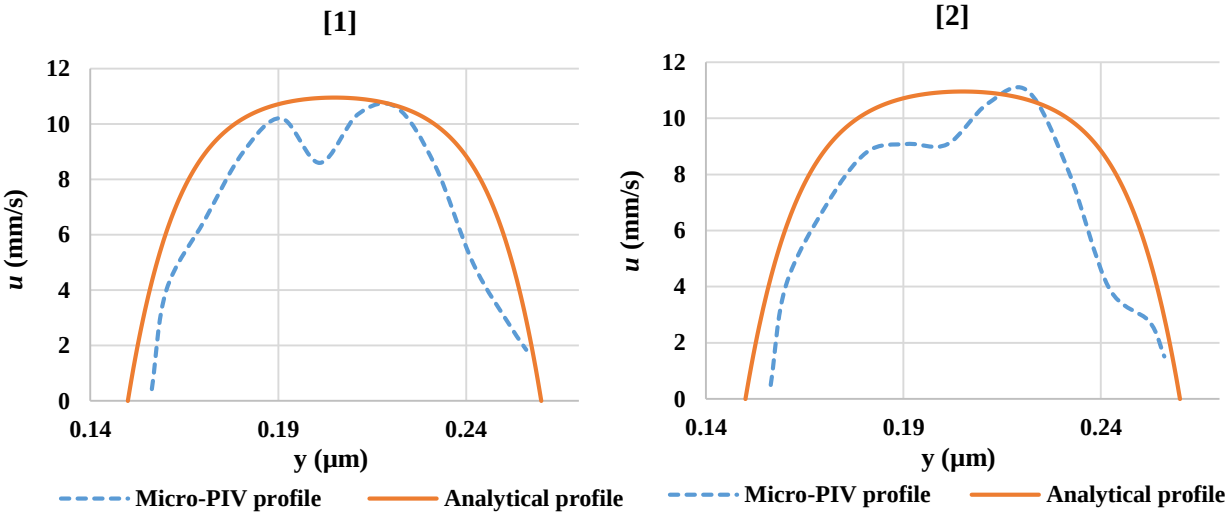

Figure 4.4 Different instantaneous velocity profiles along the channel for 10x images compared to the center-plane analytical solution.

The Reynolds number was calculated to be Re = 0.381, so this is a creeping flow. The data were taken far away from the channel inlet to ensure that the flow domain measured is fully developed. Therefore, the inhomogeneities observed should not be present in the flow. The same issue was observed in the 20x velocity fields. The root mean square (RMS) of deviations of measurements from analytical velocity profile were calculated as 0.594 mm/s and 0.637 mm/s for graphs [1] and graph [2] in Figure 4.4, respectively. It will be shown that the main reason for not obtaining a smooth parabolic velocity profile is related to the large DOC compared to the depth of the channel in the present measurements and seed particles in the images are randomly located in the z direction.

4.3. Averaging schemes

As seen above, the instantaneous velocity profiles appear to vary randomly (see Figure 4.2). This is due to different sources of error, which appear to be random. Some of these errors relate to the particle concentration distribution and size. These random errors can be reduced using averaging schemes.

Spatial averaging is one of the simplest averaging strategies used to process Micro-PIV velocity fields. In this method, all of the velocity profiles in a velocity field are averaged (e.g. along the *x*-direction in Figure 4.3) to create a single velocity profile. This velocity profile shows the average velocity of the flow at one instant of time. This averaging method is only suitable for constant cross-section channels and fully developed flow.

Time-averaging is another averaging scheme used to process Micro-PIV velocity profiles. In this averaging method, multiple velocity fields are averaged over time. In order to perform this averaging, multiple image pairs must be acquired. The result is a single mean velocity field. This averaging method is suitable for flows inside variable geometry microchannels. For this averaging scheme, the flow should be steady. Generating a steady flow is challenging at the micro-scale. This will be addressed in the next section.

4.4. Data collection

As mentioned in Chapter 3, 1000 pairs of images were obtained at a frequency of 3.5 Hz for both the 10x and 20x magnifications. The large number of images were required to track the behavior of the flow over a long time period. The aim of the experiment was to study a steady flow with a fixed flow-rate. Therefore, any fluctuations in the flow are potentially a major source of error. Before analyzing the results, it is advisable to check whether the investigated flow was steady.

To begin, all 1000 image pairs were processed according to the procedure described in Chapter 3. Once velocity fields were obtained for all the images, they were spatially averaged in the *x*-direction to yield a single velocity profile for each image. The averaging is intended to eliminate the random errors in the measured velocity profile. The centre-line velocity of the spatially averaged velocity profiles was plotted versus time in Figure 4.5 for both the 10x and 20x images. This process was done using the PIVMAT toolbox in MATLAB.

As can be seen in Figure 4.5, the flow is not steady but instead shows clear periodicity. The pulses in the flow are associated with the syringe pump used. Oscillations typically occur when the flow rate is very small (on the order of μL/hr) or when the syringe size is not appropriate. In order to mitigate these fluctuations, one should select the volume of the syringe correctly. A small syringe diameter improves the flow rate stability. According to the syringe pump catalog, for the selected flow rate (100 μL/hr*)* the smallest possible syringe is used (50 μL syringe).

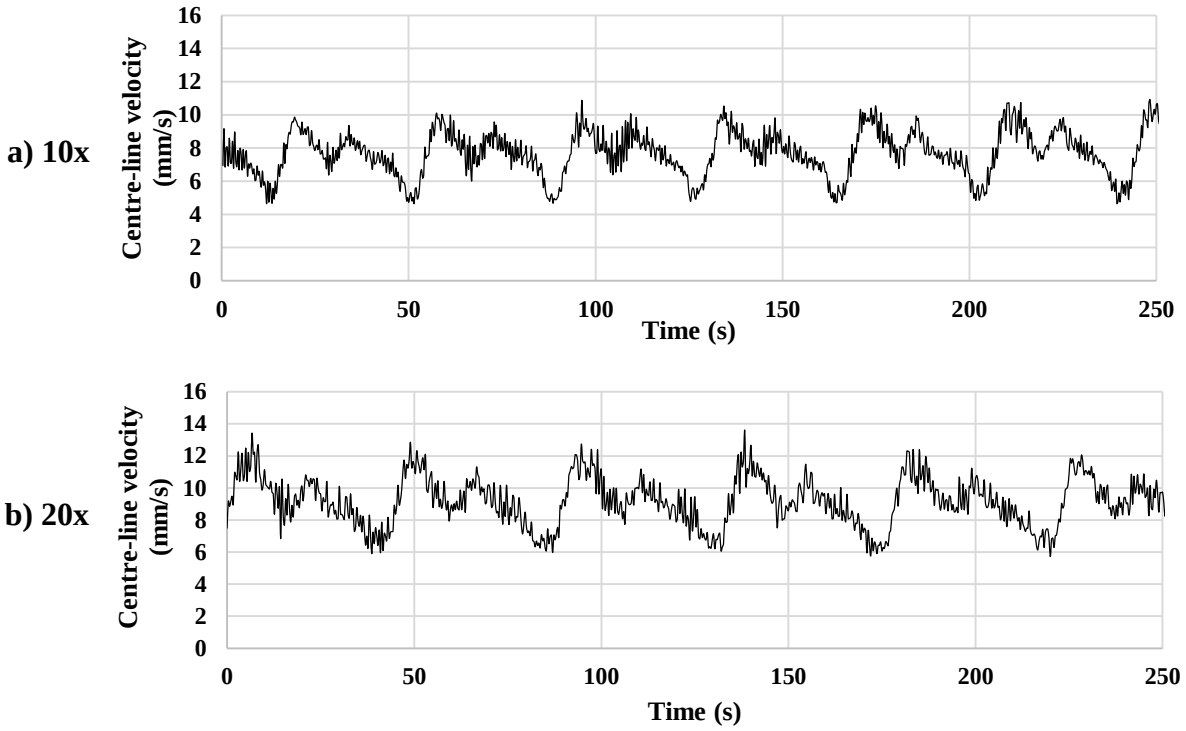

Figure 4.5 The centre-line velocity of the spatially averaged profiles plotted against time for 1000 images for both **a)** 10x and **b)** 20x magnifications.

The fluctuations in Figure 4.5 consist of both small-scale random fluctuations and large-scale periodic fluctuations. The small-scale random fluctuations can be attributed to two factors: 1) the mechanical operation of the pump, and 2) the slip-stick phenomenon in the syringe (Galindo-Rosales, 2017). The syringe pump used in this experiment uses a stepper motor to provide the driving force on the plunger. The stepper motor moves in discrete increments which can cause a fluctuation in the flow. Also the syringe plunger, even if it is pushed with a constant force, does not move smoothly but exhibits jumps due to the friction between the syringe barrel and plunger. This phenomenon is called slip-stick, and it is inevitable in injection using syringe pumps.

The large-scale fluctuation can be attributed to the performance of the syringe pump, since the period is measured to be the time required for the screw of the syringe pump to rotate one turn. Another factor that suggests the large-scale fluctuations are due to the performance of the syringe pump is their repetition with the same period for both 10x and 20x images. Therefore, the investigated flow using the Micro-PIV system is not a steady Poiseuille flow. Since the fluctuations observed in the flow are periodic, the average flow rate is constant in time.

Another unexpected issue observed in Figure 4.5 is the higher average center-line velocity for the flow in the 20x image compared to the 10x image. This was also observed in the instantaneous velocity fields of Figure 4.3. The centre-line average velocity for the 10x and 20x images was calculated to be 7.6 and 9.1 mm/s, respectively, while the flow rate was the same in both case. This is indicative of an error which is not damped out in the averaging process performed so far (spatial averaging). In order to explore this further, all spatially averaged velocity profiles for 1000 images were averaged to give a single velocity profile. Therefore, both spatial averaging and time averaging were performed to yield a single velocity profile for the 10x and 20x images as shown in Figure 4.6.

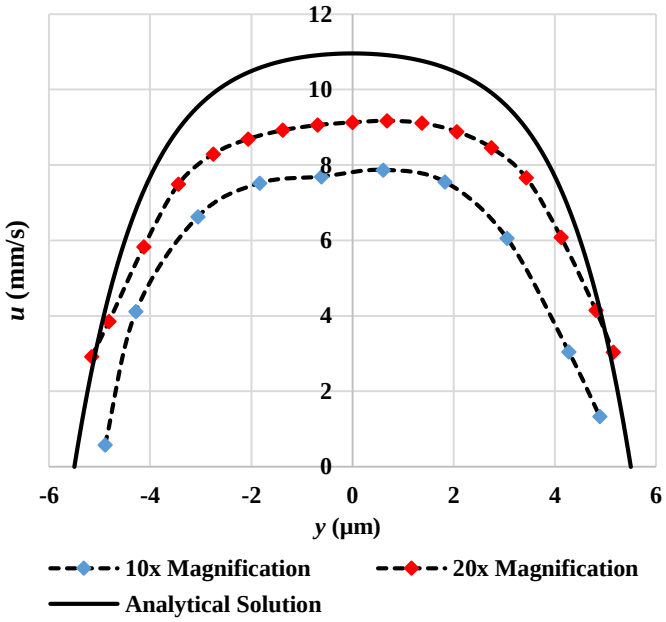

Figure 4.6 Average of all velocity profiles calculated for 1000 images.

In Figure 4.6, all 1000 instantaneous velocity profiles are averaged and compared to the center-plane analytical velocity profile. The random nature of the instantaneous velocity profiles in Figure 4.4 are not present in the averaged velocity profiles in Figure 4.6. This shows that the random errors are damped out by the averaging performed so far. However, the velocity profiles for both the 10x and 20x images does not match the center-plane velocity profiles. The RMS of deviations was calculated as 3.12 mm/s and 1.435 mm/s for the 10x and 20x cases, respectively. Therefore, the 20x velocity profile appears closer to the centre-plane analytical solution than the 10x result. This means that there is a source of error present in the measurements which was not eliminated by the averaging. Also, this error is larger in the 10x images compared to the 20x images.

4.5. Effect of DOC on the Micro-PIV velocity profiles

As shown in Figure 4.6, there is a source of error that depends on the magnification of the objective lens used. Chapter 3 showed that the experimental parameters were chosen to minimize errors due to Brownian motion and particle visibility. However, one source of error that remains in the Micro-PIV results is the DOC. As can be seen in Figure 4.6, the shapes of the measured velocity profiles are similar to the centre-plane analytical profile. However, they have different peak velocities. The experiment was repeated several times and similar peak velocities were obtained each time. Therefore, this source of error is repeatable and not due to an accidental mistake in the experiment.

In Section 4.1, the 3D theoretical velocity profile for the flow was presented. However, only the center-plane velocity profile has been compared to the experiments so far. Instead of comparing the Micro-PIV velocity profiles with the centre-plane analytical solution, it was decided to compare them with the volume average of the 3D analytical velocity profile for different averaging depths. The volume averaging was performed such that 2D velocity profiles were extracted for different planes 0.1 µm apart across the 3D analytical velocity profile and were averaged to yield a 2D volume averaged analytical velocity profile. The effect of the averaging depth on the peak velocity is shown in Figure 4.7, which compares the centre-plane velocity profile, the averaged analytical velocity profile over the entire channel depth (40 µm) and the averaged analytical velocity profile over an arbitrary depth (26 µm).

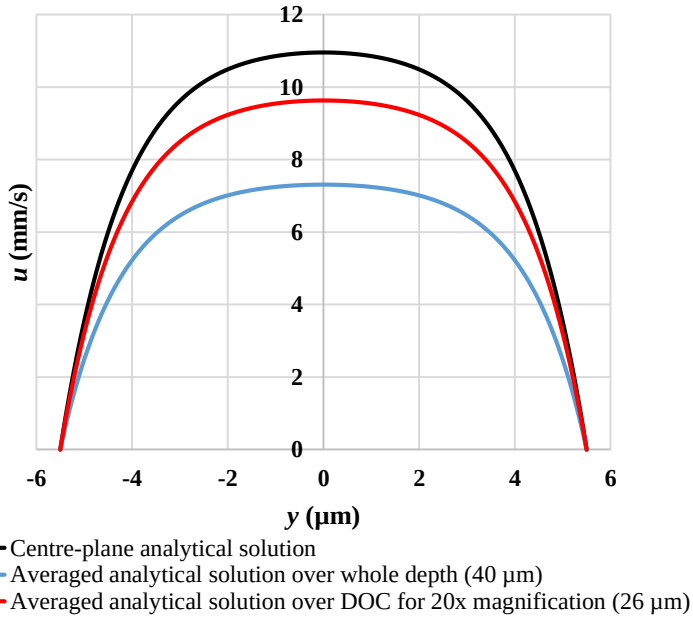

Figure 4.7 The average of the analytical solution for different depths and the centre-plane profile.

There were large discrepancies in the literature (Table 3.3) for the DOC values for similar optics. Therefore, averaging was performed starting from the entire depth of the channel (40 µm) and decreasing the averaging depth (0.2 µm each time, 0.1 µm on each side) to achieve the best match between the experimental data and the analytical solution. The averaged analytic velocity profiles are compared to the Micro-PIV velocity profiles in Figure 4.8. It can be seen that the depth of this volume averaging technique (37 µm for t he 10x magnification and 27.5 µm for the 20x magnification) is correlated to the DOC for both the 10x and 20x measurement.

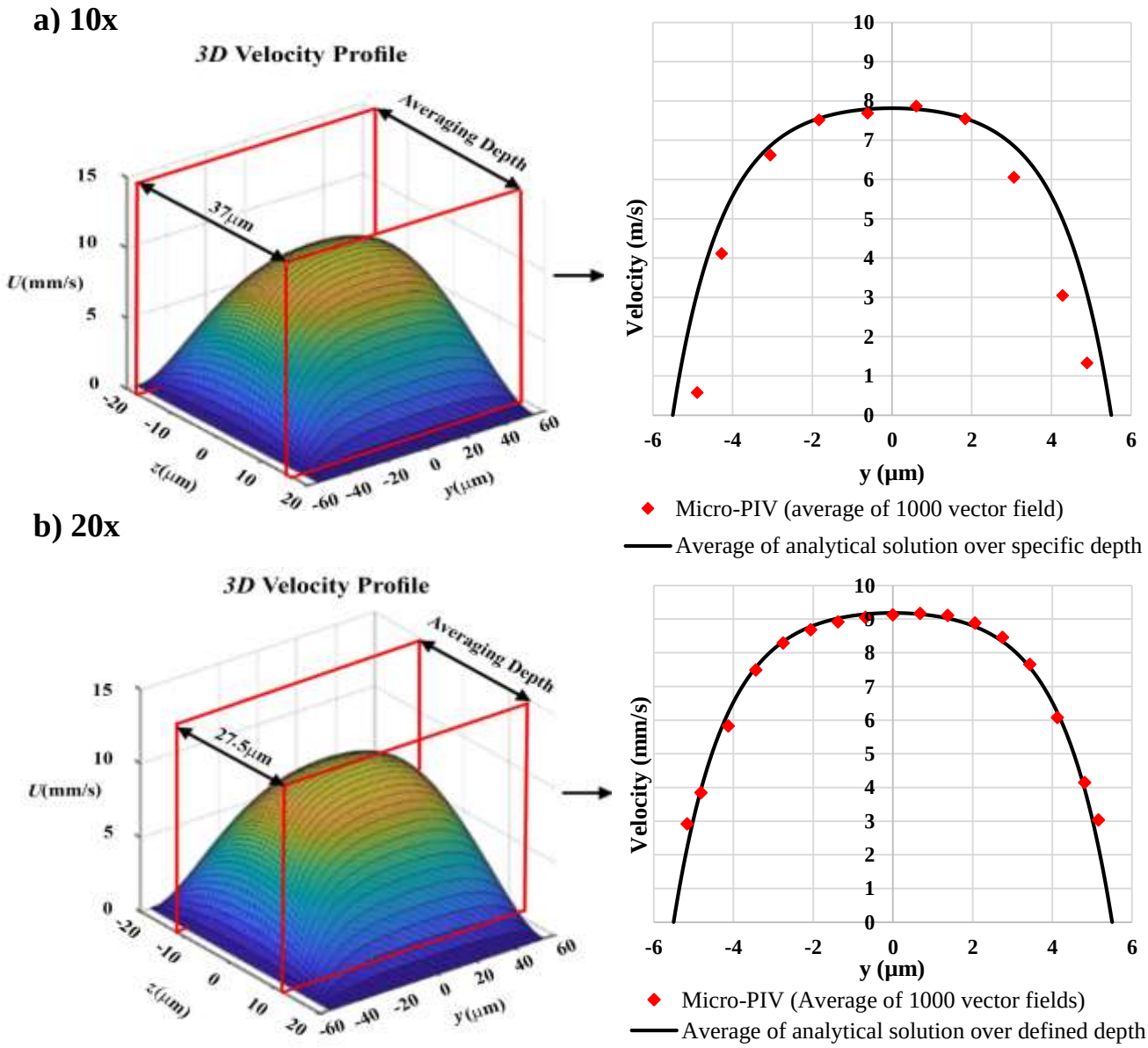

Figure 4. 8 Averaged analytical velocity profile that matches the Micro-PIV velocity profile for: **a)** 10x magnification, and **b)** 20x magnification.

The average of the analytical solution for the values of the DOC reported in Table 3.3 and the experimental result are shown in Figure 4.9 for the 10x magnification. The averaging depth obtained for the 10x magnification (37 µm) is close to the analytical values in Table 3.3, i.e. 36.1 µm (Olsen & Adrian, 2000) and 38.4 µm (Bourdon *et al.*, 2004). Since the *NA* of the objective used (0.3) is different from the available experimental data (*NA* = 0.25) (Wereley & Meinhart , 2005, Bourdon *et al.*, 2004), a range is given. The averaging depth lies within the estimated range of both experimental data sets reported in Table 3.3.

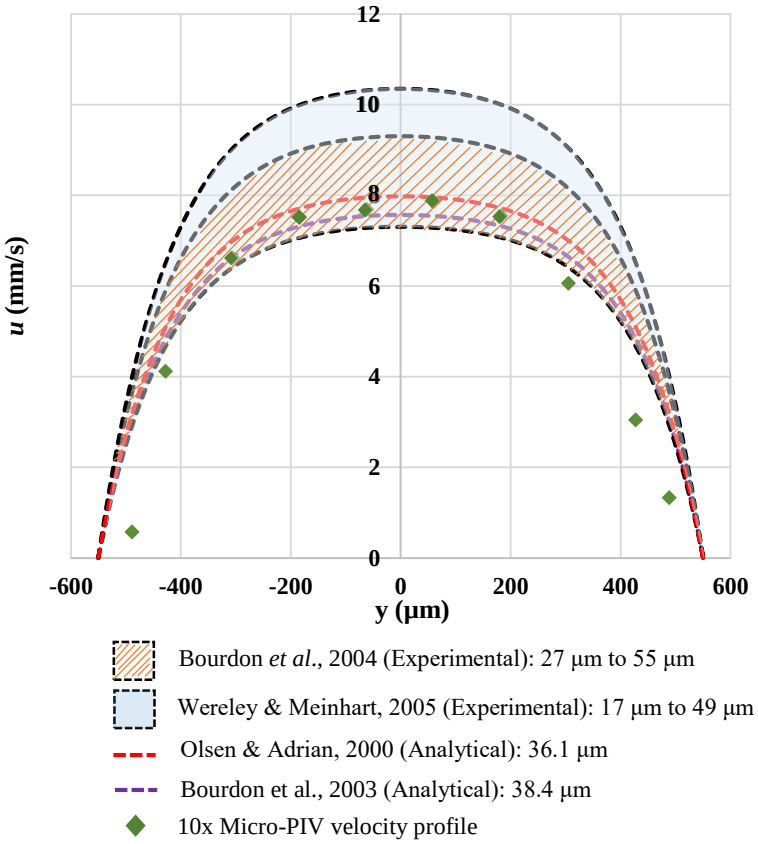

Figure 4.9 The average of the analytical solution for the DOC values mentioned in Table 3.3 and the measured velocity profile for the 10x magnification case. The shaded areas show the range of the DOC based on a specific theory or experiment.

The volume average of the analytical solution for different values of the DOC reported in Table 3.3 and the experimental result are shown in Figure 4.10 for the 20x magnification. The DOC estimated in this experiment (27.5 µm) was significantly larger than the values obtained from the analytical values in Table 3.3, i.e. 16.79 µm according to Olsen & Adrian (2000) and 19.82 µm according to Bourdon *et al.* (2003). The experimental data of Bourdon *et al*. (2004) were close to the present DOC measurements.

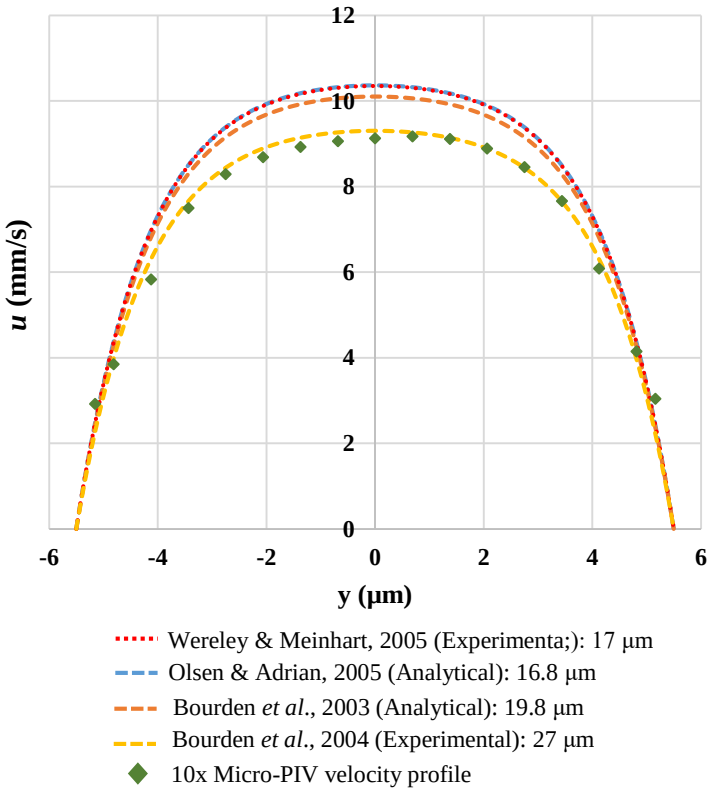

Figure 4.10 The average of the analytical solution for the DOC values mentioned in Table 3.3 and the measured velocity profile for the 20x magnification.

As the DOC values estimated by the volume averaging approach presented in Figure 4.7, are verified by most of the experimental and analytical data from previous studies (Figure 4.9 and Figure 4.10), this volume averaging scheme seems to be a suitable means to predict the DOC.

4.6. Sensitivity to flow fluctuations

As was shown in Figure 4.5, fluctuations were detected in the flow produced by the syringe pump. In this section, in order to check the effect of this issue on the measured velocity profiles, only images within 5% of the mean value were selected for the time averaging. These velocity fields were located in the red band shown in Figure 4.11.

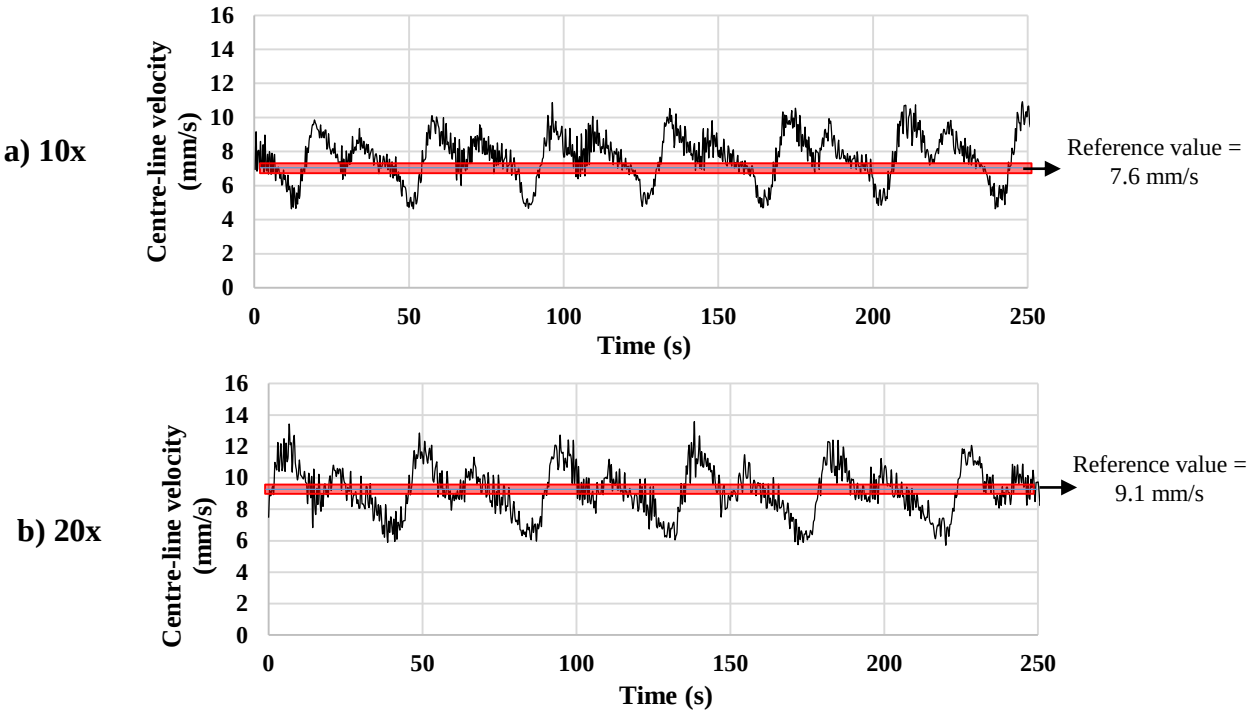

Figure 4.11 The red band shows the range that will be considered for time averaging in **a)** 10x and **b)** 20x magnifications (5% above or below the whole flow average velocity).

The desired velocity fields were selected in Microsoft Excel after being spatially averaged in MATLAB. The results are shown in Figure 4.12.

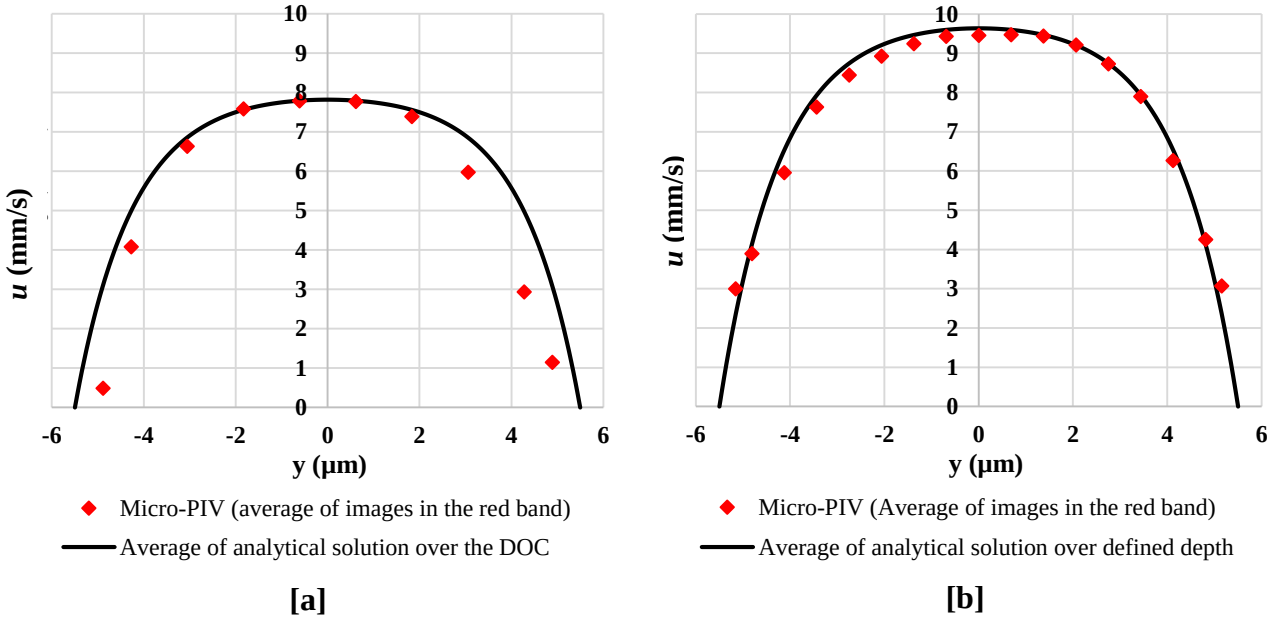

Figure 4.12 Velocity profiles obtained from averaging of images with peak velocity within the red band in the fluctuation graphs for **a)** 10x, and **b)** 20x magnification.

As can be seen in Figure 4.12, no significant improvement is observed between these velocity profiles (RMS of 1.285 mm/s and 0.324 mm/s for the 10x and 20x magnification cases, respectively) and the velocity profiles in Figure 4.8 (RMS of 1.211 mm/s and 0.462 mm/s for the 10x and 20x magnification cases, respectively). This demonstrates that the fluctuations do not affect the measurements. Therefore, the flow can be treated as steady with a flow rate based on the average of the centre-line velocity of all the velocity fields if data are taken in a long enough time which several periods of velocity fluctuations are considered in averaging.

4.7. Near-wall measurements

The velocity profiles shown in Figure 4.12 present the closest agreement with the volume averaged analytical velocity profile in these measurements. Figure 4.12 illustrates that a higher magnification leads to a higher resolution (16 data points in the 20x magnification compared to 10 data points in the 10x magnification). Also, with a higher magnification, the near-wall velocity can be measured with lower error. Figure 4.13 shows this issue more clearly.

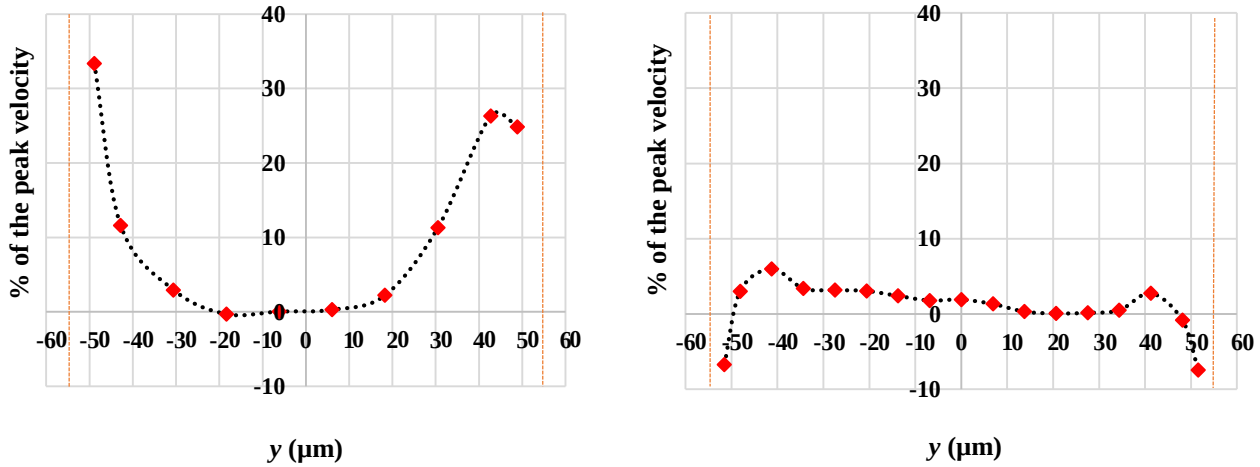

Figure 4. 13 Difference between the analytical solution and the experimental data points at different locations of the channel expressed in percentage of the peak velocity for **a)** 10x, and **b)** 20x magnification.

In Figure 4.13 the difference between the analytical solution and the measurements are presented as a percentage of the peak velocity. The centre-plane of the channel is located at the origin (y = 0) and the channel walls are located at y = +55 µm and y = -55 µm. As seen in Figure 4.13, the error is much larger in the 10x magnification and extends into the central regions. For the 20x magnification the error is less than 10% everywhere in the channel. For the 10x magnification, the error reaches above the 30% of the peak velocity in near-wall regions.

4.8. Sources of near-wall measurement errors

As observed in Figure 4.13, the deviation of the experimental result from the analytical velocity profile was largest in the near-wall regions. In this section, some of the factors that lead this deviation, especially in the near-wall region, are discussed. The first issue relates to the optimum size of the interrogation region used. Although the selected size appears to be optimum (5 to 7 particles are placed in each interrogation region) for both the 10x and the 20x images, they are still large compared to the size of the channel due to the available particles and objective lenses. 32 × 32 pixel interrogation regions correspond to 24.44 × 24.44 μm^2 and 13.75 × 13.75 μm^2 for 10x and 20x magnifications, respectively. Although a geometric mask is placed at the channel wall, the software locates the centre of the first interrogation region exactly at the border of the mask. Therefore, half of the first interrogation region is outside of the channel. The yellow line in Figure 4.14 shows the channel wall and the red square shows one of the interrogation regions at the border of the mask for the 10x magnification. The part of the interrogation region which is outside of the yellow line contains no particles and therefore will bias the cross-correlation calculation. The calculated velocity in this interrogation region only represents the mean velocity in the portion of the interrogation region containing the fluid. The smaller the size of the interrogation region at the wall, the lower the errors generated due to this issue. Higher magnifications and smaller particles are required to implement a smaller interrogation region. Note that a 50% overlap is used in both the horizontal and vertical directions (Figure 4.14). The four small purple squares within the red interrogation region are the quarters of neighboring interrogation regions. This figure only shows the interrogation regions for the first pass before they are shifted for the second pass. The velocity vector calculated for the last interrogation region (red square) corresponds to a point located at the middle of the part of it which contain fluids. This velocity is the nearest point to the wall in the measured velocity profiles and enhances the resolution of the near-wall measurements.

Figure 4. 14 The domain of the channel (inside yellow line) and the first interrogation region at the wall (red square) for 10x magnification.

The other source of near-wall measurement errors results from the chemical structure of the material used for the microchannel. Hydrophilic surfaces tend to attract water molecules while hydrophobic surfaces tend to repel them. This characteristic of solid surfaces are categorized by the contact angle (Galindo-Rosales, 2017). The analytical velocity profile used for the validation assumes a no-slip boundary condition such that the velocities at the wall go to zero. This is correct if the surface of the microchannel is fully hydrophilic (contact angle < 90˚), however, PDMS, which is used in this experiment, is super-hydrophobic (contact angle >150˚). Some chemical processes, such as oxygenated plasma, can be used to convert the surface characteristics temporarily from super-hydrophobic to hydrophilic. For hydrophobic surfaces, the velocity does not go to zero and a slip velocity exists at the wall. No surface treatment was performed for the microchannels used in this experiment. Therefore, the higher velocity measured compared to the analytical velocity profile in the near wall region for the 20x magnification (Figure 4.12 b) can be attributed to this issue.

Another source of error that affects near-wall measurements is the Saftman lift force which is experienced by particles in regions of high velocity gradient, such as the near-wall region, in a channel flow (Behboudi, 2015). It causes particles to move toward the centre of the microchannel leading to a particle concentration deficit near the wall. This source of error can be avoided if a high concentration is used such that, even after particle migration toward the centre of the channel, there are still enough particles in the interrogation region located near the wall. Due to the high concentration of particles used, no noticeable deficiency in particle concentration was detected in this work.

In conclusion, for the measured velocity profiles in Figure 4.12, the discrepancy between the zero velocity at the wall and first velocity measured from the wall (Figure 4.13) can be attributed to the combination of two factors. First, using insufficient magnification to resolve the near-wall velocity profile which leads to errors due to the large size of the interrogation region. The second source of error relates to the fact that the internal surface of the microchannel is not perfectly hydrophilic, and a slip velocity may exist at some parts of the channel's wall. By using higher magnification and smaller particles the first source of error can be reduced. A higher resolution, may allow slip velocities at the channel's wall to be measured.

4.9. Summary

The analytical solution of the Navier-Stoks equation of the desired flow using the Fourier series expansion was available from a previous study (Tabeling 2005). The infinite series from the analytical solution was coded in the Matlab software and the 3D velocity profile (Figure 4.2) was calculated. The output of the Micro-PIV measurements of the flow through rectangular cross-section microchannel resulted in 1000 pairs of images. The obtained images were processed in the Davis software and resulted in 1000 instantaneous velocity fields. Each velocity field consists of 40 to 80 instantaneous velocity profiles depending on the size of the interrogation used for the cross-correlation. These instantaneous velocity profiles were compared to the centre-plane analytical velocity profile and poor agreement was observed (Figure 4.4).

In order to investigate this further, the velocity profiles were spatially averaged. This process was done in the Matlab PIVMAT toolbox (for more information refer to appendix A). By doing this, a spatially-averaged velocity profile was obtained for each velocity field and therefore, 1000 spatially-averaged velocity profiles were available. Although this averaging reduced the deviation of the measured velocity profiles from the centre-plane analytical velocity profiles, there was still considerable variation in the peak velocity. Therefore, the peak velocity of all 1000 spatial averaged velocity profiles were plotted versus time and a periodic variation in the peak velocities was detected (Figure 4.5). The period of these variations were the same in both the 10x and 20x magnifications. Therefore, the variations were most likely caused by the syringe pump. Also, the average of the 1000 centre-line velocities was higher in the 20x magnification (9.1 mm/s) compared to the 10x magnification (7.6 mm/s). In order to explore this more thoroughly, all 1000 spatially-averaged velocity profiles were averaged over time. The random variations in the instantaneous velocity profiles were not present in the time-averaged velocity profiles but a deficit in the centre-line velocity was present which was dependent on the magnification of the objective lens used (Figure 4.6).

By volume averaging the analytical velocity profile, an averaging depth was determined which matched the velocity measured in Figure 4.6. This averaging depth (Figure 4.7) was within the range of the estimated DOC for these experiments based on previous analytical and experimental research. This was graphically shown in Figure 4.9 and Figure 4.10. Therefore, the deficit seen in the centre-line velocity in Figure 4.6 was due to the large DOC compared to the

depth of the channel in these measurements. This can also justifies the random variations observed in the instantaneous velocity profiles as the seed particles are distributed randomly within the micro-channel and their location in the *z* direction is not distinguishable in the particle images.

In order to test the effect of the flow variation generated by the syringe pump (Figure 4.5), spatially averaged velocity profiles with peak velocity within $5^{\%}$ of the average peak velocity of all spatial averaged velocity profile were selected for time averaging and no particular enhancement in the final measured velocity profiles was observed. Therefore, the generated flow can be assumed steady on average, if long enough time to include several periods of velocity fluctuations is considered for time averaging.

Finally, factors which lead to the deviation of the averaged Micro-PIV velocity profiles from the volume averaged analytical velocity profiles (Figure 4.12), especially in the near wall-region, were discussed. Noticeable enhancement was observed in near-wall resolution in the 20x magnification compared to the 10x magnification velocity profiles (Figure 4.13). The large size of the interrogation used for the cross-correlation calculation imposed by the low magnification of the objective lens and the possibility of slip at the wall were introduced as possible sources of errors.

CHAPTER 5: CONCLUSIONS AND FUTURE WORK

The main objective of this research was to commission a newly acquired Micro-PIV system from LA Vision (Germany GmbH) in the Department of Mechanical Engineering at the University of Saskatchewan. To accomplish this, an experiment was designed to test the system by measuring the velocity profile in a microchannel. In the course of the commissioning process, some interesting findings about the effect of the Depth of Correlation on the measured velocity profiles were obtained.

5.1. Summary of experiment

In the design of the experiment, a rectangular cross-section microchannel was selected for the flow device. A NE-300 Just Infusion^{TM} syringe pump and 23 gauge Tygon tubing were used to create the flow loop. The parametric design of the experiment was such that the flow rate (100 µL/hr), size of the seed particles (3µm), concentration of the seed particles (1% volume fraction), and size of the microchannel (40 µm × 110µm) were kept constant, while the magnification of the objective lens (10x and 20x) was varied. The parametric design aimed to minimize common errors in Micro-PIV measurements, such as Brownian motion and poor particle visibility. This configuration enabled a clear assessment of the effect of the DOC on the final result and highlighted its dependence on the magnification of the objective lens used. The image data obtained from the experiment (1000 pairs of images) were processed by the DAVIS 8.2 software. A 32×32 pixel square interrogation region and two-pass cross-correlation with 50% overlap were selected as the most suitable processing parameters. Post processing of the data, such as spatial and time averaging of the calculated velocity fields, was performed using the PIVMAT toolbox in Matlab.

5.2. Experimental results and conclusions

1000 image pairs of a flow in a rectangular cross-section microchannel seeded with fluorescent particles were acquired at a frequency of 3.5 Hz using the La Vision Micro-PIV system. The images were then processed using the Davis 8.2 software to calculate the velocity fields. The high frequency of image acquisition (3 Hz) and the short gap between each exposure (10 µs) enabled a time resolved velocity measurements such that small velocity changes in time were tracked in measurements (Figure 4.5). The spatial resolution of the velocity profile measurements was controlled by the magnification of the objective lens used for image acquisition. Velocity profiles

of the same flow were measured using both the 10x and the 20x objectives. The 3D analytical velocity profile was calculated by solving the Navier-Stokes equation for the nominal boundary conditions of the flow. This velocity profile was subsequently used to assess the measured velocity profiles. For a higher magnification the spatial resolution of the measured velocity profiles improved in both the *z*-direction (depth of the channel) and *y*-direction (span-wise extent). The enhancement in the *z* and *y*-direction resolution were found to be related to the DOC issue and the allowable size of the interrogation region, respectively.

This study showed that the DOC has a significant impact on low-magnification Micro-PIV measurements. A large DOC causes random variations in the measured instantaneous velocities. However, this is not due to actual velocity fluctuations but, rather the random positioning of particles in the *z* direction. The reason for this was the large size of the DOC compared to the depth of the microchannel. Depending on a particle's distance from the center of the channel, it will move with a lower velocity compared to the centre-plane particles. The location in the *z* direction is not measurable from the images. Their contribution to the overall measurement results in the random variation observed in the velocity profiles.

Time-averaged velocity profiles (the average of all of the spatially-averaged velocity profiles) removed the apparently random velocity variations, and their cumulative effect appeared as reduction in the magnitude of the velocity profile. This velocity reduction was related to the DOC by applying volume averaging to the 3D analytical velocity profile. The depth of the volume average (37 μm and 27.5 μm for the 10x and the 20x magnifications, respectively) was selected to obtain good agreement with the measured velocity profile. The calculated depth from the volume averaging was consistent with the DOC reported in previous analytical and experimental studies for both the 10x and the 20x magnification cases. Based on this analysis, a major conclusion of the study was that a large DOC relative to the size of the microchannel will significantly reduce the spatial resolution of the velocity measurements in the *z*-direction.

Spatially averaged velocity profiles showed that the measured flow was not steady. For example, the peak velocity of the spatially averaged velocity profiles versus time indicated a complex and semi-periodic variation in time, for both the 10x and 20x magnification cases. In order to obtain more insight about the measured velocity profiles, time-averaging was also performed on the measured velocity profiles. This experimental study concluded that the periodic

fluctuations created by the syringe pump, which is a common component in Micro-PIV flow configurations, can be eliminated by time-averaging the velocity profiles. This was demonstrated by comparing the results of averaging a subset of the spatially-averaged profiles based on the peak velocity value and the entire set.

The final conclusion of this experimental study is related to measurements in the transverse (*y*-direction) or more specifically the near-wall resolution of the measurements. The near-wall resolution was enhanced in the 20x magnification compared to the 10x magnification measured velocity profiles. The enhancement was quantified by calculating the deviation from the volume-averaged analytical velocity profile. The minimum allowable size of the interrogation region used for the cross-correlation calculations was imposed by the magnification used and contributed to the deviation of the measured profile near the wall. The presence of a slip velocity at the wall could also account for some of the observed deviation specifically in near wall region. One of the major characteristics of slip at the wall is the higher velocity in the near-wall region compared to the no slip condition. This was clearly observed in the 20x velocity profiles. The reason for this issue was related to the hydrophobic nature of the PDMS used to make the microchannel, in this experiment.

Overall, the La Vision Micro-PIV system was successfully commissioned in this experimental research project. A novel volume-averaging technique was introduced to assess the effect of the DOC on the measured velocity profiles. As such, this study achieved the two objectives identified in Chapter 1.

5.3. Future work

Although some explanations were offered in previous sections for the observed deviations of the measured velocity profiles from the analytical velocity profiles in near-wall regions, further investigations are required to explore the reasons behind this issue in more depth. Therefore, Micro-PIV measurements with higher magnifications and smaller particles would be useful to enable implementing smaller interrogation regions for the cross-correlation calculations. Smaller interrogation regions would allow velocity vectors measurement closer to the wall so, the source of the deviations such as the slip velocities at the wall can be examined in more detail.

Although the DOC would be thinner in higher magnification Micro-PIV measurements, the microchannel should be designed thinner to avoid the visibility issue. Therefore, the DOC issue

may still exist in the higher magnification measurements. The volume averaging of the analytical velocity profile presented in this research can be investigated further to explore its ability to predict the centre-plane velocity profile in more complicated fluid flows where an analytical solution is not available for the verification. It is of highly interest to find out whether the reduction in the measured velocity magnitude due to the DOC would be the same in the non-Newtonian fluid flows such as the blood flow or the flow of a Newtonian fluid through a more complicated microchannel shapes.

REFERENCES

Adrian R. J. "Particle-imaging techniques for experimental fluid mechanics." *Annual Review of Fluid Mechanics* 23, no. 1 (1991): 261-304.

Adrian L., Ronald J. Adrian, and Jerry Westerweel. "Particle image velocimetry." *Cambridge University Press*, 2011.

Al-Muhammad J., Séverine Tomas, Nassim Ait-Mouheb, Muriel Amielh, and Fabien Anselmet. "Micro-PIV characterization of the flow in a milli-labyrinth-channel used in drip irrigation." *Experiments in Fluids* 59, no. 12 (2018): 181.

Angele K. P., Y. Suzuki, J. Miwa, and N. Kasagi. "Development of a high-speed scanning Micro PIV system using a rotating disc." *Measurement Science and Technology* 17, no. 7 (2006): 1639.

Aristotle G., Dimitris S. Mathioulakis, and Sokrates Tsangaris. "Microscope PIV for velocity-field measurement of particle suspensions flowing inside glass capillaries." *Measurement Science and Technology* 10, no. 11 (1999): 1037.

Barnkob R., Christian J. Kähler, and Massimiliano Rossi. "General defocusing particle tracking." *Lab on a Chip* 15, no. 17 (2015): 3556-3560.

Bastiaans R. JM. "Cross-correlation PIV; theory, implementation and accuracy.", *Eindhoven University of Technology*, Faculty of Mechanical Engineering, Thesis, 2000.

Behboodi F. "Investigation of determining velocity profiles in microfluidic channel using Micro-PIV.", *University of Alberta*, Faculty of Mechanical Engineering, Thesis, 2015.

Bourdon C. J., Michael G. Olsen, and Allen D. Gorby. "Validation of analytical solution for depth-of-correlation in microscopic particle image velocimetry." *ASME International Mechanical Engineering Congress and Exposition*, vol. 37211, pp. 559-570. 2003.

Bourdon C. J., Michael G. Olsen, and Allen D. Gorby. "The depth of correlation in Micro-PIV for high numerical aperture objectives". no. SAND2004-4379C. *Sandia National Laboratories*, 2004.

Brücker C. "3D scanning-particle-image-velocimetry: technique and application to a spherical cap wake flow." *Applied Scientific Research* 56, no. 2-3 (1996): 157-179.

Bruus H., Jurg Dual, Jeremy Hawkes, Martyn Hill, Thomas Laurell, Johan Nilsson, Stefan Radel, Satwindar Sadhal, and Martin Wiklund. "Forthcoming Lab-on-a-Chip tutorial series on acoustofluidics: Acoustofluidics—exploiting ultrasonic standing wave forces and acoustic streaming in microfluidic systems for cell and particle manipulation." *Lab on a Chip* 11, no. 21 (2011): 3579-3580.

Chuang H. S., Lichuan Gui, and Steven T. Wereley. "Nano-resolution flow measurement based on single pixel evaluation PIV." *Microfluidics and Nanofluidics* 13, no. 1 (2012): 49-64.

Cierpk C., and C. J. Kähler. "Particle imaging techniques for volumetric three-component (3D3C) velocity measurements in microfluidics." *Journal of Visualization* 15, no. 1 (2012): 1-31.

Dahm W. J., Lester K. Su, and Kenneth B. Southerland. "A scalar imaging velocimetry technique for fully resolved four-dimensional vector velocity field measurements in turbulent flows." *Physics of Fluids A: Fluid Dynamics* 4, no. 10 (1992): 2191-2206.

Dongqing L., ed."Encyclopedia of microfluidics and nanofluidics." *Springer Science & Business Media*, 2008.

Elsinga G. E., Fulvio Scarano, Bernhard Wieneke, and Bas W. van Oudheusden. "Tomographic particle image velocimetry." *Experiments in Fuids* 41, no. 6 (2006): 933-947.

Galindo-Rosales F. J. "Complex fluids and rheometry in microfluidics." *Complex Fluid-Flows in Microfluidics*, pp. 1-23. Springer, Cham, 2018.

Gothsch T., Christiane Schilcher, Claudia Richter, Stefan Beinert, Andreas Dietzel, Stephanus Büttgenbach, and Arno Kwade. "High-pressure microfluidic systems (HPMS): flow and cavitation measurements in supported silicon microsystems." *Microfluidics and Nanofluidics* 18, no. 1 (2015): 121-130.

Guerrero-Viramontes J. A., D. Moreno-Hernández, F. Mendoza-Santoyo, and M. Funes-Gallanzi. "3D particle positioning from CCD images using the generalized Lorenz–Mie and Huygens–Fresnel theories." *Measurement Science and Technology* 17, no. 8 (2006): 2328.

Inoué S. "Foundations of confocal scanned imaging in light microscopy."*Handbook of Biological Confocal Microscopy*, pp. 1-19. Springer, Boston, MA, 2006.

Jahanmiri M. "Particle image velocimetry: Fundamentals and its applications." *Chalmers University of Technology*, Department of Mechanical Engineering, Thesis, 2011.

Kao H. P., and A. S. Verkman. "Tracking of single fluorescent particles in three dimensions: use of cylindrical optics to encode particle position." *Biophysical Journal* 67, no. 3 (1994): 1291-1300.

Keane R. D., R.J. Adrian, and Yuanhui Zhang. "Super-resolution particle imaging velocimetry." *Measurement Science and Technology* 6, no. 6 (1995): 754.

Kelemen K., F. E. Crowther, C. Cierpka, L. L. Hecht, C. J. Kähler, and H. P. Schuchmann. "Investigations on the characterization of laminar and transitional flow conditions after high pressure homogenization orifices." *Microfluidics and Nanofluidics* 18, no. 4 (2015): 599-612.

Kim H., Sebastian Große, Gerrit E. Elsinga, and Jerry Westerweel. "Full 3D-3C velocity measurement inside a liquid immersion droplet." *Experiments in Fluids* 51, no. 2 (2011): 395-405.

Koutsiaris A. G., D. S. Mathioulakis and S. Tsangaris. "Microscope PIV for velocity-field measurement of particle suspensions flowing inside glass capillaries." *Measurement Science and Technology* 10, no. 11 (1999): 1037.

Laurell T., Filip Petersson, and Andreas Nilsson. "Chip integrated strategies for acoustic separation and manipulation of cells and particles." *Chemical Society Reviews* 36, no. 3 (2007): 492-506.

Lei P., “CROSS CORRELATION.” *A-to-Z Guide to Thermodynamics, Heat and Mass Transfer, and Fluids Engineering* c., 2006.

Lindken R., Massimiliano Rossi, Sebastian Große, and Jerry Westerweel. "Micro-particle image velocimetry (μPIV): recent developments, applications, and guidelines." *Lab on a Chip* 9, no. 17 (2009): 2551-2567.

Lindken R., J. Westerweel, and B. Wieneke. "Stereoscopic micro PIV applied to the three-dimensional flow in a T-mixer." *Proceedings of the PIVNET2 International Workshop on lPIV and Applications in Microsystems, Delft*. 2005.

Lu J., Francisco Pereira, Scott E. Fraser, and Morteza Gharib. "Three-dimensional real-time imaging of cardiac cell motions in living embryos." *Journal of Biomedical Optics* 13, no. 1 (2008): 014006.

Meinhart C. D., Steve T. Wereley, and Juan G. Santiago. "PIV measurements of a microchannel flow." *Experiments in Fluids* 27, no. 5 (2000): 414-419.

Meinhart C. D., and Hongsheng Zhang. "The flow structure inside a microfabricated inkjet printhead." *Journal of Microelectromechanical Systems* 9, no. 1 (2000): 67-75.

Minsky M. "Memoir on inventing the confocal scanning microscope." *Scanning* 10, no. 4 (1988): 128-138.

Moreno-Hernandez D., J. Andrés Bueno-García, J. Ascención Guerrero-Viramontes, and Fernando Mendoza-Santoyo. "3D particle positioning by using the Fraunhofer criterion." *Optics and Lasers in Engineering* 49, no. 6 (2011): 729-735.

Muller P. B., Massimiliano Rossi, A. G. Marin, Rune Barnkob, Per Augustsson, Thomas Laurell, Christian J. Kaehler, and Henrik Bruus. "Ultrasound-induced acoustophoretic motion of microparticles in three dimensions." *Physical Review E* 88, no. 2 (2013): 023006.

Nguyen N. T., Steven T. Wereley, and Seyed Ali Mousavi Shaegh. "Fundamentals and Applications of Microfluidics." *Artech house*, 2019.

Olsen M. G., and R. J. Adrian. "Out-of-focus effects on particle image visibility and correlation in microscopic particle image velocimetry." *Experiments in Fluids* 29, no. 1 (2000): S166-S174.

Ovryn B., and Edward A. Hovenac. "Coherent forward scattering particle-image velocimetry: application of Poisson's spot for velocity measurements in fluids." *Optical Diagnostics in Fluid and Thermal Flow*, vol. 2005, pp. 338-348. International Society for Optics and Photonics, 1993.

Park J. S., Chang Kyoung Choi, and Kenneth D. Kihm. "Optically sliced micro-PIV using confocal laser scanning microscopy (CLSM)." *Experiments in Fluids* 37, no. 1 (2004): 105-119.

Pitts K. L., and Marianne Fenech. "Micro-particle image velocimetry for velocity profile measurements of micro blood flows." *JoVE (Journal of Visualized Experiments)* 74 (2013): e50314.

Prasad A. K., R. J. Adrian, C. C. Landreth, and P. W. Offutt. "Effect of resolution on the speed and accuracy of particle image velocimetry interrogation." *Experiments in Fluids* 13, no. 2-3 (1992): 105-116.

Raffel M., Christian E. Willert, Fulvio Scarano, Christian J. Kähler, Steve T. Wereley, and Jürgen Kompenhans. "Particle image velocimetry: a practical guide." *Springer*, 2018.

Rossi M., Ralph Lindken, Beerend P. Hierck, and Jerry Westerweel. "Tapered microfluidic chip for the study of biochemical and mechanical response at subcellular level of endothelial cells to shear flow." *Lab on a Chip* 9, no. 10 (2009): 1403-1411.

Sadr R., K. Anoop, and R. Khader. "Effects of surface forces and non-uniform out-of-plane illumination on the accuracy of nPIV velocimetry." *Measurement Science and Technology* 23, no. 5 (2012): 055303.

Santiago J. G., Steve T. Wereley, Carl D. Meinhart, D. J. Beebe, and Ronald J. Adrian. "A particle image velocimetry system for microfluidics." *Experiments in Fluids* 25, no. 4 (1998): 316-319.

Shinohara K., Yasuhiko Sugii, Jae Hong Jeong, and Koji Okamoto. "Development of a three-dimensional scanning microparticle image velocimetry system using a piezo actuator." *Review of Scientific Instruments* 76, no. 10 (2005): 106109.

Sinton D. "Microscale flow visualization." *Microfluidics and Nanofluidics* 1, no. 1 (2004): 2-21.

Song Y., Daojian Cheng, and Liang Zhao, eds. "Microfluidics: Fundamentals, Devices, and Applications." *John Wiley & Sons*, 2018.

Stolz W., and J. Köhler. "In-plane determination of 3D-velocity vectors using particle tracking anemometry (PTA)." *Experiments in Fluids* 17, no. 1-2 (1994): 105-109.

Tabeling P. "Introduction to microfluidics." *OUP Oxford*, 2005.

Török P. C., J. R. Sheppard, and P. Varga. "Study of evanescent waves for transmission near-field optical microscopy." *Journal of Modern Optics* 43, no. 6 (1996): 1167-1183.

Urushihara T., C. D. Meinhart, and R. J. Adrian. "Investigation of the logarithmic layer in pipe flow using particle image velocimetry." *Near-wall Turbulent Flows* (1993): 433-446.

Wereley S. T., and Carl D. Meinhart. "Micron-resolution particle image velocimetry." *Microscale Diagnostic Techniques*, pp. 51-112. Springer, Berlin, Heidelberg, 2005.

Wereley S. T., and Carl D. Meinhart. "Recent advances in micro-particle image velocimetry." *Annual Review of Fluid Mechanics* 42 (2010): 557-576.

Yoon S. Y., and Kyung Chun Kim. "3D particle position and 3D velocity field measurement in a microvolume via the defocusing concept." *Measurement Science and Technology* 17, no. 11 (2006): 2897.

Zettner C., and M. Yoda. "Particle velocity field measurements in a near-wall flow using evanescent wave illumination." *Experiments in Fluids* 34, no. 1 (2003): 115-121.

APPENDIX A: ANALYTICAL SOLUTION AND DEPTH AVERAGING CODES

In this Appendix, the code developed for the analytical solution of the flow and its averaging over the depth of the channel is presented. The way the analytical solution is coded is that the area of the channel is divided into small squares and the infinite series of equation (4.2) is calculated at the edges of the squares for the first 500 terms (n = 500). The value of the series did not change significantly after n = 150.

```
clc
clear
% Q=10 (microliter/hour) , W = 110 (micrometer), b= 40 (micrometer)
Q=2.548*(10^(-11));        %Cubic meter/s
u=8.9*10^(-4);             %viscosity of dionized water (pa.s)
W=110*(10^(-6));           %m
b=40*(10^(-6));            %m
n=1;
L=0;
bnm=linspace(0.15,0.26,111)
for n=1:500
Bn=(2*n-1)*(pi/W);
l(n)=(1/Bn^4)*(1-(2/(Bn*b))*tanh(Bn*(b/2)));
L=L+l(n);
end
G=((Q*u*W)/(8*b*L))      %pressure gradient along the channel (pa/m)
Y=-W/2:(10^(-7)):W/2;
Z=-b/2:(10^(-7)):b/2;
n=1;
C=0;
for j=1:1:(b/(10^(-7)))+1
for i=1:1:(W/(10^(-7)))+1
H=0;
for n=1:500
C=(2*n-1)*(pi/W);
h(n)=(((-1)^(n+1))/(C^3))*(1-(cosh(C*Z(j))/cosh(C*b/2)))*cos(C*Y(i));
H=H+h(n);
end
U(j,i)=(4*G*H)/(u*W);
end
end
figure
h=surf (Y,Z,U)
```

```
34.  shading interp
35.  xlabel('y (m)'), ylabel('Z (m)'), zlabel('U (m/s)'), title('3D velocity profile');
36.  for i=66:1:335
37.  Ud(n,:)=U(i,:);
38.  n=n+1;
39.  end
40.  UUd=sum(Ud)/270;          %average velocity profile
41.  y=-W/2:(10^(-6)):W/2;
42.  figure
43.  plot(Y,UUd,'linewidth',5)   %ploting averaged velocity profile over mentioned depth
44.  ylabel('x component velocity (m/s)'), xlabel('width of the channel (m)'), legend('analytical'),
       title ('Center-plane 2D profile');
45.  set(gca,'linewidth',2,'FontSize',30)
```

APPENDIX B: POST-PROCESSING CODES

In this Apendix, the code developed in the PIVMAT toolbox of Matlab for post-processing the Micro-PIV data is covered. Post processing includes spatial averaging of instantaneous velocity fields, normalizing of the velocity profiles based on the center-plane velocity in each velocity field, and calculating the spatial average of normalized velocity fields. There is no pre-defined function in the toolbox for time-averaging. Therefore, in order to obtain a velocity profile that represents the average of 1000 velocity fields, the 1000 spatially averaged velocity profiles were averaged manually in the code. Finally, the average of the normalized spatially averaged velocity profiles were calculated. The below code is used for the 20x magnification data and some numbers (especially, the ranges of the counters of the loops in the code) are different for the 10x magnification data.

```
clc
clear
v = loadvec('*.VC7');          % loads all the vector field files obtained from the Davis software
r = loadvec('*.VC7');
figure(1);
showf(v);                      % displays instantaneous velocity profile
hold on
FF=spaverf (v,'x');            % calculates spatial average velocity profile
figure (2);
showf (FF);                    % display spatial averaged velocity profile
i=1;
hold on
vv = struct;                   % make a structure that only contains three fields of vx, vy, vtot
for n=1:1000
    vv(n).vx = v(n).vx(:,:);
    vv(n).vy = v(n).vy(:,:);
    vv(n).tv = sqrt((v(n).vx(:,:)).^2 + (v(n).vy(:,:)).^2);
end
% make a readable file by PIV-MAT module that contains normalized instantaneous velocities
for n=1:1000
    for i=1:43
        for j=1:33
            r(n).vx(i,j) = (vv(n).vx(i,j))/(vv(n).vx(i,21));
        end
```

```
    end
end
figure(3);
showf(r);                          % display normalized instantaneous velocity profile
ss=spaverf(r,'x');
figure(4),
showf(ss);                         % display normalized spatial averaged velocity profile
hold on
% calculating the average of the spatial averaged velocity profiles of 1000 images (avsa)
sa=0;
n=1;
for n=1:1000
    for i=1:33
        sa(n,i)=FF(n).vx(1,i);
    end
end
avsa=0;
n=1;
for i=13:29
    avsa(n)=sum(sa(:,i))/1000;
    n=n+1;
end
% calculating the average of normalized spatial averaged velocity profiles of 1000 images
(navsa)
nsa=0;                             % matrix of normalized spatial averaged velocity profiles
n=1;
for n=1:1000
    for i=1:33
        nsa(n,i)=ss(n).vx(1,i);
    end
end
navsa=0;
n=1;
for i=13:29
    navsa(n)=sum(nsa(:,i))/1000;
    n=n+1;
end
```

Some output graphs of this code are shown in Figure B.1 to Figure B.4 of this Appendix. Figure B.1 shows the instantaneous velocity fields for the 20x magnification. The sequence of 1000 instantaneous velocity fields are played in a video after the code is compiled. Some frames of this video are shown in Figure B.1.

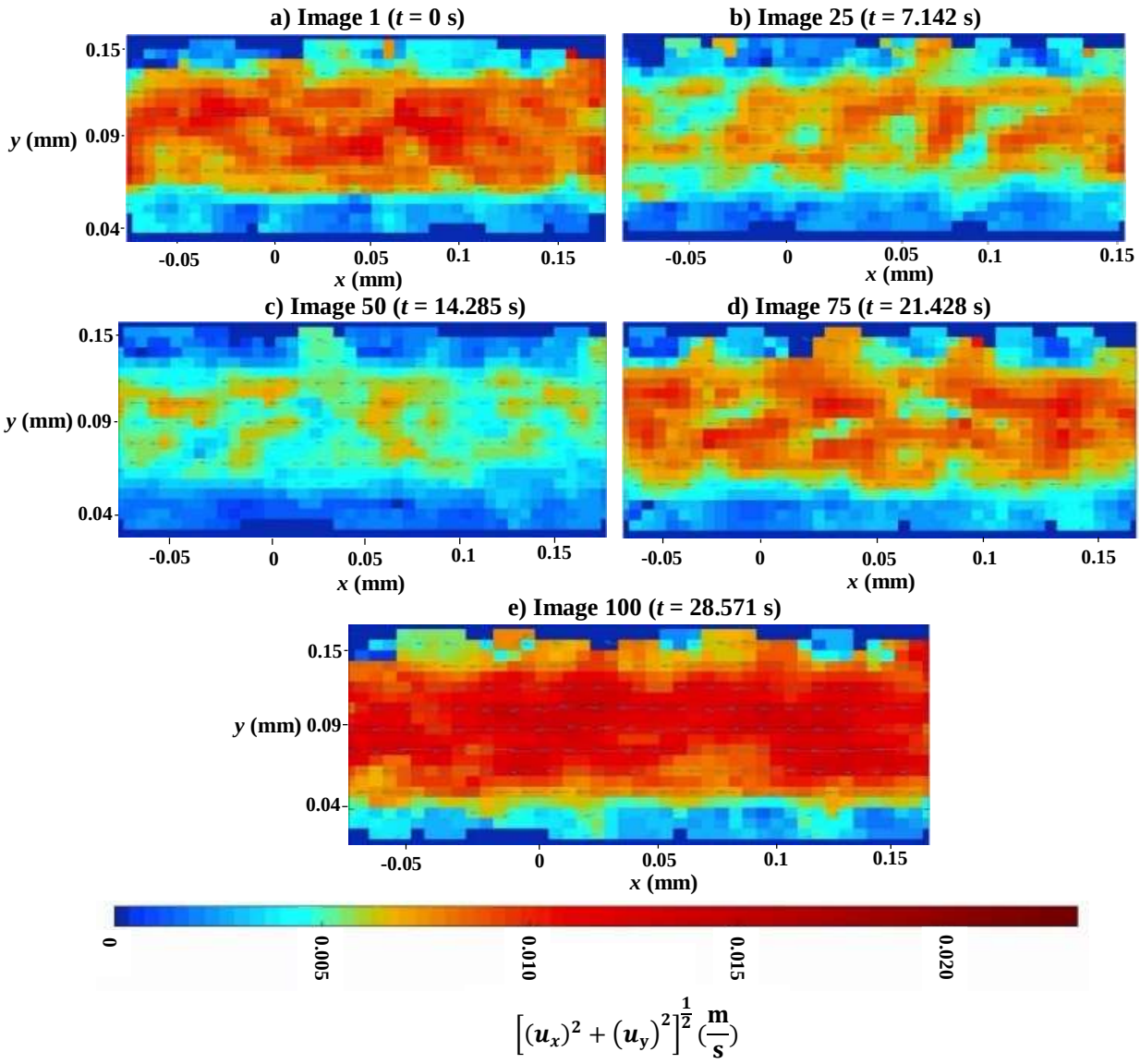

Figure B.1 Instantaneous velocity field at four different times of **a)** t = 0 s, **b)** t = 7.142 s, **c)** t = 14.285 s, **d)** t = 21.428 s and **e)** t = 28.571 s which approximately shows a period of fluctuation in the flow

Five different instantaneous velocity fields (image pairs of 1, 25, 50, 75, and 100) are shown in Figure B.1. As can be seen, velocity profiles are not homogeneous (as shown in Figure 4.3). Also, it appears that the flow is not steady. For example, the flow-rate in image 1 seems to be higher and then decreases in image 25 and image 50 and again increases in image 75 and image 100. This shows, approximately, a cycle of flow variation. Figure B.2 shows the same images with the instantaneous velocity profiles along the channel spatially averaged.

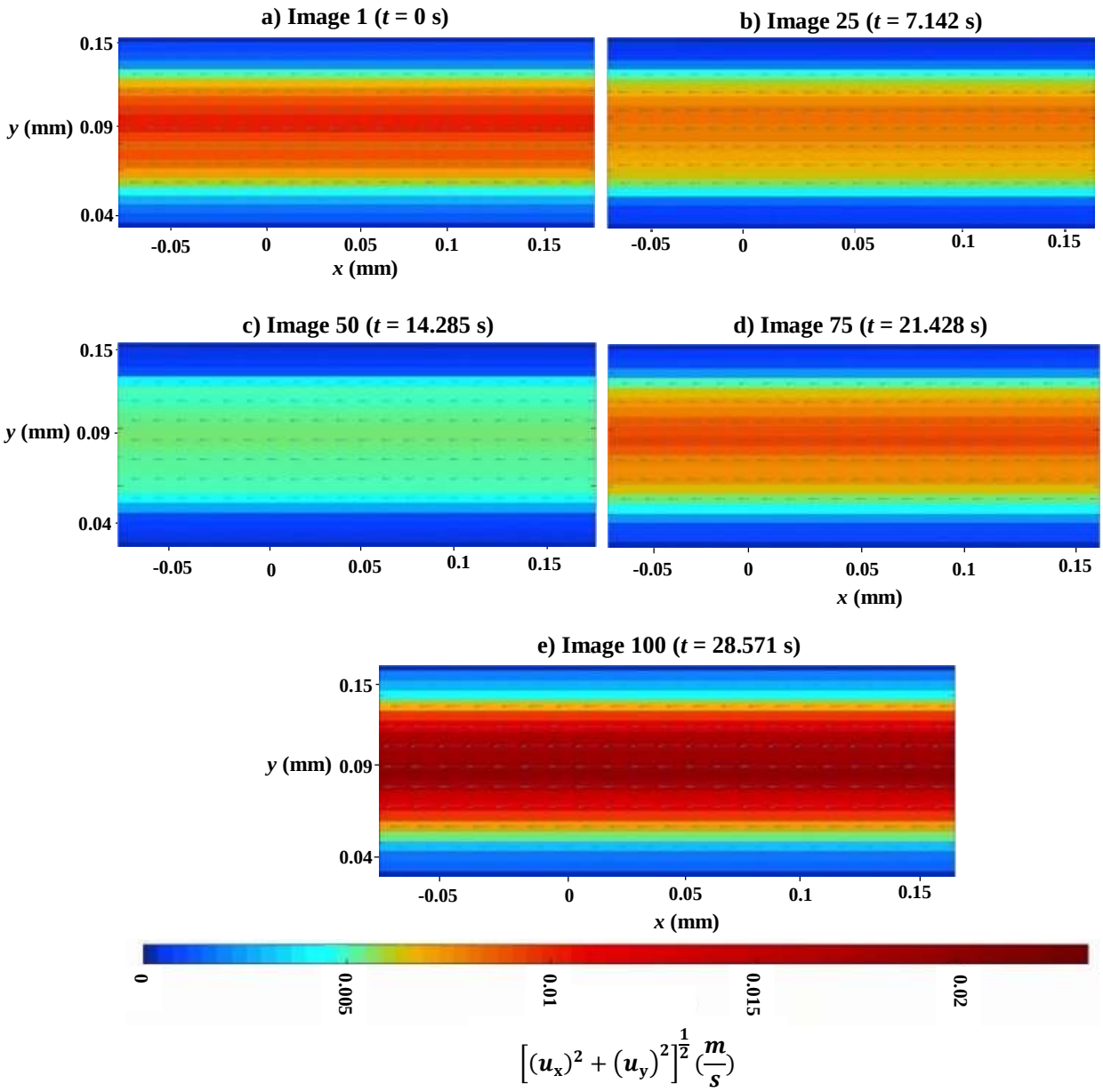

Figure B.2 Spatially averaged velocity fields at four different times of **a)** t = 0 s, **b)** t = 7.142 s, **c)** t = 14.285 s, **d)** t = 21.428 s and **e)** t = 28.571 s which approximately shows a period of fluctuation in the flow

The variation of the flow in time is more clearly visible in the spatially averaged velocity fields of Figure B.2. This cycle is repeated in a periodic fashion. In the next section of this code, the instantaneous velocity fields are normalized based on the center-plane velocity of each velocity profile in the velocity fields. Some frames of this video are shown in Figure B.3.

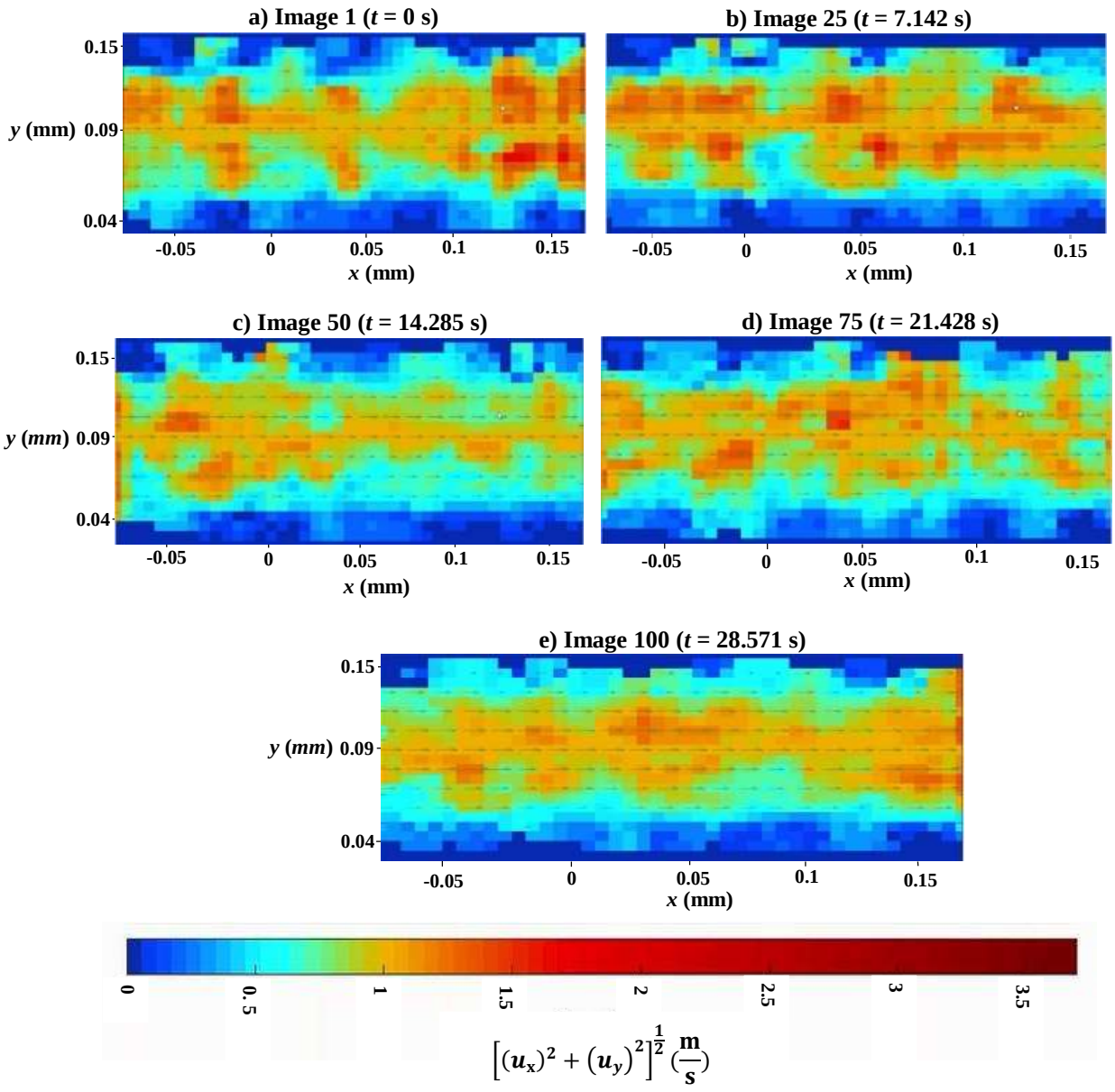

Figure B.3 Normalized instantaneous velocity fields at four different times of **a)** t = 0 s, **b)** t = 7.142 s, **c)** t = 14.285 s, **d)** t = 21.428 s and **e)** t = 28.571 s

In Figure B.3, the velocity fields are normalized based on the center plane velocity, However variations both along the channel and in time are still visible in the flow. In the next section of the code, these normalized instantaneous velocity profiles are spatially averaged. Selected normalized spatially averaged velocity profiles are shown in Figure B.4.

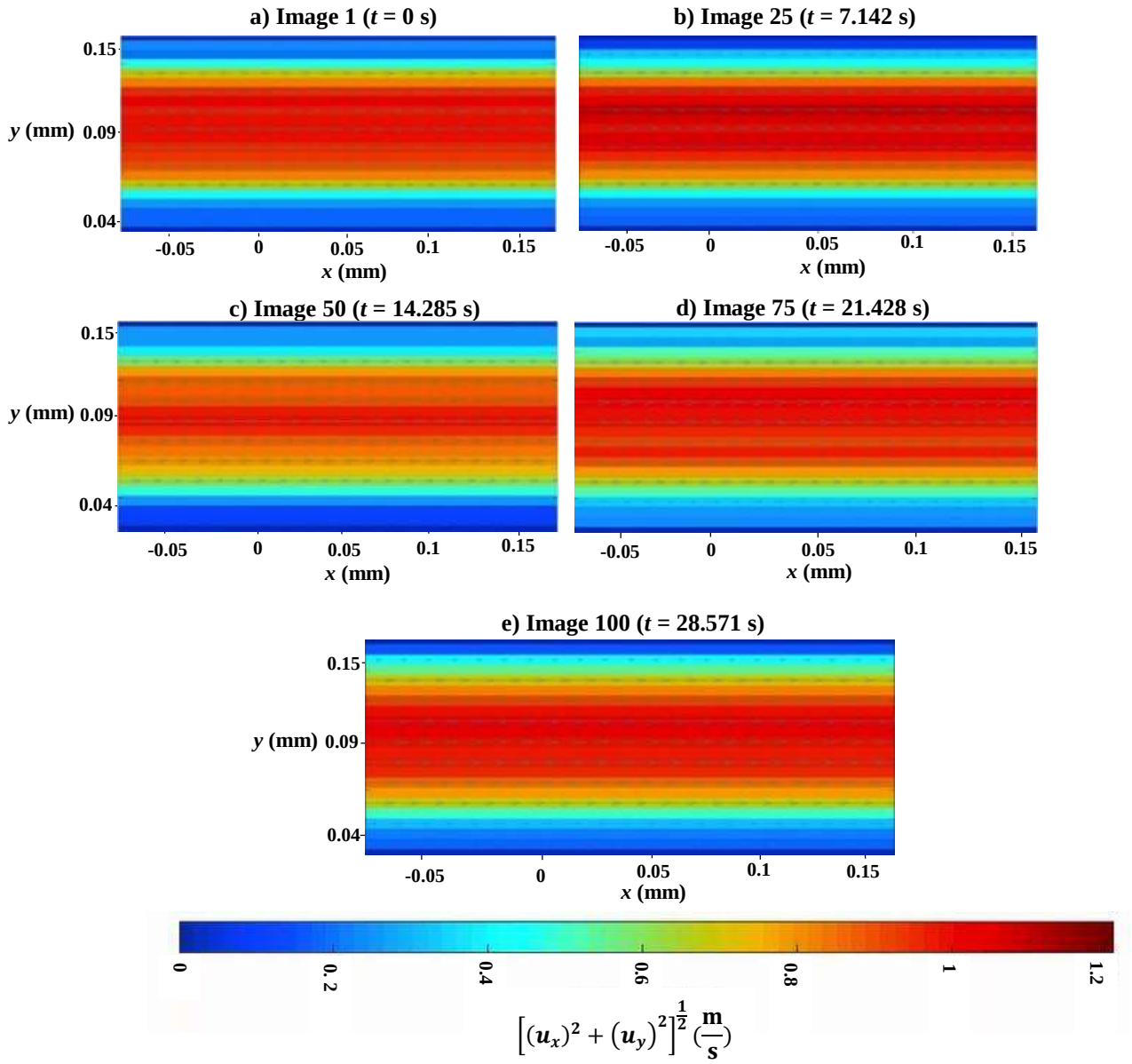

Figure B.4 Spatial averaged normalized velocity fields at four different times of **a)** t = 0 s, **b)** t = 7.142 s, **c)** t = 14.285 s, **d)** t = 21.428 s and **e)** t = 28.571 s

Figure B. 4 shows that the variations of velocity with time are decreased by the normalization process. Since the velocity variations were periodic in this experiment, time averaging minimized the effect of fluctuations in the flow therefore, non-normalized velocity profiles were presented in the result section.

In the next section of the code, all 1000 non-normalized spatially averaged velocity profiles are averaged and stored in the *avsa* parameter. Once it is calculated, it is copied to a spreadsheet for plotting versus the volume averaged analytical solution obtained from the code in Appendix B (Figure 4.8). Finally, the code averages all normalized spatially averaged velocity profiles and saves it in the *navsa* parameter. It is worth mentioning that the order of spatial averaging and normalizing was changed and no noticeable difference was observed in the final averaged velocity profiles.

APPENDIX C: CORRELATION GRAPHS

In this Appendix, sample correlation graphs corresponded to interrogation regions at different channel locations are shown for 32×32 pixel interrogation regions for both the 10x and the 20x magnification images.

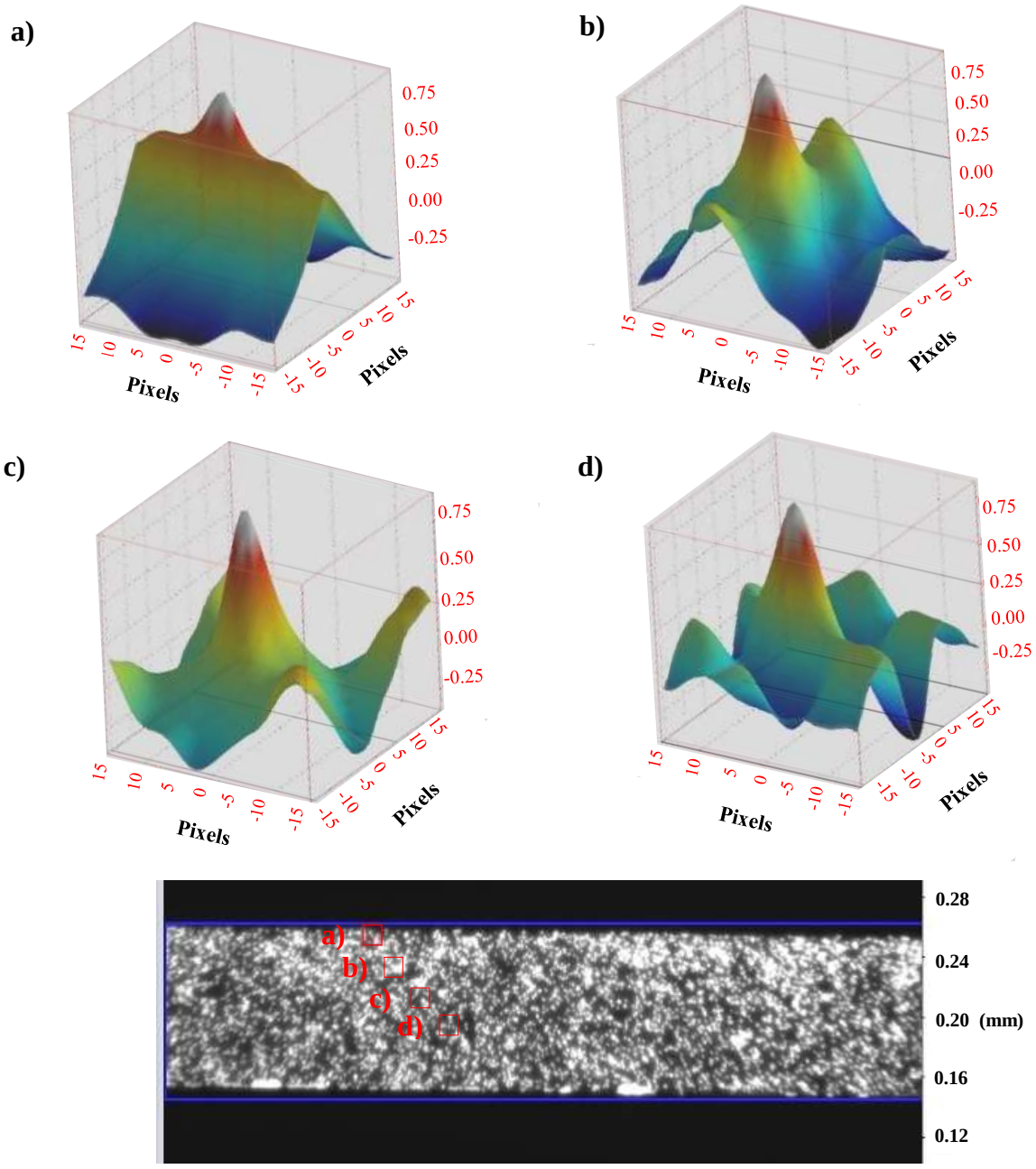

Figure C.1 Correlation graphs shown for four different interrogation regions in the channel for the 10x magnification. For all interrogation regions, correlation peaks of over 0.50 were detected. This is the threshold for a valid correlation.

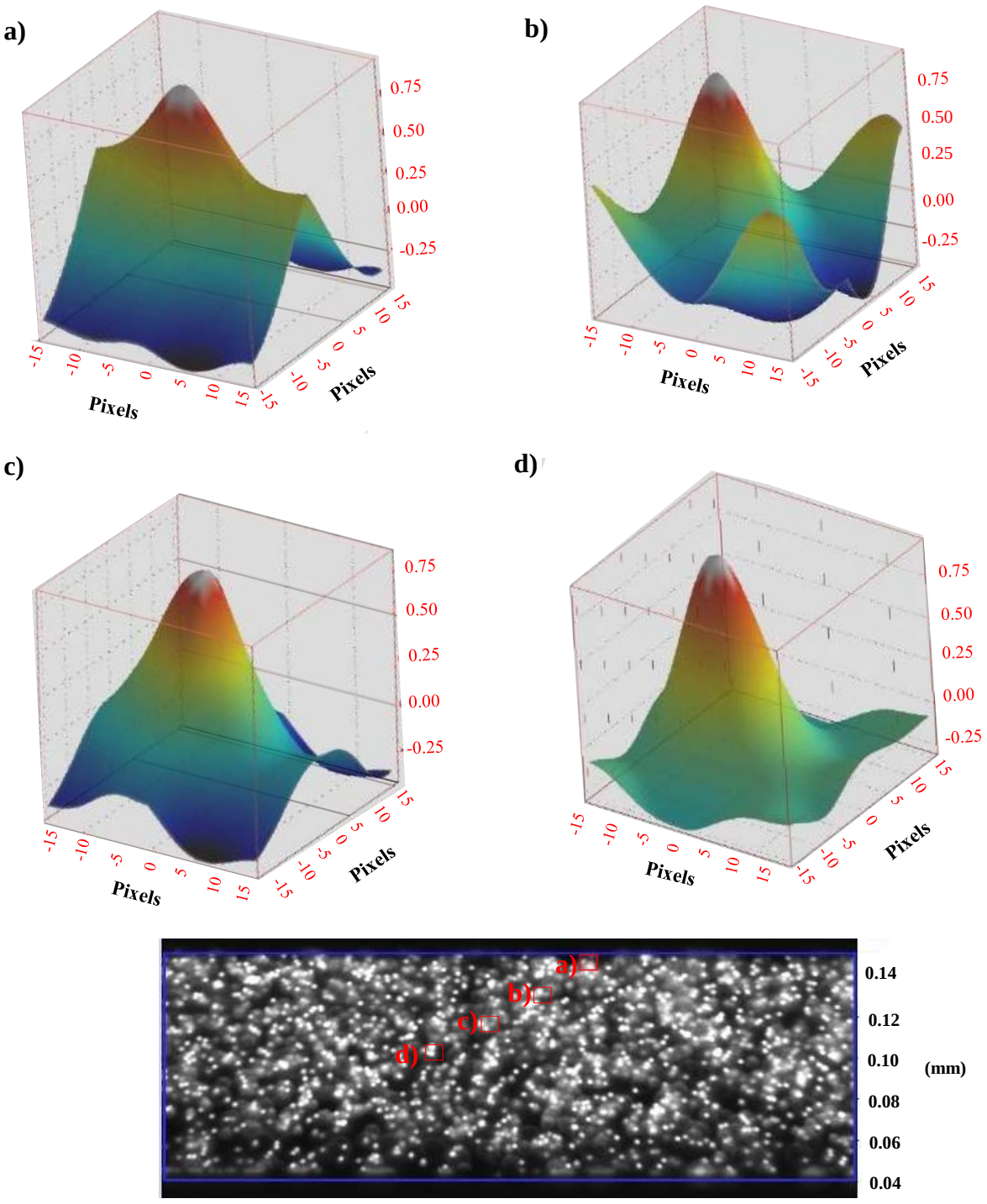

Figure C.2 Correlation graphs shown for four different interrogation regions in the channel for the 20x magnification. For all interrogation regions, correlation peaks of over 0.50 is detected. This is the threshold for a valid correlation.

APPENDIX D: PEAK-LOCKING

This Appendix, ckecks whether peak-locking had any effect on the instantaneous velocity measurements. Peak-locking occurs when particle images are smaller than the pixel size. This causes the calculated displacements to be biased toward discrete pixel values.

In order to check this issue, a histogram of the fractional part of the displacement components (in terms of pixels) is plotted, as suggested by Al-Muhammad *et al*. (2018). In this experiment, the particle diameter (3 μm) is larger than the pixels for both the 10x magnification (0.318 μm) and the 20x magnification (0.214 μm). Therefore, no peak-locking is expected in this experiment.

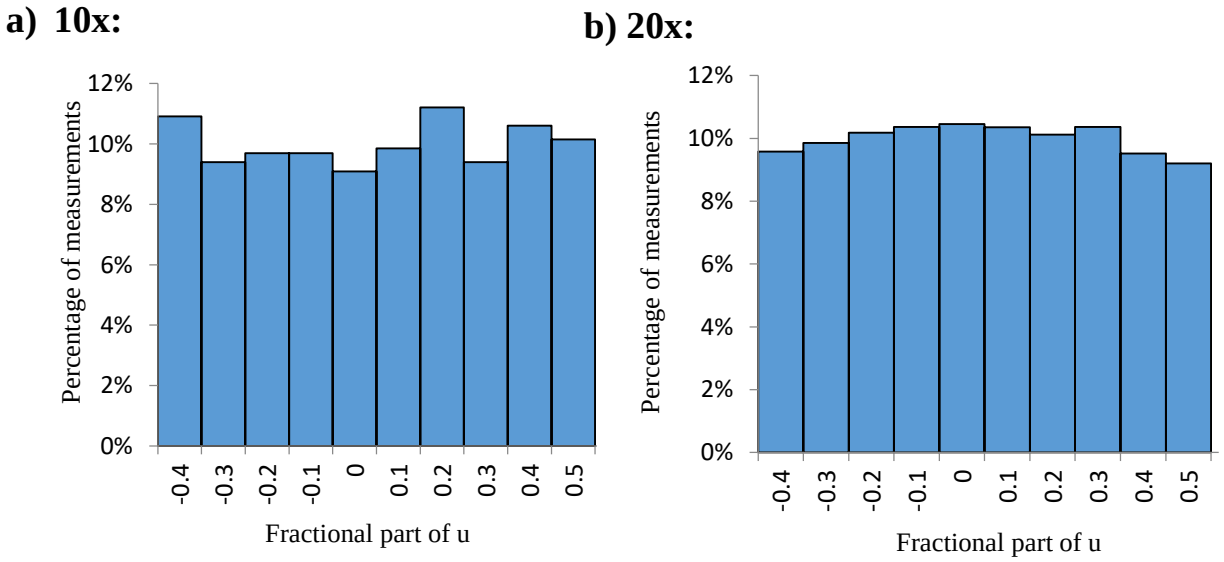

Figure D.1 Histogram of fractional part of displacements for both **a)** 10x magnification and **b)** 20x magnification.

As can be observed in Figure D.1, no obvious peak occurs in these histograms. The intensity of the peak-locking can be tested by calculating the parameter *K* given as:

$$K = 1 - \frac{Min\ (\text{Percentage of Measurements})}{Max\ (\text{Percentage of Measurements})} \tag{D.1}$$

The value of *K* is calculated based on equation D.1 as 0.31 for the 10x magnification and 0.12 for the 20x magnification. The level of peak-locking can be defined based on the value of *K* as:

- $K < 0.2$, no peak-locking occurs,
- $0.2 < K < 0.4$ mild peak-locking occurs,
- $0.4 < K < 0.6$ strong peak-locking occurs,
- $K > 0.6$ severe peak-locking occurs.

Based on the calculated value of K for this experiment, mild peak-locking is detected for the 10x magnification and there is no peak-locking in the 20x magnification data. This is due to the fact that the size of the pixels are larger in the 10x magnification images compared to the 20x magnification images.

Appendix E: PERMISSION OF USE FOR FIGURES

In this Appendix, the permission for figures taken from other sources are covered.

Figures 1.1, Figure 2.5, Figure 2.7 and Figure 3.2:

SPRINGER NATURE LICENSE
TERMS AND CONDITIONS

Sep 14, 2020

This Agreement between Mr. Amin Jahan Panah ("You") and Springer Nature ("Springer Nature") consists of your license details and the terms and conditions provided by Springer Nature and Copyright Clearance Center.

License Number	4905770340530
License date	Sep 11, 2020
Licensed Content Publisher	Springer Nature
Licensed Content Publication	Springer eBook
Licensed Content Title	Micro-PIV
Licensed Content Author	Markus Raffel, Christian E. Willert, Fulvio Scarano et al
Licensed Content Date	Jan 1, 2018
Type of Use	Thesis/Dissertation
Requestor type	academic/university or research institute
Format	electronic
Portion	figures/tables/illustrations
Number of figures/tables/illustrations	6

Will you be translating?	no
Circulation/distribution	1 - 29
Author of this Springer Nature content	no
Title	Student
Institution name	University of Saskatchewan
Expected presentation date	Oct 2020
Portions	Figure 10.6, Figure 10.7, Figure 10.9, Figure 10.11,
Requestor Location	Mr. Amin Jahan Panah 213 Ave X North Saskatoon, SK S7L 3J4 Canada Attn: Mr. Amin Jahan Panah
Billing Type	Invoice
Billing Address	Mr. Amin Jahan Panah 213 Ave X North Saskatoon, SK S7L 3J4 Canada Attn: Mr. Amin Jahan Panah
Total	0.00 CAD

Terms and Conditions

Springer Nature Customer Service Centre GmbH
Terms and Conditions

This agreement sets out the terms and conditions of the licence (the **Licence**) between you and **Springer Nature Customer Service Centre GmbH** (the **Licensor**). By clicking

'accept' and completing the transaction for the material (**Licensed Material**), you also confirm your acceptance of these terms and conditions.

1. Grant of License

1. 1. The Licensor grants you a personal, non-exclusive, non-transferable, world-wide licence to reproduce the Licensed Material for the purpose specified in your order only. Licences are granted for the specific use requested in the order and for no other use, subject to the conditions below.

1. 2. The Licensor warrants that it has, to the best of its knowledge, the rights to license reuse of the Licensed Material. However, you should ensure that the material you are requesting is original to the Licensor and does not carry the copyright of another entity (as credited in the published version).

1. 3. If the credit line on any part of the material you have requested indicates that it was reprinted or adapted with permission from another source, then you should also seek permission from that source to reuse the material.

2. Scope of Licence

2. 1. You may only use the Licensed Content in the manner and to the extent permitted by these Ts&Cs and any applicable laws.

2. 2. A separate licence may be required for any additional use of the Licensed Material, e.g. where a licence has been purchased for print only use, separate permission must be obtained for electronic re-use. Similarly, a licence is only valid in the language selected and does not apply for editions in other languages unless additional translation rights have been granted separately in the licence. Any content owned by third parties are expressly excluded from the licence.

2. 3. Similarly, rights for additional components such as custom editions and derivatives require additional permission and may be subject to an additional fee. Please apply to Journalpermissions@springernature.com/bookpermissions@springernature.com for these rights.

2. 4. Where permission has been granted **free of charge** for material in print, permission may also be granted for any electronic version of that work, provided that the material is incidental to your work as a whole and that the electronic version is essentially equivalent to, or substitutes for, the print version.

2. 5. An alternative scope of licence may apply to signatories of the STM Permissions Guidelines, as amended from time to time.

3. Duration of Licence

3. 1. A licence for is valid from the date of purchase ('Licence Date') at the end of the relevant period in the below table:

Scope of Licence	Duration of Licence
Post on a website	12 months

Presentations	12 months
Books and journals	Lifetime of the edition in the language purchased

4. Acknowledgement

4. 1. The Licensor's permission must be acknowledged next to the Licenced Material in print. In electronic form, this acknowledgement must be visible at the same time as the figures/tables/illustrations or abstract, and must be hyperlinked to the journal/book's homepage. Our required acknowledgement format is in the Appendix below.

5. Restrictions on use

5. 1. Use of the Licensed Material may be permitted for incidental promotional use and minor editing privileges e.g. minor adaptations of single figures, changes of format, colour and/or style where the adaptation is credited as set out in Appendix 1 below. Any other changes including but not limited to, cropping, adapting, omitting material that affect the meaning, intention or moral rights of the author are strictly prohibited.

5. 2. You must not use any Licensed Material as part of any design or trademark.

5. 3. Licensed Material may be used in Open Access Publications (OAP) before publication by Springer Nature, but any Licensed Material must be removed from OAP sites prior to final publication.

6. Ownership of Rights

6. 1. Licensed Material remains the property of either Licensor or the relevant third party and any rights not explicitly granted herein are expressly reserved.

7. Warranty

IN NO EVENT SHALL LICENSOR BE LIABLE TO YOU OR ANY OTHER PARTY OR ANY OTHER PERSON OR FOR ANY SPECIAL, CONSEQUENTIAL, INCIDENTAL OR INDIRECT DAMAGES, HOWEVER CAUSED, ARISING OUT OF OR IN CONNECTION WITH THE DOWNLOADING, VIEWING OR USE OF THE MATERIALS REGARDLESS OF THE FORM OF ACTION, WHETHER FOR BREACH OF CONTRACT, BREACH OF WARRANTY, TORT, NEGLIGENCE, INFRINGEMENT OR OTHERWISE (INCLUDING, WITHOUT LIMITATION, DAMAGES BASED ON LOSS OF PROFITS, DATA, FILES, USE, BUSINESS OPPORTUNITY OR CLAIMS OF THIRD PARTIES), AND
WHETHER OR NOT THE PARTY HAS BEEN ADVISED OF THE POSSIBILITY OF SUCH DAMAGES. THIS LIMITATION SHALL APPLY NOTWITHSTANDING ANY FAILURE OF ESSENTIAL PURPOSE OF ANY LIMITED REMEDY PROVIDED HEREIN.

8. Limitations

8. 1. ***BOOKS ONLY:*** Where **'reuse in a dissertation/thesis'** has been selected the following terms apply: Print rights of the final author's accepted manuscript (for clarity, NOT the published version) for up to 100 copies, electronic rights for use only on a personal website or institutional repository as defined by the Sherpa guideline (www.sherpa.ac.uk/romeo/).

9. Termination and Cancellation

9. 1. Licences will expire after the period shown in Clause 3 (above).

9. 2. Licensee reserves the right to terminate the Licence in the event that payment is not received in full or if there has been a breach of this agreement by you.

Appendix 1 — Acknowledgements:

For Journal Content:
Reprinted by permission from [**the Licensor**]: [**Journal Publisher** (e.g. Nature/Springer/Palgrave)] [**JOURNAL NAME**] [**REFERENCE CITATION** (Article name, Author(s) Name), [**COPYRIGHT**] (year of publication)

For **Advance Online Publication papers:**
Reprinted by permission from [**the Licensor**]: [**Journal Publisher** (e.g. Nature/Springer/Palgrave)] [**JOURNAL NAME**] [**REFERENCE CITATION** (Article name, Author(s) Name), [**COPYRIGHT**] (year of publication), advance online publication, day month year (doi: 10.1038/sj.[JOURNAL ACRONYM].)

For Adaptations/Translations:
Adapted/Translated by permission from [**the Licensor**]: [**Journal Publisher** (e.g. Nature/Springer/Palgrave)] [**JOURNAL NAME**] [**REFERENCE CITATION** (Article name, Author(s) Name), [**COPYRIGHT**] (year of publication)

Note: For any republication from the British Journal of Cancer, the following credit line style applies:

Reprinted/adapted/translated by permission from [**the Licensor**]: on behalf of Cancer Research UK: : [**Journal Publisher** (e.g. Nature/Springer/Palgrave)] [**JOURNAL NAME**] [**REFERENCE CITATION** (Article name, Author(s) Name), [**COPYRIGHT**] (year of publication)

For **Advance Online Publication** papers:
Reprinted by permission from The [**the Licensor**]: on behalf of Cancer Research UK: [**Journal Publisher** (e.g. Nature/Springer/Palgrave)] [**JOURNAL NAME**] [**REFERENCE CITATION** (Article name, Author(s) Name), [**COPYRIGHT**] (year of publication), advance online publication, day month year (doi: 10.1038/sj.[JOURNAL ACRONYM])

For Book content:
Reprinted/adapted by permission from [**the Licensor**]: [**Book Publisher** (e.g. Palgrave Macmillan, Springer etc) [**Book Title**] by [**Book author**(s)] [**COPYRIGHT**] (year of publication)

Other Conditions.

Version 1.2

Questions? customercare@copyright.com or +1-855-239-3415 (toll free in the US) or +1-978-646-2777.

Figure 2.1:

SPRINGER NATURE LICENSE
TERMS AND CONDITIONS

Sep 14, 2020

This Agreement between Mr. Amin Jahan Panah ("You") and Springer Nature ("Springer Nature") consists of your license details and the terms and conditions provided by Springer Nature and Copyright Clearance Center.

License Number	4906081387515
License date	Sep 11, 2020
Licensed Content Publisher	Springer Nature
Licensed Content Publication	Microfluids and Nanofluids
Licensed Content Title	Microscale flow visualization
Licensed Content Author	D. Sinton
Licensed Content Date	Aug 19, 2004
Type of Use	Thesis/Dissertation
Requestor type	academic/university or research institute
Format	print and electronic
Portion	figures/tables/illustrations
Number of figures/tables/illustrations	2
Will you be translating?	no

Circulation/distribution	1 - 29
Author of this Springer Nature content	no
Title	Student
Institution name	University of Saskatchewan
Expected presentation date	Oct 2020
Portions	Figure 3.5, Figure 3.6
Requestor Location	Mr. Amin Jahan Panah 213 Ave X North Saskatoon, SK S7L 3J4 Canada Attn: Mr. Amin Jahan Panah
Total	0.00 CAD

Terms and Conditions

Springer Nature Customer Service Centre GmbH
Terms and Conditions

This agreement sets out the terms and conditions of the licence (the **Licence**) between you and **Springer Nature Customer Service Centre GmbH** (the **Licensor**). By clicking 'accept' and completing the transaction for the material (**Licensed Material**), you also confirm your acceptance of these terms and conditions.

1. Grant of License

1. 1. The Licensor grants you a personal, non-exclusive, non-transferable, world-wide licence to reproduce the Licensed Material for the purpose specified in your order only. Licences are granted for the specific use requested in the order and for no other use, subject to the conditions below.

1. 2. The Licensor warrants that it has, to the best of its knowledge, the rights to license reuse of the Licensed Material. However, you should ensure that the material you are requesting is original to the Licensor and does not carry the copyright of another entity (as credited in the published version).

1. 3. If the credit line on any part of the material you have requested indicates that it was reprinted or adapted with permission from another source, then you should also seek permission from that source to reuse the material.

2. Scope of Licence

2. 1. You may only use the Licensed Content in the manner and to the extent permitted by these Ts&Cs and any applicable laws.

2. 2. A separate licence may be required for any additional use of the Licensed Material, e.g. where a licence has been purchased for print only use, separate permission must be obtained for electronic re-use. Similarly, a licence is only valid in the language selected and does not apply for editions in other languages unless additional translation rights have been granted separately in the licence. Any content owned by third parties are expressly excluded from the licence.

2. 3. Similarly, rights for additional components such as custom editions and derivatives require additional permission and may be subject to an additional fee. Please apply to Journalpermissions@springernature.com/bookpermissions@springernature.com for these rights.

2. 4. Where permission has been granted **free of charge** for material in print, permission may also be granted for any electronic version of that work, provided that the material is incidental to your work as a whole and that the electronic version is essentially equivalent to, or substitutes for, the print version.

2. 5. An alternative scope of licence may apply to signatories of the STM Permissions Guidelines, as amended from time to time.

3. Duration of Licence

3. 1. A licence for is valid from the date of purchase ('Licence Date') at the end of the relevant period in the below table:

Scope of Licence	Duration of Licence
Post on a website	12 months
Presentations	12 months
Books and journals	Lifetime of the edition in the language purchased

4. Acknowledgement

4. 1. The Licensor's permission must be acknowledged next to the Licenced Material in print. In electronic form, this acknowledgement must be visible at the same time as the figures/tables/illustrations or abstract, and must be hyperlinked to the journal/book's homepage. Our required acknowledgement format is in the Appendix below.

5. Restrictions on use

5. 1. Use of the Licensed Material may be permitted for incidental promotional use and minor editing privileges e.g. minor adaptations of single figures, changes of format, colour and/or style where the adaptation is credited as set out in Appendix 1 below. Any other changes including but not limited to, cropping, adapting, omitting material that affect the meaning, intention or moral rights of the author are strictly prohibited.

5. 2. You must not use any Licensed Material as part of any design or trademark.

5. 3. Licensed Material may be used in Open Access Publications (OAP) before publication by Springer Nature, but any Licensed Material must be removed from OAP sites prior to final publication.

6. Ownership of Rights

6. 1. Licensed Material remains the property of either Licensor or the relevant third party and any rights not explicitly granted herein are expressly reserved.

7. Warranty

IN NO EVENT SHALL LICENSOR BE LIABLE TO YOU OR ANY OTHER PARTY OR ANY OTHER PERSON OR FOR ANY SPECIAL, CONSEQUENTIAL, INCIDENTAL OR INDIRECT DAMAGES, HOWEVER CAUSED, ARISING OUT OF OR IN CONNECTION WITH THE DOWNLOADING, VIEWING OR USE OF THE MATERIALS REGARDLESS OF THE FORM OF ACTION, WHETHER FOR BREACH OF CONTRACT, BREACH OF WARRANTY, TORT, NEGLIGENCE, INFRINGEMENT OR OTHERWISE (INCLUDING, WITHOUT LIMITATION, DAMAGES BASED ON LOSS OF PROFITS, DATA, FILES, USE, BUSINESS OPPORTUNITY OR CLAIMS OF THIRD PARTIES), AND
WHETHER OR NOT THE PARTY HAS BEEN ADVISED OF THE POSSIBILITY OF SUCH DAMAGES. THIS LIMITATION SHALL APPLY NOTWITHSTANDING ANY FAILURE OF ESSENTIAL PURPOSE OF ANY LIMITED REMEDY PROVIDED HEREIN.

8. Limitations

8. 1. ***BOOKS ONLY:*** Where **'reuse in a dissertation/thesis'** has been selected the following terms apply: Print rights of the final author's accepted manuscript (for clarity, NOT the published version) for up to 100 copies, electronic rights for use only on a personal website or institutional repository as defined by the Sherpa guideline (www.sherpa.ac.uk/romeo/).

9. Termination and Cancellation

9. 1. Licences will expire after the period shown in Clause 3 (above).

9. 2. Licensee reserves the right to terminate the Licence in the event that payment is not received in full or if there has been a breach of this agreement by you.

Appendix 1 — Acknowledgements:

For Journal Content:
Reprinted by permission from [**the Licensor**]: [**Journal Publisher** (e.g. Nature/Springer/Palgrave)] [**JOURNAL NAME**] [**REFERENCE CITATION** (Article name, Author(s) Name), [**COPYRIGHT**] (year of publication)

For **Advance Online Publication papers:**
Reprinted by permission from [**the Licensor**]: [**Journal Publisher** (e.g. Nature/Springer/Palgrave)] [**JOURNAL NAME**] [**REFERENCE CITATION** (Article name, Author(s) Name), [**COPYRIGHT**] (year of publication), advance online publication, day month year (doi: 10.1038/sj.[JOURNAL ACRONYM].)

For Adaptations/Translations:
Adapted/Translated by permission from [**the Licensor**]: [**Journal Publisher** (e.g. Nature/Springer/Palgrave)] [**JOURNAL NAME**] [**REFERENCE CITATION** (Article name, Author(s) Name), [**COPYRIGHT**] (year of publication)

Note: For any republication from the British Journal of Cancer, the following credit line style applies:

Reprinted/adapted/translated by permission from [**the Licensor**]: on behalf of Cancer Research UK: : [**Journal Publisher** (e.g. Nature/Springer/Palgrave)] [**JOURNAL NAME**] [**REFERENCE CITATION** (Article name, Author(s) Name), [**COPYRIGHT**] (year of publication)

For **Advance Online Publication** papers:
Reprinted by permission from The [**the Licensor**]: on behalf of Cancer Research UK: [**Journal Publisher** (e.g. Nature/Springer/Palgrave)] [**JOURNAL NAME**] [**REFERENCE CITATION** (Article name, Author(s) Name), [**COPYRIGHT**] (year of publication), advance online publication, day month year (doi: 10.1038/sj.[JOURNAL ACRONYM])

For Book content:
Reprinted/adapted by permission from [**the Licensor**]: [**Book Publisher** (e.g. Palgrave Macmillan, Springer etc) [**Book Title**] by [**Book author**(s)] [**COPYRIGHT**] (year of publication)

Other Conditions:

Version 1.2

Questions? customercare@copyright.com or +1-855-239-3415 (toll free in the US) or +1-978-646-2777.

Figure 2.2 and 3.4:

SPRINGER NATURE LICENSE
TERMS AND CONDITIONS

Sep 14, 2020

This Agreement between Mr. Amin Jahan Panah ("You") and Springer Nature ("Springer Nature") consists of your license details and the terms and conditions provided by Springer Nature and Copyright Clearance Center.

License Number	4907950647272
License date	Sep 14, 2020
Licensed Content Publisher	Springer Nature
Licensed Content Publication	Springer eBook
Licensed Content Title	Fluid-Flow Characterization in Microfluidics
Licensed Content Author	Laura Campo-Deaño
Licensed Content Date	Jan 1, 2018
Type of Use	Thesis/Dissertation
Requestor type	academic/university or research institute
Format	print and electronic
Portion	figures/tables/illustrations
Number of figures/tables/illustrations	2
Will you be translating?	no

Circulation/distribution	1 - 29
Author of this Springer Nature content	no
Title	Student
Institution name	University of Saskatchewan
Expected presentation date	Oct 2020
Portions	Figure 3.5 and Figure 3.6
Requestor Location	Mr. Amin Jahan Panah 213 Ave X North Saskatoon, SK S7L 3J4 Canada Attn: Mr. Amin Jahan Panah
Total	0.00 CAD

Terms and Conditions

Springer Nature Customer Service Centre GmbH
Terms and Conditions

This agreement sets out the terms and conditions of the licence (the **Licence**) between you and **Springer Nature Customer Service Centre GmbH** (the **Licensor**). By clicking 'accept' and completing the transaction for the material (**Licensed Material**), you also confirm your acceptance of these terms and conditions.

1. Grant of License

1. 1. The Licensor grants you a personal, non-exclusive, non-transferable, world-wide licence to reproduce the Licensed Material for the purpose specified in your order only. Licences are granted for the specific use requested in the order and for no other use, subject to the conditions below.

1. 2. The Licensor warrants that it has, to the best of its knowledge, the rights to license reuse of the Licensed Material. However, you should ensure that the material you are requesting is original to the Licensor and does not carry the copyright of another entity (as credited in the published version).

1. 3. If the credit line on any part of the material you have requested indicates that it was reprinted or adapted with permission from another source, then you should also seek permission from that source to reuse the material.

2. Scope of Licence

2. 1. You may only use the Licensed Content in the manner and to the extent permitted by these Ts&Cs and any applicable laws.

2. 2. A separate licence may be required for any additional use of the Licensed Material, e.g. where a licence has been purchased for print only use, separate permission must be obtained for electronic re-use. Similarly, a licence is only valid in the language selected and does not apply for editions in other languages unless additional translation rights have been granted separately in the licence. Any content owned by third parties are expressly excluded from the licence.

2. 3. Similarly, rights for additional components such as custom editions and derivatives require additional permission and may be subject to an additional fee. Please apply to Journalpermissions@springernature.com/bookpermissions@springernature.com for these rights.

2. 4. Where permission has been granted **free of charge** for material in print, permission may also be granted for any electronic version of that work, provided that the material is incidental to your work as a whole and that the electronic version is essentially equivalent to, or substitutes for, the print version.

2. 5. An alternative scope of licence may apply to signatories of the STM Permissions Guidelines, as amended from time to time.

3. Duration of Licence

3. 1. A licence for is valid from the date of purchase ('Licence Date') at the end of the relevant period in the below table:

Scope of Licence	Duration of Licence
Post on a website	12 months
Presentations	12 months
Books and journals	Lifetime of the edition in the language purchased

4. Acknowledgement

4. 1. The Licensor's permission must be acknowledged next to the Licenced Material in print. In electronic form, this acknowledgement must be visible at the same time as the figures/tables/illustrations or abstract, and must be hyperlinked to the journal/book's homepage. Our required acknowledgement format is in the Appendix below.

5. Restrictions on use

5. 1. Use of the Licensed Material may be permitted for incidental promotional use and minor editing privileges e.g. minor adaptations of single figures, changes of format, colour and/or style where the adaptation is credited as set out in Appendix 1 below. Any other changes including but not limited to, cropping, adapting, omitting material that affect the meaning, intention or moral rights of the author are strictly prohibited.

5. 2. You must not use any Licensed Material as part of any design or trademark.

5. 3. Licensed Material may be used in Open Access Publications (OAP) before publication by Springer Nature, but any Licensed Material must be removed from OAP sites prior to final publication.

6. Ownership of Rights

6. 1. Licensed Material remains the property of either Licensor or the relevant third party and any rights not explicitly granted herein are expressly reserved.

7. Warranty

IN NO EVENT SHALL LICENSOR BE LIABLE TO YOU OR ANY OTHER PARTY OR ANY OTHER PERSON OR FOR ANY SPECIAL, CONSEQUENTIAL, INCIDENTAL OR INDIRECT DAMAGES, HOWEVER CAUSED, ARISING OUT OF OR IN CONNECTION WITH THE DOWNLOADING, VIEWING OR USE OF THE MATERIALS REGARDLESS OF THE FORM OF ACTION, WHETHER FOR BREACH OF CONTRACT, BREACH OF WARRANTY, TORT, NEGLIGENCE, INFRINGEMENT OR OTHERWISE (INCLUDING, WITHOUT LIMITATION, DAMAGES BASED ON LOSS OF PROFITS, DATA, FILES, USE, BUSINESS OPPORTUNITY OR CLAIMS OF THIRD PARTIES), AND
WHETHER OR NOT THE PARTY HAS BEEN ADVISED OF THE POSSIBILITY OF SUCH DAMAGES. THIS LIMITATION SHALL APPLY NOTWITHSTANDING ANY FAILURE OF ESSENTIAL PURPOSE OF ANY LIMITED REMEDY PROVIDED HEREIN.

8. Limitations

8. 1. ***BOOKS ONLY***:Where **'reuse in a dissertation/thesis'** has been selected the following terms apply: Print rights of the final author's accepted manuscript (for clarity, NOT the published version) for up to 100 copies, electronic rights for use only on a personal website or institutional repository as defined by the Sherpa guideline (www.sherpa.ac.uk/romeo/).

9. Termination and Cancellation

9. 1. Licences will expire after the period shown in Clause 3 (above).

9. 2. Licensee reserves the right to terminate the Licence in the event that payment is not received in full or if there has been a breach of this agreement by you.

Appendix 1 — Acknowledgements:

For Journal Content:
Reprinted by permission from [**the Licensor**]: [**Journal Publisher** (e.g. Nature/Springer/Palgrave)] [**JOURNAL NAME**] [**REFERENCE CITATION** (Article name, Author(s) Name), [**COPYRIGHT**] (year of publication)

For **Advance Online Publication papers**:
Reprinted by permission from [**the Licensor**]: [**Journal Publisher** (e.g. Nature/Springer/Palgrave)] [**JOURNAL NAME**] [**REFERENCE CITATION** (Article name, Author(s) Name), [**COPYRIGHT**] (year of publication), advance online publication, day month year (doi: 10.1038/sj.[JOURNAL ACRONYM].)

For Adaptations/Translations:
Adapted/Translated by permission from [**the Licensor**]: [**Journal Publisher** (e.g. Nature/Springer/Palgrave)] [**JOURNAL NAME**] [**REFERENCE CITATION** (Article name, Author(s) Name), [**COPYRIGHT**] (year of publication)

Note: For any republication from the British Journal of Cancer, the following credit line style applies:

Reprinted/adapted/translated by permission from [**the Licensor**]: on behalf of Cancer Research UK: : [**Journal Publisher** (e.g. Nature/Springer/Palgrave)] [**JOURNAL NAME**] [**REFERENCE CITATION** (Article name, Author(s) Name), [**COPYRIGHT**] (year of publication)

For **Advance Online Publication** papers:
Reprinted by permission from The [**the Licensor**]: on behalf of Cancer Research UK: [**Journal Publisher** (e.g. Nature/Springer/Palgrave)] [**JOURNAL NAME**] [**REFERENCE CITATION** (Article name, Author(s) Name), [**COPYRIGHT**] (year of publication), advance online publication, day month year (doi: 10.1038/sj.[JOURNAL ACRONYM])

For Book content:
Reprinted/adapted by permission from [**the Licensor**]: [**Book Publisher** (e.g. Palgrave Macmillan, Springer etc) [**Book Title**] by [**Book author**(s)] [**COPYRIGHT**] (year of publication)

Other Conditions:

Version 1.2

Questions? customercare@copyright.com or +1-855-239-3415 (toll free in the US) or +1-978-646-2777.

Figure 2.3:

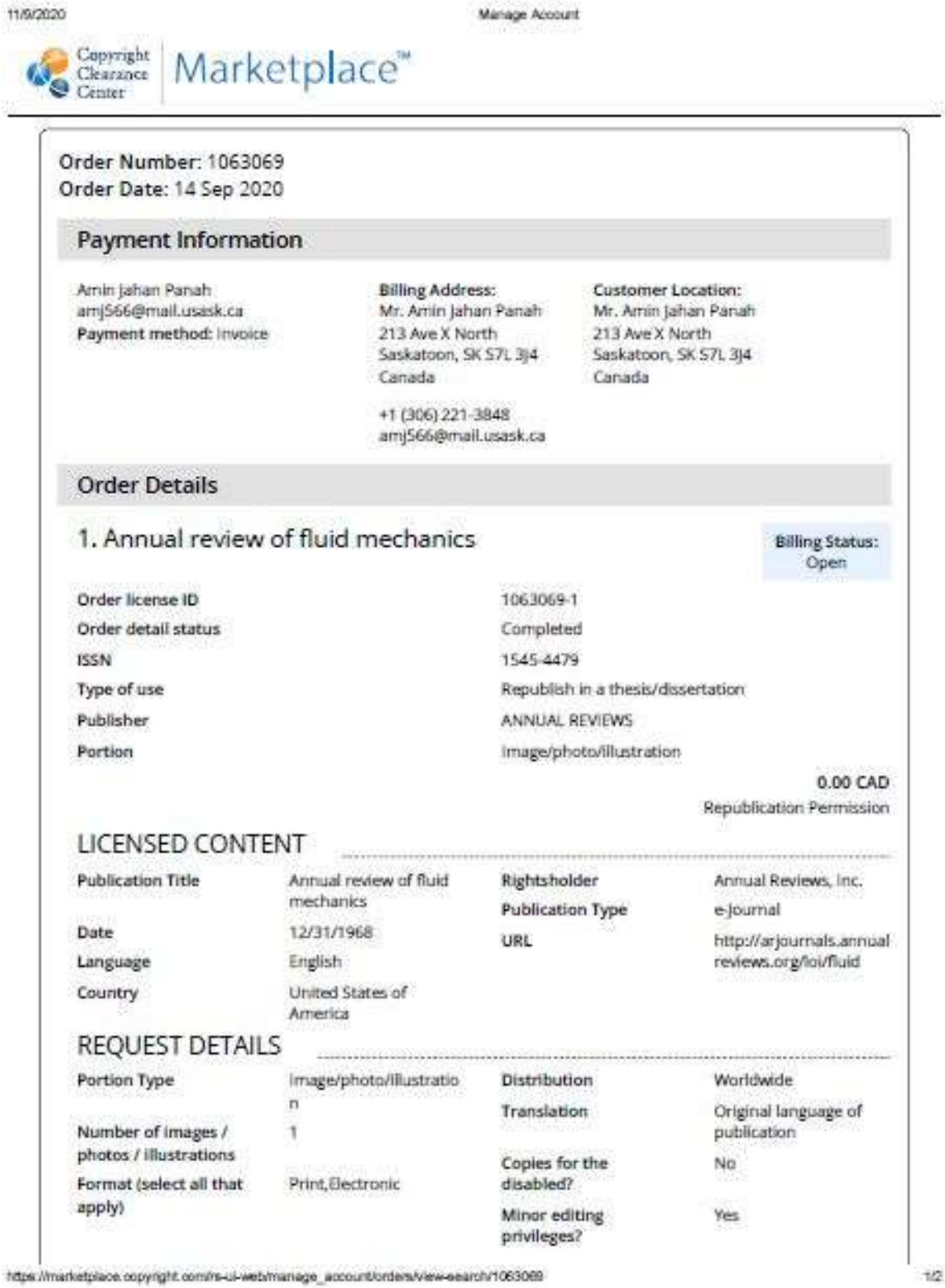

11/9/2020 Manage Account

Copyright Clearance Center | Marketplace™

Order Number: 1063069
Order Date: 14 Sep 2020

Payment Information

Amin Jahan Panah
amj566@mail.usask.ca
Payment method: Invoice

Billing Address:
Mr. Amin Jahan Panah
213 Ave X North
Saskatoon, SK S7L 3J4
Canada

+1 (306) 221-3848
amj566@mail.usask.ca

Customer Location:
Mr. Amin Jahan Panah
213 Ave X North
Saskatoon, SK S7L 3J4
Canada

Order Details

1. Annual review of fluid mechanics

Billing Status: Open

Order license ID	1063069-1
Order detail status	Completed
ISSN	1545-4479
Type of use	Republish in a thesis/dissertation
Publisher	ANNUAL REVIEWS
Portion	image/photo/illustration

0.00 CAD
Republication Permission

LICENSED CONTENT

Publication Title	Annual review of fluid mechanics	Rightsholder	Annual Reviews, Inc.
		Publication Type	e-Journal
Date	12/31/1968	URL	http://arjournals.annualreviews.org/loi/fluid
Language	English		
Country	United States of America		

REQUEST DETAILS

Portion Type	image/photo/illustration	Distribution	Worldwide
		Translation	Original language of publication
Number of images / photos / illustrations	1		
		Copies for the disabled?	No
Format (select all that apply)	Print,Electronic		
		Minor editing privileges?	Yes

https://marketplace.copyright.com/rs-ui-web/manage_account/orders/view-search/1063069 1/2

Who will republish the content?	Academic institution	Incidental promotional use?	No
Duration of Use	Life of current and all future editions	Currency	CAD
Lifetime Unit Quantity	Up to 499		
Rights Requested	Main product		

NEW WORK DETAILS

Title	EXPERIMENTAL STUDY OF A MICROFLUIDIC FLOW USING A MICRO-PIV SYSTEM	Institution name	University of Saskatchewan
		Expected presentation date	2020-10-15
Instructor name	Prof. Bergstrom and Prof. Bugg		

ADDITIONAL DETAILS

The requesting person / organization to appear on the license	Amin Jahan Panah

REUSE CONTENT DETAILS

Title, description or numeric reference of the portion(s)	Recent Advances in Micro-Particle Image Velocimetry	Title of the article/chapter the portion is from	Recent Advances in Micro-Particle Image Velocimetry
Editor of portion(s)	N/A	Author of portion(s)	Steven T. Wereley and Carl D. Meinhart
Volume of serial or monograph	N/A	Publication date of portion	2009-09-21
Page or page range of portion	557-574		

Total Items: 1

Subtotal: 0.00 CAD

Order Total: 0.00 CAD

Figure 2.6 and 2.8:

SPRINGER NATURE LICENSE
TERMS AND CONDITIONS

Sep 14, 2020

This Agreement between Mr. Amin Jahan Panah ("You") and Springer Nature ("Springer Nature") consists of your license details and the terms and conditions provided by Springer Nature and Copyright Clearance Center.

License Number	4906761099265
License date	Sep 12, 2020
Licensed Content Publisher	Springer Nature
Licensed Content Publication	Journal of Visualization
Licensed Content Title	Particle imaging techniques for volumetric three-component (3D3C) velocity measurements in microfluidics
Licensed Content Author	C. Cierpka et al
Licensed Content Date	Oct 8, 2011
Type of Use	Thesis/Dissertation
Requestor type	academic/university or research institute
Format	print and electronic
Portion	figures/tables/illustrations
Number of figures/tables/illustrations	2

Will you be translating?	no
Circulation/distribution	1 - 29
Author of this Springer Nature content	no
Title	Student
Institution name	University of Saskatchewan
Expected presentation date	Oct 2020
Portions	Figure 7, Figure 2
Requestor Location	Mr. Amin Jahan Panah 213 Ave X North Saskatoon, SK S7L 3J4 Canada Attn: Mr. Amin Jahan Panah
Total	0.00 CAD

Terms and Conditions

Springer Nature Customer Service Centre GmbH
Terms and Conditions

This agreement sets out the terms and conditions of the licence (the **Licence**) between you and **Springer Nature Customer Service Centre GmbH** (the **Licensor**). By clicking 'accept' and completing the transaction for the material (**Licensed Material**), you also confirm your acceptance of these terms and conditions.

1. Grant of License

1. 1. The Licensor grants you a personal, non-exclusive, non-transferable, world-wide licence to reproduce the Licensed Material for the purpose specified in your order only. Licences are granted for the specific use requested in the order and for no other use, subject to the conditions below.

1. 2. The Licensor warrants that it has, to the best of its knowledge, the rights to license reuse of the Licensed Material. However, you should ensure that the material you are requesting is original to the Licensor and does not carry the copyright of another entity (as credited in the published version).

1. 3. If the credit line on any part of the material you have requested indicates that it was reprinted or adapted with permission from another source, then you should also seek permission from that source to reuse the material.

2. Scope of Licence

2. 1. You may only use the Licensed Content in the manner and to the extent permitted by these Ts&Cs and any applicable laws.

2. 2. A separate licence may be required for any additional use of the Licensed Material, e.g. where a licence has been purchased for print only use, separate permission must be obtained for electronic re-use. Similarly, a licence is only valid in the language selected and does not apply for editions in other languages unless additional translation rights have been granted separately in the licence. Any content owned by third parties are expressly excluded from the licence.

2. 3. Similarly, rights for additional components such as custom editions and derivatives require additional permission and may be subject to an additional fee. Please apply to Journalpermissions@springernature.com/bookpermissions@springernature.com for these rights.

2. 4. Where permission has been granted **free of charge** for material in print, permission may also be granted for any electronic version of that work, provided that the material is incidental to your work as a whole and that the electronic version is essentially equivalent to, or substitutes for, the print version.

2. 5. An alternative scope of licence may apply to signatories of the STM Permissions Guidelines, as amended from time to time.

3. Duration of Licence

3. 1. A licence for is valid from the date of purchase ('Licence Date') at the end of the relevant period in the below table:

Scope of Licence	Duration of Licence
Post on a website	12 months
Presentations	12 months
Books and journals	Lifetime of the edition in the language purchased

4. Acknowledgement

4. 1. The Licensor's permission must be acknowledged next to the Licenced Material in print. In electronic form, this acknowledgement must be visible at the same time as the figures/tables/illustrations or abstract, and must be hyperlinked to the journal/book's

homepage. Our required acknowledgement format is in the Appendix below.

5. Restrictions on use

5. 1. Use of the Licensed Material may be permitted for incidental promotional use and minor editing privileges e.g. minor adaptations of single figures, changes of format, colour and/or style where the adaptation is credited as set out in Appendix 1 below. Any other changes including but not limited to, cropping, adapting, omitting material that affect the meaning, intention or moral rights of the author are strictly prohibited.

5. 2. You must not use any Licensed Material as part of any design or trademark.

5. 3. Licensed Material may be used in Open Access Publications (OAP) before publication by Springer Nature, but any Licensed Material must be removed from OAP sites prior to final publication.

6. Ownership of Rights

6. 1. Licensed Material remains the property of either Licensor or the relevant third party and any rights not explicitly granted herein are expressly reserved.

7. Warranty

IN NO EVENT SHALL LICENSOR BE LIABLE TO YOU OR ANY OTHER PARTY OR ANY OTHER PERSON OR FOR ANY SPECIAL, CONSEQUENTIAL, INCIDENTAL OR INDIRECT DAMAGES, HOWEVER CAUSED, ARISING OUT OF OR IN CONNECTION WITH THE DOWNLOADING, VIEWING OR USE OF THE MATERIALS REGARDLESS OF THE FORM OF ACTION, WHETHER FOR BREACH OF CONTRACT, BREACH OF WARRANTY, TORT, NEGLIGENCE, INFRINGEMENT OR OTHERWISE (INCLUDING, WITHOUT LIMITATION, DAMAGES BASED ON LOSS OF PROFITS, DATA, FILES, USE, BUSINESS OPPORTUNITY OR CLAIMS OF THIRD PARTIES), AND
WHETHER OR NOT THE PARTY HAS BEEN ADVISED OF THE POSSIBILITY OF SUCH DAMAGES. THIS LIMITATION SHALL APPLY NOTWITHSTANDING ANY FAILURE OF ESSENTIAL PURPOSE OF ANY LIMITED REMEDY PROVIDED HEREIN.

8. Limitations

8. 1. ***BOOKS ONLY:*** Where **'reuse in a dissertation/thesis'** has been selected the following terms apply: Print rights of the final author's accepted manuscript (for clarity, NOT the published version) for up to 100 copies, electronic rights for use only on a personal website or institutional repository as defined by the Sherpa guideline (www.sherpa.ac.uk/romeo/).

9. Termination and Cancellation

9. 1. Licences will expire after the period shown in Clause 3 (above).

9. 2. Licensee reserves the right to terminate the Licence in the event that payment is not received in full or if there has been a breach of this agreement by you.

Appendix 1 — Acknowledgements:

For Journal Content:
Reprinted by permission from [**the Licensor**]: [**Journal Publisher** (e.g. Nature/Springer/Palgrave)] [**JOURNAL NAME**] [**REFERENCE CITATION** (Article name, Author(s) Name), [**COPYRIGHT**] (year of publication)

For **Advance Online Publication papers:**
Reprinted by permission from [**the Licensor**]: [**Journal Publisher** (e.g. Nature/Springer/Palgrave)] [**JOURNAL NAME**] [**REFERENCE CITATION** (Article name, Author(s) Name), [**COPYRIGHT**] (year of publication), advance online publication, day month year (doi: 10.1038/sj.[JOURNAL ACRONYM].)

For Adaptations/Translations:
Adapted/Translated by permission from [**the Licensor**]: [**Journal Publisher** (e.g. Nature/Springer/Palgrave)] [**JOURNAL NAME**] [**REFERENCE CITATION** (Article name, Author(s) Name), [**COPYRIGHT**] (year of publication)

Note: For any republication from the British Journal of Cancer, the following credit line style applies:

Reprinted/adapted/translated by permission from [**the Licensor**]: on behalf of Cancer Research UK: : [**Journal Publisher** (e.g. Nature/Springer/Palgrave)] [**JOURNAL NAME**] [**REFERENCE CITATION** (Article name, Author(s) Name), [**COPYRIGHT**] (year of publication)

For **Advance Online Publication** papers:
Reprinted by permission from The [**the Licensor**]: on behalf of Cancer Research UK: [**Journal Publisher** (e.g. Nature/Springer/Palgrave)] [**JOURNAL NAME**] [**REFERENCE CITATION** (Article name, Author(s) Name), [**COPYRIGHT**] (year of publication), advance online publication, day month year (doi: 10.1038/sj.[JOURNAL ACRONYM])

For Book content:
Reprinted/adapted by permission from [**the Licensor**]: [**Book Publisher** (e.g. Palgrave Macmillan, Springer etc) [**Book Title**] by [**Book author**(s)] [**COPYRIGHT**] (year of publication)

Other Conditions:

Version 1.2

Figure 3.3:

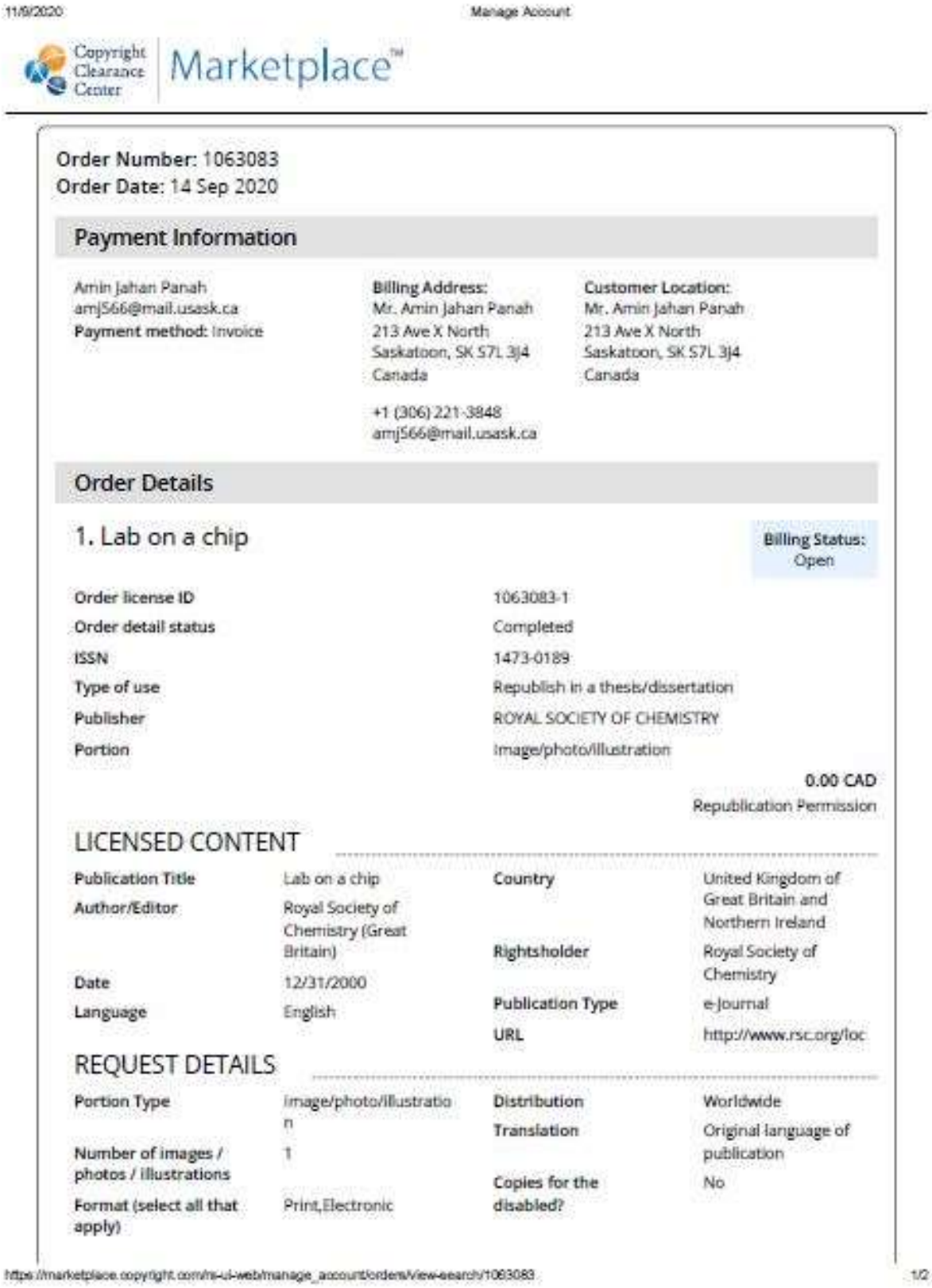

11/9/2020 Manage Account

Copyright Clearance Center | Marketplace™

Order Number: 1063083
Order Date: 14 Sep 2020

Payment Information

Amin Jahan Panah
amjS66@mail.usask.ca
Payment method: Invoice

Billing Address:
Mr. Amin Jahan Panah
213 Ave X North
Saskatoon, SK S7L 3J4
Canada

+1 (306) 221-3848
amjS66@mail.usask.ca

Customer Location:
Mr. Amin Jahan Panah
213 Ave X North
Saskatoon, SK S7L 3J4
Canada

Order Details

1. Lab on a chip

Billing Status: Open

Order license ID	1063083-1
Order detail status	Completed
ISSN	1473-0189
Type of use	Republish in a thesis/dissertation
Publisher	ROYAL SOCIETY OF CHEMISTRY
Portion	Image/photo/illustration

0.00 CAD
Republication Permission

LICENSED CONTENT

Publication Title	Lab on a chip	Country	United Kingdom of Great Britain and Northern Ireland
Author/Editor	Royal Society of Chemistry (Great Britain)	Rightsholder	Royal Society of Chemistry
Date	12/31/2000	Publication Type	e-Journal
Language	English	URL	http://www.rsc.org/loc

REQUEST DETAILS

Portion Type	Image/photo/illustration	Distribution	Worldwide
		Translation	Original language of publication
Number of images / photos / illustrations	1		
		Copies for the disabled?	No
Format (select all that apply)	Print,Electronic		

https://marketplace.copyright.com/rs-ui-web/manage_account/orders/view-search/1063083 1/2

Who will republish the content?	Academic institution	Minor editing privileges?	Yes
Duration of Use	Life of current edition	Incidental promotional use?	Yes
Lifetime Unit Quantity	Up to 499		
Rights Requested	Main product	Currency	CAD

NEW WORK DETAILS

Title	EXPERIMENTAL STUDY OF A MICROFLUIDIC FLOW USING A MICRO-PIV SYSTEM	Institution name	University of Saskatchewan
		Expected presentation date	2020-10-30
Instructor name	Prof. Bergstrom and Prof. Bugg		

ADDITIONAL DETAILS

The requesting person / organization to appear on the license	Amin Jahan Panah

REUSE CONTENT DETAILS

Title, description or numeric reference of the portion(s)	Micro-Particle Image Velocimetry (μPIV): Recent developments, applications, and guidelines†	Title of the article/chapter the portion is from	Micro-Particle Image Velocimetry (μPIV): Recent developments, applications, and guidelines†
Editor of portion(s)	N/A	Author of portion(s)	Ralph Lindken,*a Massimiliano Rossi,a Sebastian Großea and Jerry Westerweela
Volume of serial or monograph	N/A		
Page or page range of portion	2551-2567	Publication date of portion	2000-12-31

Total Items: 1

Subtotal: 0.00 CAD

Order Total: 0.00 CAD

Figure 1.2:

Hi Amin,

Thank you for reaching out.

Please consider this explicit permission to reuse the JoVE content in your thesis. Please ensure that JoVE is cited properly throughout.

Nam

Figure 2.9: